INSTITUTO TECNOLÓGICO
Y DE ESTUDIOS SUPERIORES DE OCCIDENTE

Reconocimiento de validez oficial de estudios de nivel superior según acuerdo secretarial 15018, publicado en el Diario Oficial de la Federación el 29 de noviembre de 1976.

Departamento de Electrónica, Sistemas e Informática

DOCTORADO EN CIENCIAS DE LA INGENIERÍA

MAPEO ESPACIAL A LA ENTRADA BASADO EN BROYDEN CON EXTRACCIÓN DE PARÁMETROS BASADA EN LA DISTANCIA DE KULLBACK-LEIBLER

Tesis que para obtener el grado de

DOCTOR EN CIENCIAS DE LA INGENIERÍA

presenta: Roberto Loera Díaz

Director de tesis: Dr. José Ernesto Rayas Sánchez

Tlaquepaque, Jalisco. Diciembre de 2025

DOCTOR EN CIENCIAS DE LA INGENIERÍA (2025) ITESO, Tlaquepaque, Jal., México

TÍTULO: **Mapeo espacial a la entrada basado en Broyden con extracción de parámetros basada en la distancia de Kullback-Leibler**

AUTOR: Roberto Loera Díaz
Ingeniero en Comunicaciones y Electrónica (Universidad de Guadalajara, México)
Maestro en Ciencias en Ingeniería Eléctrica (CINVESTAV-IPN, México)

DIRECTOR DE TESIS: José Ernesto Rayas Sánchez
Profesor Numerario y Emérito del Departamento de Electrónica, Sistemas e Informática, ITESO
Ingeniero en Electrónica (ITESO, México)
Maestro en Sistemas Electrónicos (ITESM Campus Monterrey, México)
Doctor en Ingeniería Eléctrica (Universidad McMaster, Canadá)
Senior, IEEE

NÚMERO DE PÁGINAS: xxix, 128

ITESO – The Jesuit University of Guadalajara

Department of Electronics, Systems, and Informatics

DOCTORAL PROGRAM IN ENGINEERING SCIENCES

BROYDEN-BASED INPUT SPACE MAPPING WITH PARAMETER EXTRACTION BASED ON THE KULLBACK-LEIBLER DISTANCE

Thesis to obtain the degree of

DOCTOR IN ENGINEERING SCIENCES

Presents: Roberto Loera-Díaz

Thesis Director: Dr. José Ernesto Rayas-Sánchez

Tlaquepaque, Jalisco, Mexico
December 2025

PHD IN ENGINEERING SCIENCES (2025) ITESO, Tlaquepaque, Jal., Mexico

TITLE: **Broyden-Based Input Space Mapping with Parameter Extraction based on the Kullback-Leibler Distance**

AUTHOR: Roberto Loera-Díaz
Bachelor's degree in communications and electronics engineering (University of Guadalajara, Mexico)
Master of Science degree in electrical engineering (CINVESTAV, Mexico)

THESIS DIRECTOR: José Ernesto Rayas-Sánchez
Department of Electronics, Systems, and Informatics, ITESO
Bachelor's degree in electronics engineering (ITESO, México)
Master's degree in electrical engineering (ITESM, México)
Ph.D. degree in electrical engineering (McMaster University, Canada)
Senior, IEEE

NUMBER OF PAGES: xxix, 128

To God.

To my wife, María Elena.

To my son, Roberto Isaac.

To my parents, Salvador and María Guadalupe.

Resumen

Los circuitos de alta frecuencia son usados en diferentes aplicaciones modernas, incluyendo electrónica de consumo, equipo médico, circuitos automotrices, etc. A estas frecuencias son inadecuados los modelos concentrados de circuitos, siendo necesario usar modelos de elementos distribuidos basados en teoría de líneas de transmisión o modelos electromagnéticos (EM) de onda completa. Los componentes de radiofrecuencia (RF) y microondas típicos pueden ser implementados en varias tecnologías, tales como microcinta, guías de onda coplanar, etc. Las simulaciones EM de onda completa, apropiadamente configuradas, se usan normalmente para validar el desempeño de estos componentes. La optimización de estos componentes, utilizando directamente simuladores EM de onda completa, puede ser muy costosa computacionalmente y, en muchos casos, inviable. La optimización de circuitos de microondas puede ser acelerada con ayuda de algoritmos de mapeo espacial (ME), los cuales optimizan modelos de muy alta exactitud, pero computacionalmente muy costosos, llamados modelos finos, con el auxilio de modelos rápidos pero insuficientemente precisos, llamados modelos burdos. Un subproceso crítico de la mayoría de los algoritmos de ME es la extracción de parámetros (EP), que consiste en encontrar los parámetros del modelo burdo que crean una respuesta del modelo burdo tan similar como sea posible a la respuesta del modelo fino en cada iteración de ME. Para medir la similitud entre las respuestas del modelo burdo y fino, normas clásicas, como la norma Manhattan, Euclidiana y Chebyshev son muy usadas. Esta disertación doctoral primero presenta un proceso de validación de simulaciones EM de onda completa de filtros en tecnología microcinta que son usados posteriormente en ejemplos de EP y ME. Después, propone una formulación numérica de EP basada en la distancia de Kullback-Leibler (K-L), haciendo comparaciones rigurosas con funciones objetivo basadas en normas clásicas. Además, propone una formulación de ME a la entrada basado en Broyden con EP basada en la distancia de K-L, la cual es la contribución principal de esta tesis doctoral. Los resultados generales de esta disertación, ilustrados por varios ejemplos, incluyendo ejemplos sintéticos y filtros microcinta cuyos modelos EM de onda completa fueron usados como modelos finos, demuestran que ME con EP usando K-L tiene un comportamiento igual o superior al de ME con EP usando normas clásicas. Varias posibilidades de investigación futura relacionadas a estos temas también son mencionadas en esta disertación.

Summary

High-frequency and high-speed circuits are commonly used in different kinds of modern electronics applications, including consumer electronics, medical equipment, automotive circuitry, among others. For these high frequencies, regular lumped circuit models are inadequate, being necessary to use distributed-element models based on transmission line theory or even full-wave electromagnetic (EM) models. Typical radio frequency (RF) and microwave components can be implemented in a variety of general technologies, such as microstrip, stripline, coplanar waveguide, etc. Properly configured full-wave EM simulations are normally employed to validate the performance of these components. Optimizing the performance of these RF and microwave components by directly using full-wave EM simulators can be computationally very expensive and, in many cases, even unfeasible. The design optimization process of microwave circuits can be accelerated with the help of space mapping (SM) algorithms, which optimize highly accurate but computationally expensive models, also known as fine models, with the support of fast but not accurate enough models, known as coarse models. A critical sub-process of most SM algorithms is parameter extraction (PE), which consists of finding the coarse model parameters that create a coarse model response as similar as possible to the fine model response at each iteration of the SM algorithm. To measure the similarity between the coarse and fine model responses, classical norms, such as the Manhattan, Euclidean, and Chebyshev norms are widely used. This doctoral dissertation first presents a validation procedure of full-wave EM simulations of filters in microstrip technology which are subsequently used in PE and SM examples. Next, it proposes a numerical PE formulation based on the Kullback-Leibler (K-L) distance, making rigorous comparisons with objective functions based on classical norms. Furthermore, it proposes a Broyden-based input SM formulation with PE based on the K-L distance, which is the principal contribution of this PhD thesis. The overall results presented in this dissertation, illustrated by many examples, considering both synthetic examples and filters in microstrip technology whose full-wave EM simulation responses were used as fine models, demonstrate that SM with PE based on the K-L distance behaves similarly or better than SM with PE based on classical norms. Some future research opportunities related to these topics are also mentioned in this dissertation.

Acknowledgements

The author wishes to express his sincere appreciation to Dr. José Ernesto Rayas-Sánchez, professor of the Department of Electronics, Systems, and Informatics at ITESO, for his encouragement, expert guidance, and keen supervision as doctoral thesis director throughout the course of this work. The author offers his gratitude to Dr. Zabdiel Brito-Brito, now at the Polytechnic University of Catalonia, Spain, for his feedback during the initial part of the author's PhD research. He also thanks Dr. Omar Humberto Longoria-Gándara, Dr. Esteban Martínez-Guerrero, Dr. Luis Rizo-Domínguez, and Dr. Francisco Elías Rangel-Patiño, members of his Ph.D. Thesis Committee, for their interest, assessment, and suggestions.

The author has greatly benefited from working with PathWave Advance Design System (ADS) developed by Keysight, Sonnet EM developed by Sonnet Software Inc., and MATLAB developed by The MathWorks Inc. The author is grateful to Dr. James Rautio, President of Sonnet Software, for making the Sonnet Suites available for this work.

It is the author's pleasure to acknowledge fruitful collaboration and stimulating discussions with his colleagues of CAECAS research group at ITESO – The Jesuit University of Guadalajara: José Luis Chávez-Hurtado, Juan Rafael del-Rey-Acuña, Felipe de Jesús Leal-Romo, Andrés Viveros-Watcher, Jacqueline Sánchez-Mesa, Joge Dávalos-Guzmán, Aurea Edna Moreno-Mojica and Enrique Raúl Villa-Loustaunau.

The author gratefully acknowledges the financial assistance through a scholarship granted by the *Consejo Nacional de Ciencia y Tecnología* (CONACYT), Mexican Government. The author also acknowledges the support provided by ITESO, as well as the support provided by Continental AG.

Finally, the author gives special thanks to his family, his wife María Elena Rosales-Ruvalcaba and his son Roberto Isaac Loera-Rosales, for their understanding, patience, and continuous loving support. Special thanks to his parents, Salvador Loera-Vivar and María Guadalupe Díaz-Velasco, for their guidance, and thanks to his siblings, Salvador Loera-Díaz, María Guadalupe Loera-Díaz and Adriana Loera-Díaz.

Contenido

Contents

List of Figures

List of Tables

Introduction

Microstrip, stripline, and other planar technologies are commonly used in modern electronics industries, at different physical levels (PCB, package, and chip level) [Aksun-05]. The use of high-frequency components is largely demanded for high-speed operation in many electronic devices. Filters implemented by distributed elements are used when the operating frequency of the system is very high, as in many diverse microwave systems. Classical filter lumped models, which are typically used for low frequencies, are inadequate for these high frequencies [Pozar-98]. In this scenario, distributed equivalent circuits based on transmission line theory, or even full-wave electromagnetic models are employed instead of lumped elements [Maas-14].

Nowadays, microstrip filters are widely used for high frequency applications [Hong-01]. Distributed-element filters are designed by changing the physical dimensions and shapes of the physical structures or topologies as well by selecting the appropriate dielectric and metallic materials. Some of the typical physical parameters of a microstrip circuit include the substrate heights, the widths and lengths of the microstrip traces, the separating gaps between traces, as well as materials properties like the relative dielectric permittivity, dielectric loss tangent, metal conductivity, etc.

The elaboration process of a microstrip circuit can be complex and relatively expensive. Moreover, once a circuit is fabricated, it cannot be adjusted or optimized. To optimize circuits in microstrip technology [Ravindran-06], [Koziel-13], simulation software is widely used [Swanson-03]. Equivalent circuit models, both lumped and distributed, for microstrip circuits are usually computationally fast, however, in many cases they are not sufficiently accurate. Therefore, their use to design microstrip circuits is limited. On the other hand, full-wave electromagnetic (EM) models are more accurate [Kogure-11], but they are much more computationally expensive and slower than equivalent circuit models.

Full-wave EM simulation responses of filters and other RF and microwave structures, in microstrip and other technologies, might vary depending on the numerical method employed in the EM simulator and its configuration parameter settings [Chávez-Hurtado-14c] and [Brito-Brito-15]. Therefore, to obtain reliable full-wave EM simulations, the EM simulator must be properly

configured. This is important for full wave EM simulators and even more important for multiphysics simulators such us COMSOL [Brito-Brito-13], which are used for multiphysics analysis and design. Some other commercially available electromagnetic simulators are the ones from Sonnet and Keysight, among others, which also require proper configuration settings.

A target or desired response of a system can be optimally approximated by numerical parameter extraction (PE) if there is available a parameterized model that approximates the system. PE formulations can be used to minimize the error between an initial model response and the target response [Bandler-04]. Formulations with classical norms (Manhattan, Euclidean, and Chebyshev norms) are commonly used to measure the error between these two responses.

Parameter extraction is also the most critical process in several space mapping (SM) optimization algorithms [Koziel-08], [Bandler-95]. SM techniques are used for the efficient optimization of highly accurate models that require large computational effort, known as fine models, with the support from simplified models that are computationally fast but not accurate enough, known as coarse models [Bakr-00], [Cheng-08], [Rayas-Sánchez-21a]. Most SM algorithms require solving a parameter extraction sub-problem at each iteration. PE essentially consists of finding, at each iteration, the coarse model parameters that generate a coarse model response as similar as possible to the current fine model response. Using better formulations for PE can positively impact on the convergence of those SM algorithms [Bandler-04], and can make them even more efficient. The optimization of circuits in microstrip technology, such as microstrip filters, can be performed using SM algorithms, where an equivalent circuit can be used as coarse model and a full-wave EM simulator can be used as fine model.

In a very different arena, in the field of information theory, the "Kullback-Leibler [Kullback-51] (K-L) measure", also known as "K-L divergence", or "K-L distance" [Kullback-87], was developed for measuring the divergence in statistical populations. The difference between two probability distributions can be efficiently measured with this K-L formulation [Vergara-09]. Although, S. Kullback mentions in [Kullback-87] that he preferred the term "discrimination information" over other terms, he recognizes that the nomenclature "Kullback-Leibler distance" (and other names) has been employed extensively, and for that reason it is used throughout this thesis. The K-L formulation has been applied to many fields and applications, for example, in speech synthesis [Veldhuis-03], image processing [Do-02], and others [Vergara-09].

This doctoral dissertation presents a Broyden-based space mapping algorithm with

parameter extraction based on the K-L distance applied to some synthetic examples as well as to some filters in microstrip technology whose equivalent circuit models are used as coarse models and the full-wave EM models are used as fine models. This dissertation is organized as follows.

Chapter 1 presents the validation of some EM models implemented in ADS Momentum for filters in microstrip technology, including a single-stub band-stop filter, a low-pass filter, a band-pass filter, and another band-stop filter. Some of these validated filters are later used in Chapter 3 and Chapter 4.

Chapter 2 proposes an objective function formulation for circuit parameter extraction based on the K-L distance, illustrated with a sixth-order π band-pass lumped filter (one-dimensional PE example) and an ideal 10:1 two section impedance transformer (two-dimensional PE example). A comparison of PE is performed with classical norms (Manhattan, Euclidean, and Chebyshev norms) against the K-L formulation. Moreover, this chapter shows a graphical comparison of the objective functions, for the mentioned examples, between the classical norms formulations and the proposed K-L formulation.

Chapter 3 presents a PE graphical and numerical study using classical norms and the K-L formulation. Some synthetic examples are considered in this chapter: a one-section impedance transformer, a two-section impedance transformer, and a third-order low-pass asymmetrical lumped filter. Moreover, the single-stub band-stop filter in microstrip technology, validated in Chapter 1, is also used in this chapter. Additionally, this chapter shows, using the previously mentioned examples, that PE with the K-L formulation requires less evaluations of the objective function with similar or better error matching in comparison to classical norm formulations.

Chapter 4 describes the most important contribution in this doctoral dissertation. It describes a Broyden-based SM algorithm with PE based on the K-L formulation. First, PE using classical norms and the K-L formulation is applied to the low-pass and the band-pass filters validated in Chapter 1. Then, SM with PE based on classical norms and the K-L formulation is illustrated with a synthetic example (the one-section impedance transformer used in Chapter 2) and with the single-stub band-stop, low-pass and band-pass filters validated in Chapter 1. The equivalent circuit model of these microstrip filters is used as coarse model, while the full-wave EM model is used as fine model. Furthermore, this chapter shows, using the previously mentioned examples, that SM with PE based on the K-L formulation yields similar or better results, than SM with classical norms for PE, with less evaluations of the objective function for the PE sub-process.

In the General Conclusions, the most relevant remarks about this doctoral dissertation are summarized, discussing the overall results of the proposed SM algorithm with PE based on the K-L distance. Some opportunities for future research are also briefly outlined.

Finally, Appendix A shows the reference list of the eleven internal research reports developed during these doctoral studies, and Appendix B shows the list of papers published during this same period of time.

1. Validating Electromagnetic Models Implemented in ADS Momentum for Filters in Microstrip Technology

The use of high-frequency filters has become very common in industry due to the high-speed operation of many electronic devices. In this chapter, several filters implemented as distributed elements in microstrip technology are simulated and validated, including low-pass, band-pass and band-stop filters.

Full-wave electromagnetic (EM) simulation responses can vary depending on the EM simulator used and how it is configured, therefore, a proper simulator configuration is required. This chapter presents a procedure for reliable full-wave EM simulations performed in ADS Momentum for these microstrip filters. The simulation responses obtained for these microstrip filters are validated with responses previously obtained with a different electromagnetic simulator such as Sonnet. The first microstrip filter is a single-stub band-stop filter, the second filter is a low-pass filter, the third filter is a band-pass filter and the last filter is fifth order Chebyshev band-stop filter.

This chapter also presents a comparison of simulation responses of this low-pass microstrip filter with two different circuit models implemented in ADS. The full-wave EM response from ADS Momentum Microwave of the physical layouts obtained from these circuit models is included as reference for assessing the accuracy of the circuit model responses. The first circuit model uses MTEE, MLIN, and MLOC components. The second circuit model uses a MSOP component and a couple of MLIN components. Differences in the circuit responses are highlighted.

1.1. Introduction

Filters implemented by distributed elements are used when the operation frequency of the system is very high, as in microwave systems. For these high frequencies, typical filter models used for low frequencies are inadequate: distributed elements are used instead of lumped elements [Pozar-98], [Hong-01]. Distributed-element filters are designed by changing the physical

dimensions and shapes of the physical structures or topologies. Nowadays, filters in microstrip technology [Loera-Díaz-20c], [Villa-Loustaunau-23] are widely used for high frequency applications [Hennings-06].

The microstrip filters used in this chapter are implemented in Keysight PathWave Advanced Design System (ADS[1]) [Keysight-22] considering circuit models and their respective full-wave electromagnetic (EM) model implemented in ADS Momentum Microwave. To validate these responses, they are compared against the full-wave EM response obtained in a different EM simulator for the same filter [Loera-Díaz-22], [Loera-Díaz-23a]. In Chapters 3 and 4, these circuit model responses and full-wave EM model responses are used as coarse model and fine model respectively to illustrate parameter extraction using classical norms and a proposed objective function formulation based on the Kullback-Leibler distance.

Full-wave EM simulation responses of filters and other structures in microstrip and other technologies might vary depending on the EM simulator employed and their parameters configuration. Therefore, to obtain reliable full-wave EM simulations, the EM simulator must be properly configured. In this chapter, we describe a method to configure Keysight ADS Momentum to obtain reliable full-wave EM simulations of three microstrip filters [Loera-Díaz-20c]. The responses of these filters are compared against previously validated responses simulated in a different electromagnetic simulator.

As a first example, we show the configuration and validation of a single-stub band-stop microstrip filter. The second filter considered is a low-pass microstrip filter. Several configuration cases are studied to analyze which one generates the most accurate response in the shorter simulation time among these cases. The same cases are compared between two 2-D EM simulators available in ADS: ADS Momentum Microwave and ADS Momentum RF.

We present a comparison of simulation results for this low-pass filter in microstrip technology using two different circuit models created in Keysight ADS. Additionally, a comparison is made with the full-wave EM responses of the layout obtained from these circuit models. These full-wave EM responses are obtained using ADS Momentum Microwave.

The third filter is a microstrip band-pass filter. In a similar way to the previous example, some configuration cases are compared to determine which case generates the most accurate

[1] Advance Design System (ADS), Version 512.update2.0, Keysight Technologies, 1400 Fountaingrove Pkwy, Santa Rosa CA 95403-1738, 1985-2020

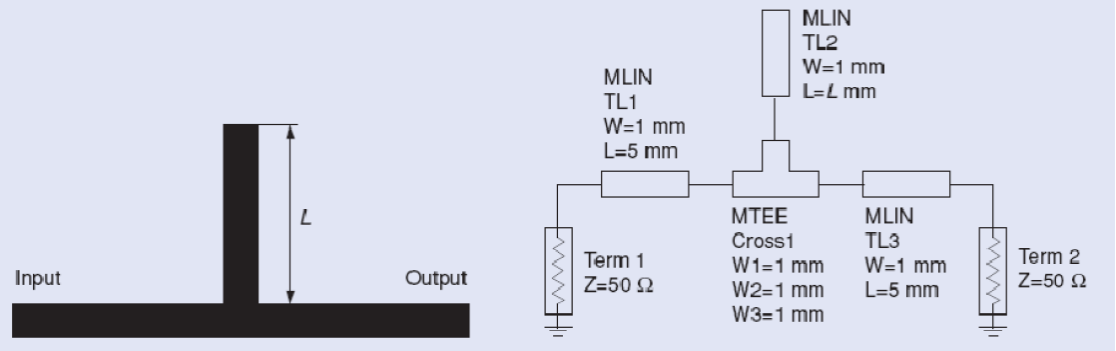

Fig. 1.1 Microstrip single-stub band-stop filter: a) geometry, b) ADS schematic. Images taken from [Koziel-08].

response among them, using also ADS Momentum Microwave and ADS Momentum RF.

Finally, we show the configuration and validation of a fifth order Chebyshev band-stop microstrip filter. Similarly, several configuration cases are considered, which are simulated using only ADS Momentum RF.

The overall results obtained in this chapter reconfirm the importance of properly configuring ADS Momentum for reliable simulations.

The EM models used in this chapter consider only nominal responses, however it is also important con consider manufacturing variation but it is very difficult to implement. An example of yield estimation considering manufacturing variation can be found in [Loera-Díaz-18].

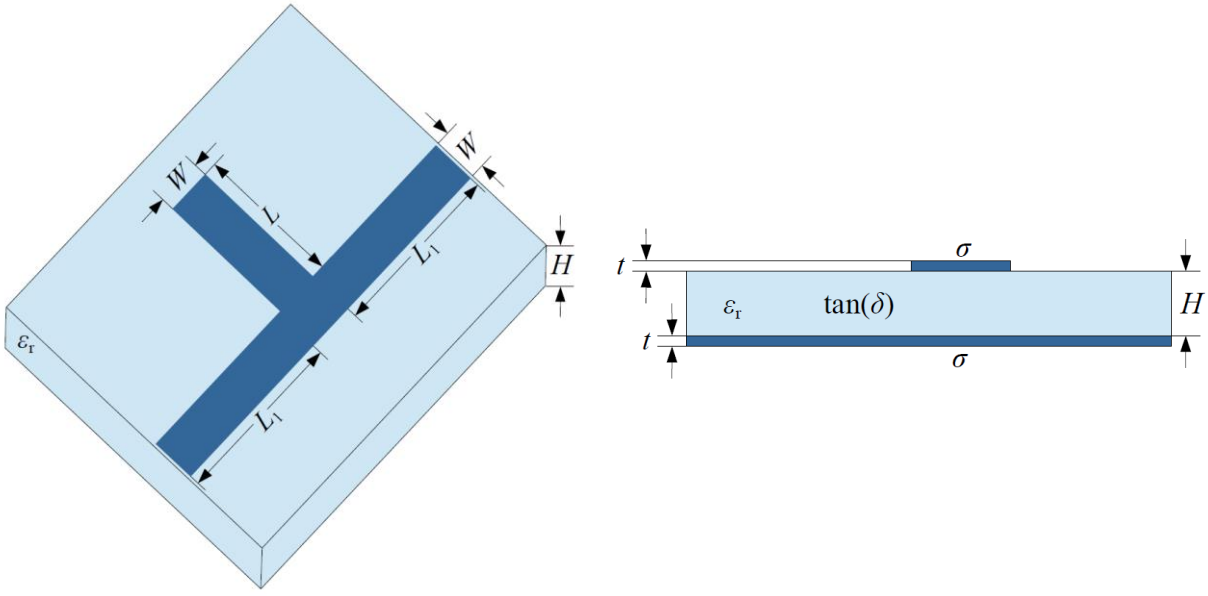

Fig. 1.2 Geometrical structure of the microstrip single-stub band-stop filter [Koziel-08], [Loera-Díaz-25c]. Figure taken from [Loera-Díaz-23b].

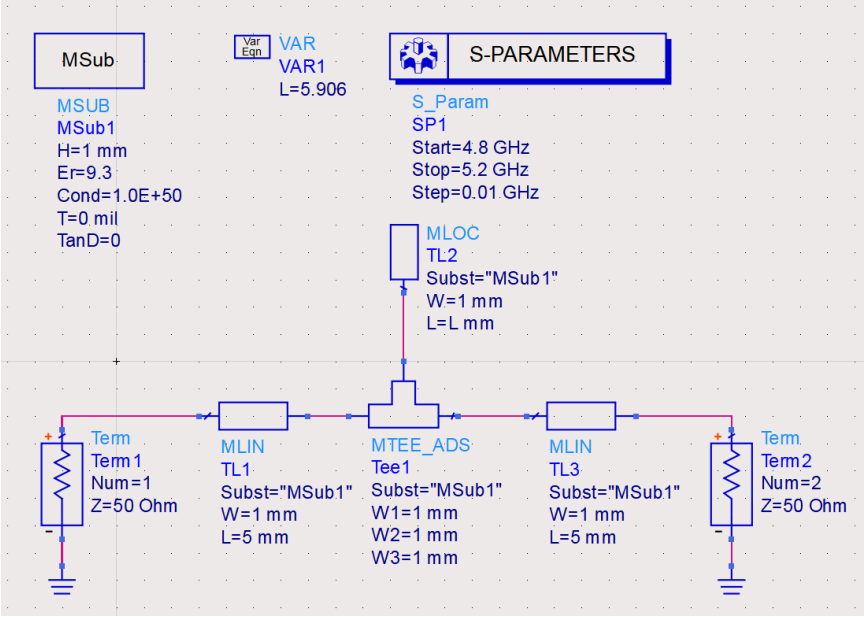

Fig. 1.3 Circuit model made in ADS for the microstrip single-stub band-stop filter (coarse model).

1.2. Microstrip Structures in ADS

Microstrip structures [Chávez-Hurtado-14a], [Chávez-Hurtado-14b], [Rayas-Sánchez-09], like those used in high-frequency filters, can be simulated in Keysight ADS, in two ways: by using distributed circuit models or by using a full-wave EM models. The simulation time for distributed

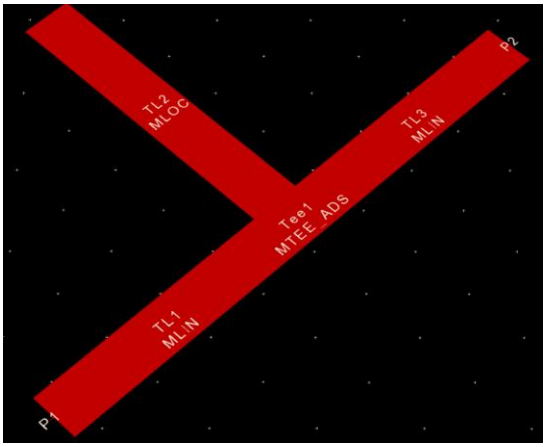

Fig. 1.4 Layout geometry in ADS Momentum for the microstrip single-stub band-stop filter (fine model).

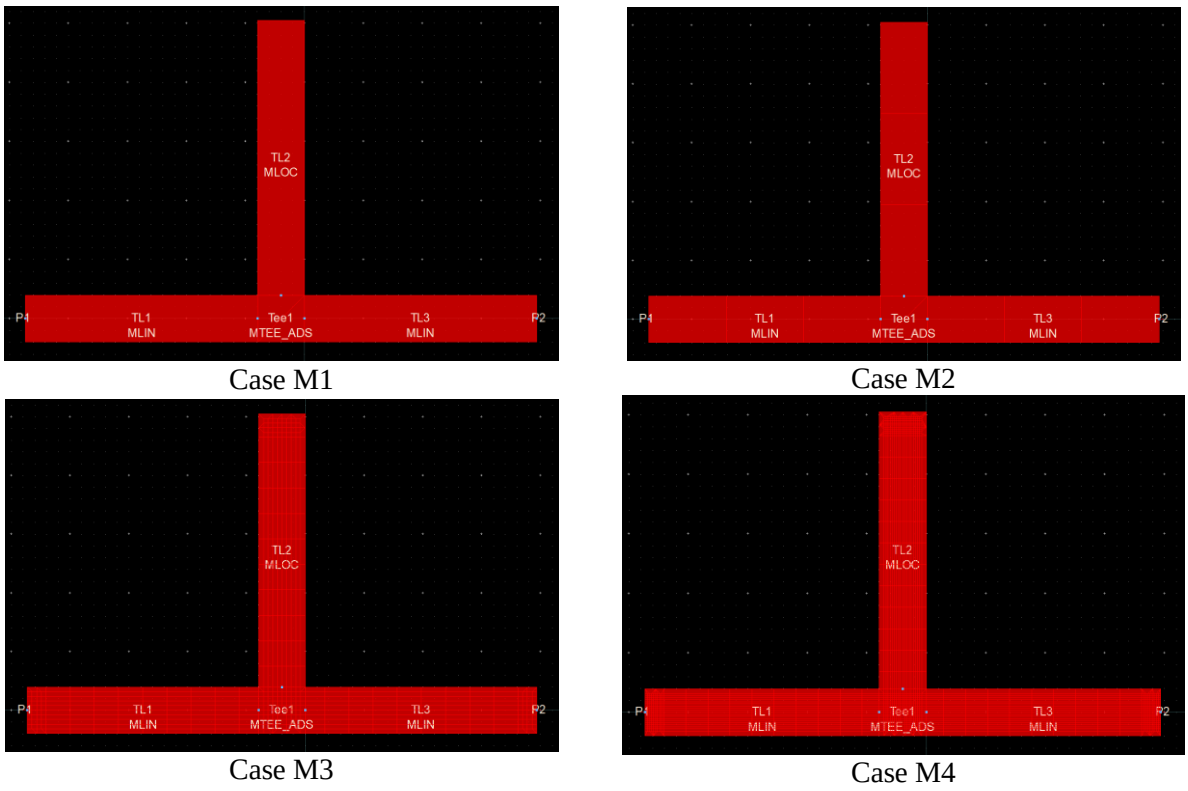

Fig. 1.5 Varying the mesh for the microstrip single-stub band-stop filter in ADS Momentum: Cases M1 to M4.

circuit models is much faster than that one for full-wave EM models, however, distributed circuit models are not as accurate as the EM models (if properly configured). A distributed circuit model is based on quasi-static electromagnetic approximations of the actual physical structure (layout geometry and material properties) by using parameterized transmission lines and parameterized lumped components combined with analytical and empirical equations. On the other hand, full-

TABLE 1.1. CONFIGURATION OF ADS MOMENTUM FOR THE SINGLE-STUB BAND-STOP MICROSTRIP FILTER

Case	Mesh density (cells/λ)	Edge mesh	Transmission line mesh	Thin layer overlap extraction	Port feed type	Simulation time (hr:min:sec)	
						Momentum Microwave	Momentum RF
M1	1	Not used	Not used	Normal	Auto	0:00:05	0:00:03
M2	5	Not used	Not used	Normal	Auto	0:00:05	0:00:04
M3	20	Auto	10	Aggressive	TML	0:01:15	0:00:19
M4	20	Auto	20	Aggressive	TML	0:10:53	0:03:05

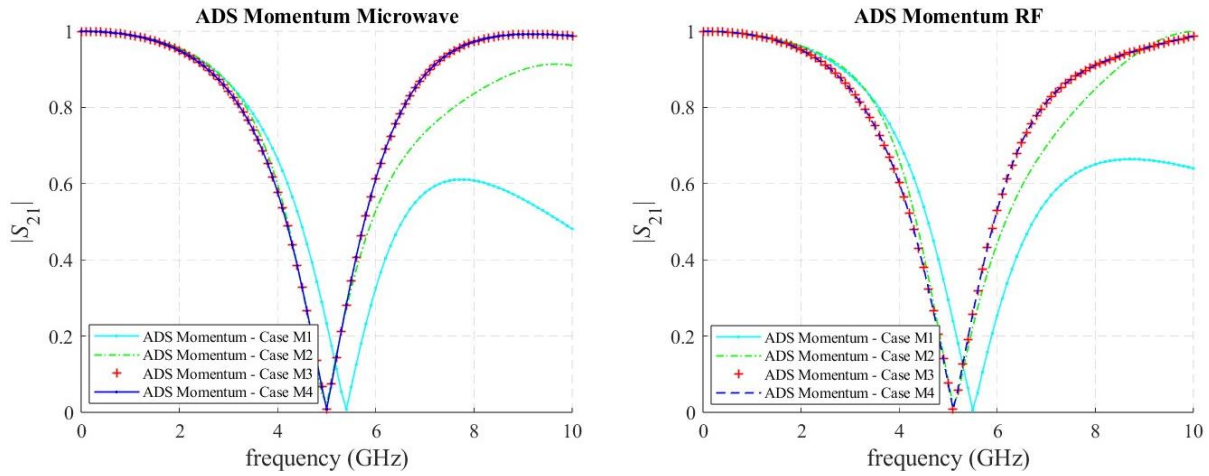

Fig. 1.6 Microstrip single-stub band-stop filter EM response at x_f^* for Cases M1 to M4: a) ADS Momentum Microwave, b) ADS Momentum RF.

wave EM models [Swanson-91], [Mirotznik-97], [Dunn-14] aim at directly solving Maxwell equations for the actual physical structure with no circuit approximation, by discretizing the structure into many small cells and approximating Maxwell's differential equations by algebraic linear equations at each small cell. The higher the resolution of the discretization (the smaller the cells), the higher the accuracy of the EM simulation. The default full-wave EM model used by Keysight ADS is based on the Method of Moments (MoM) [Harrington-67], [Rautio-03], and its commercial name is Momentum [Keysight-22].

In this section, the responses of all the microstrip filters considered are obtained following

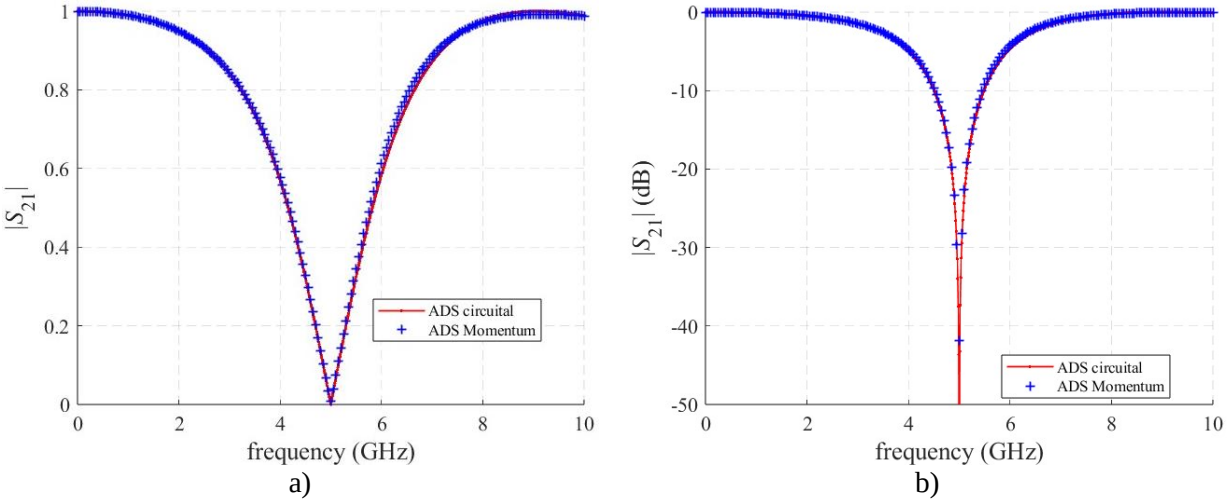

Fig. 1.7 Optimal responses for the microstrip single-stub band-stop filter for $\boldsymbol{R}_c(x_c^*)$ (ADS circuit model at its optimal design parameter) and $\boldsymbol{R}_f(x_f^*)$ (ADS Momentum Microwave model at its optimal design parameter): a) in decimal scale, b) in dB.

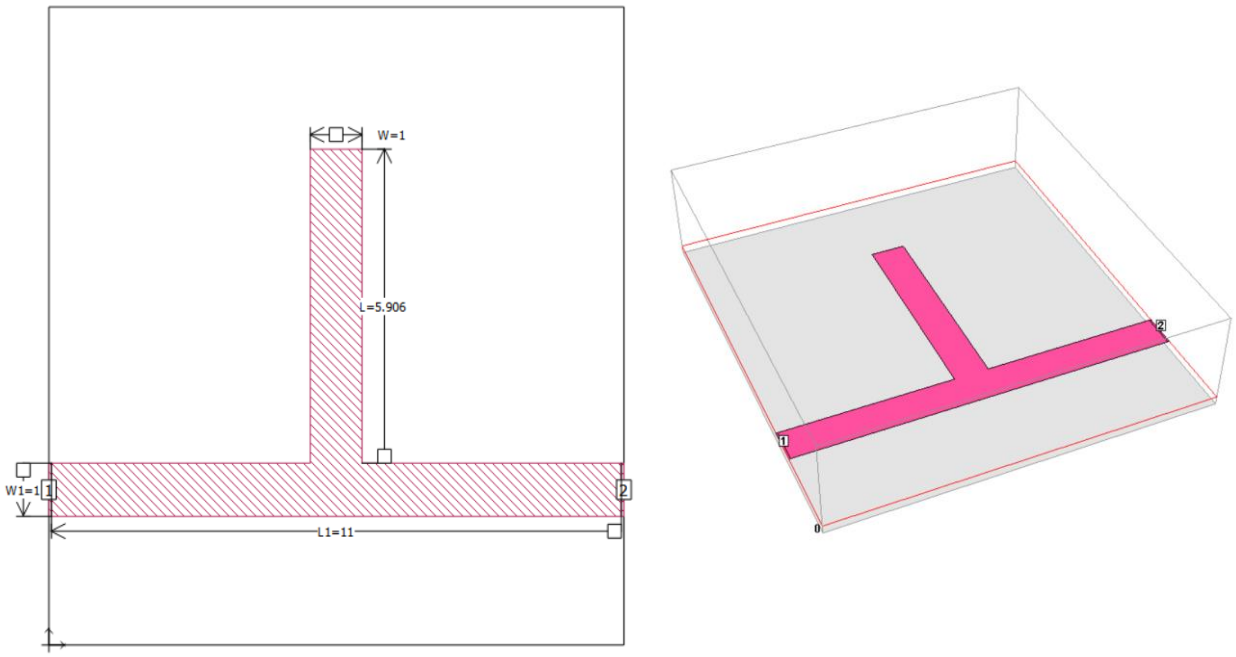

a) b)

Fig. 1.8 Geometry structure of the microstrip single-stub band-stop filter as implemented.

these steps: 1) a circuit model is first created, and the corresponding S-parameters are obtained; 2) a layout is automatically created from the circuit model and its circuit simulation is performed to get more accurate results. Then, these electromagnetic models implemented in ADS Momentum

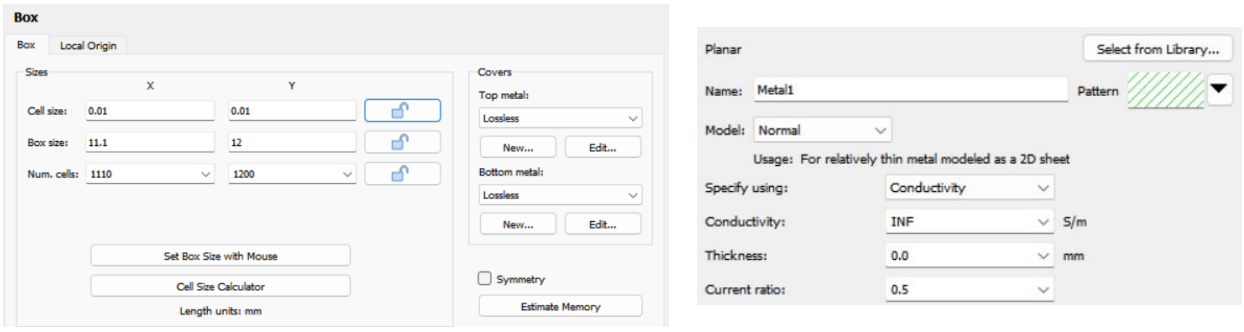

a) b)

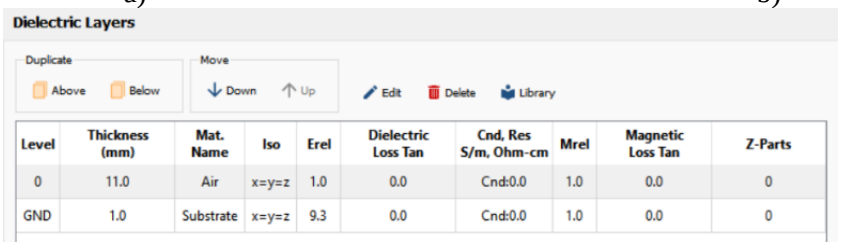

Level	Thickness (mm)	Mat. Name	Iso	Erel	Dielectric Loss Tan	Cnd, Res S/m, Ohm-cm	Mrel	Magnetic Loss Tan	Z-Parts
0	11.0	Air	x=y=z	1.0	0.0	Cnd:0.0	1.0	0.0	0
GND	1.0	Substrate	x=y=z	9.3	0.0	Cnd:0.0	1.0	0.0	0

c)

Fig. 1.9 Sonnet configuration for the microstrip single-stub band-stop filter: a) cell sizes, b) conductors, c) dielectrics.

TABLE 1.2. CONFIGURATION OF SONNET FOR THE MICROSTRIP BAND-STOP FILTER

Case	Cell size X (mm)	Cell size Y (mm)	Num. cells X	Num. cells Y	Simulation time (hr:min:sec)
S1	0.01	0.01	1110	1120	0:01:56
S2	0.005	0.005	2220	2240	0:10:55

are validated for several filters in microstrip technology [Loera-Díaz-22].

1.3. Microstrip Single-Stub Band-Stop Filter

Let us consider the microstrip single-stub band-stop filter based in the filter reported in [Koziel-08] (see Fig. 1.1). Some parameter values are modified in the filter used in this chapter with respect to those used in [Koziel-08].

1.3.1 Single-Stub Band-Stop Filter Description

In this chapter, as mentioned, some parameters have been modified with respect to those in [Koziel-08], as described in [Loera-Díaz-23b]. Fig. 1.2 shows the geometrical structure of the microstrip single-stub band-stop filter used in this chapter.

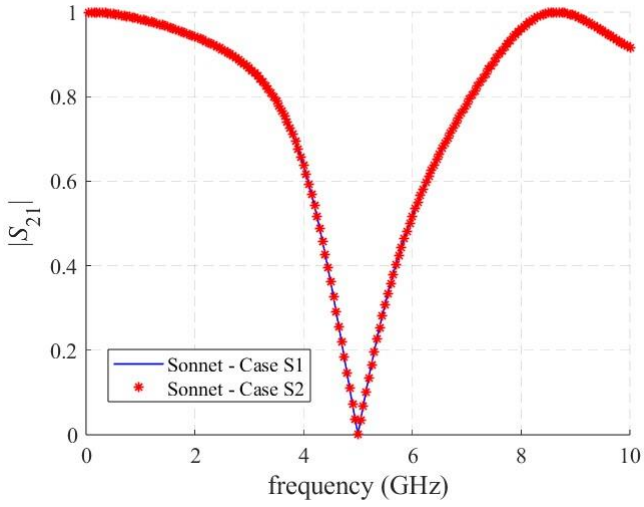

Fig. 1.10 Microstrip single-stub band-stop Sonnet responses for Case S1 and Case S2.

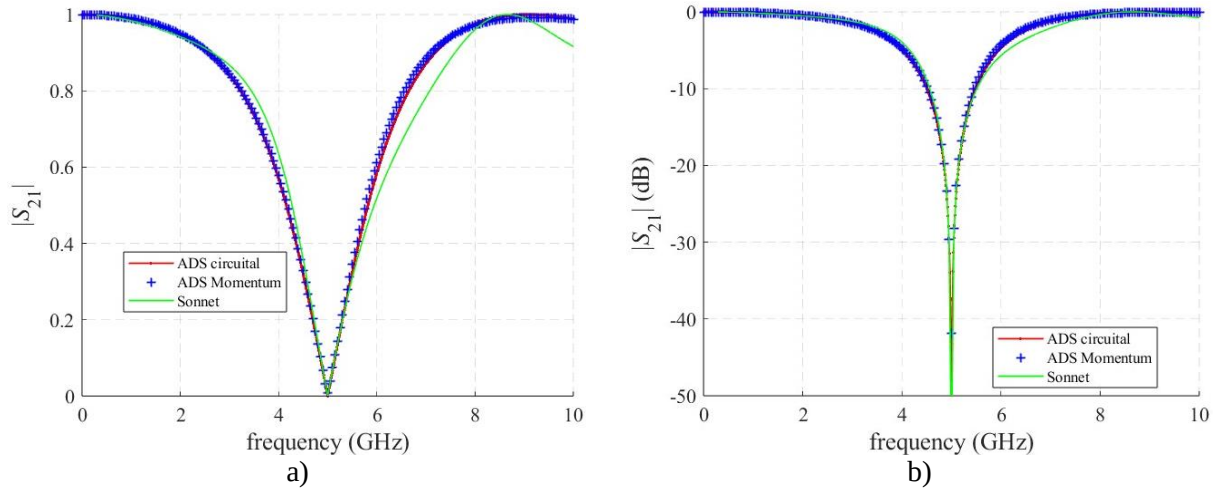

Fig. 1.11 Microstrip single-stub band-stop filter response at x_c^* of the ADS circuit model versus the filter responses at x_f^* of the EM models in ADS Momentum Microwave and Sonnet: a) in decimal scale, b) in dB.

As mentioned in [Loera-Díaz-23b] and [Loera-Díaz-25c], this band-stop microstrip filter has only one design parameter $x = L$ (mm). The pre-assigned parameters are $\boldsymbol{z} = [H \;\; \varepsilon_r \;\; W \;\; L_1]^T$, with a substrate thickness H = 1 mm, relative dielectric permittivity ε_r = 9.3, microstrips width W = 1 mm, and input/output microstrips length L_1 = 5 mm. These values of H, ε_r , and W yield a microstrip characteristic impedance Z_0 = 50.04 Ω ≈ 50 Ω. In this example, losses are neglected and metals are considered as infinitesimally thin perfect conductors, *i.e.*, the loss tangent tan(δ) =

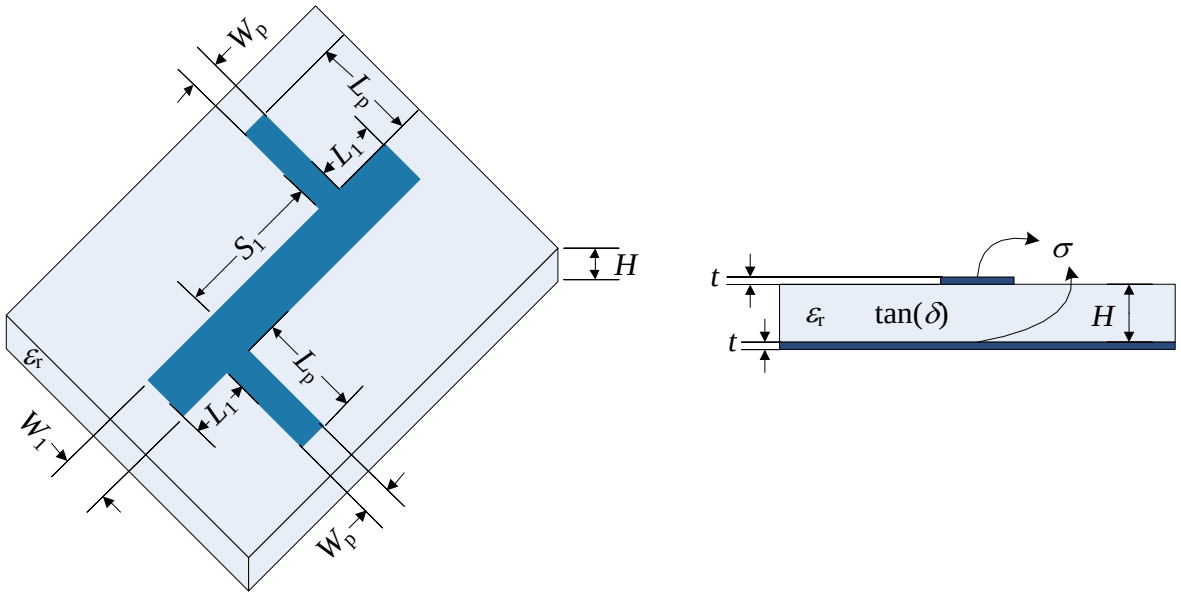

Fig. 1.12 Low-pass filter in microstrip technology [Sheen-90], [Loera-Díaz-25c]. Figure taken from [Rayas-Sánchez-12a].

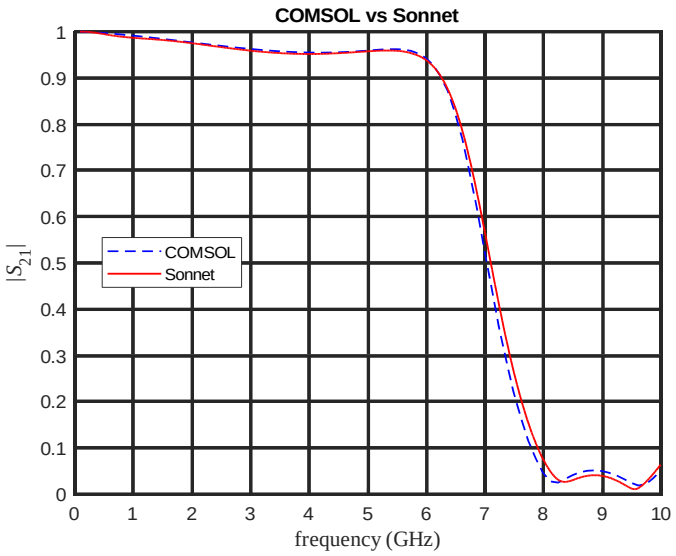

Fig. 1.13 Low-pass filter response at $\boldsymbol{x}_f^*$ in COMSOL and Sonnet obtained with data from [Rayas-Sánchez-12a].

0, the metal thickness $t = 0$, and the conductivity σ is infinite (see Fig. 1.2).

1.3.2 Single-Stub Band-Stop Filter: ADS Momentum Configuration

The circuit model in ADS of this filter is shown in Fig. 1.3. The fine model of this filter is

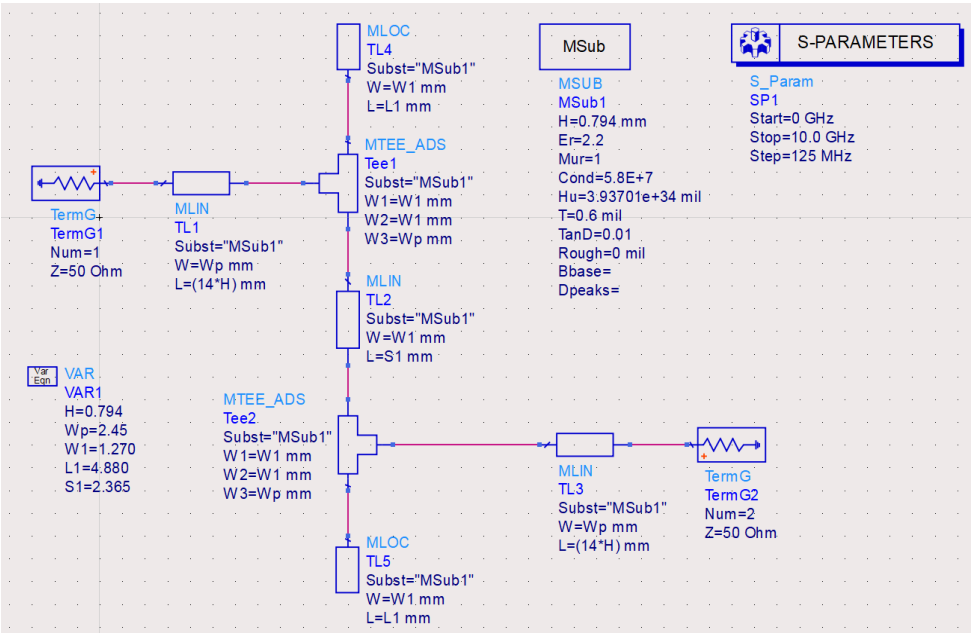

Fig. 1.14 Circuit model in ADS for the microstrip low-pass filter.

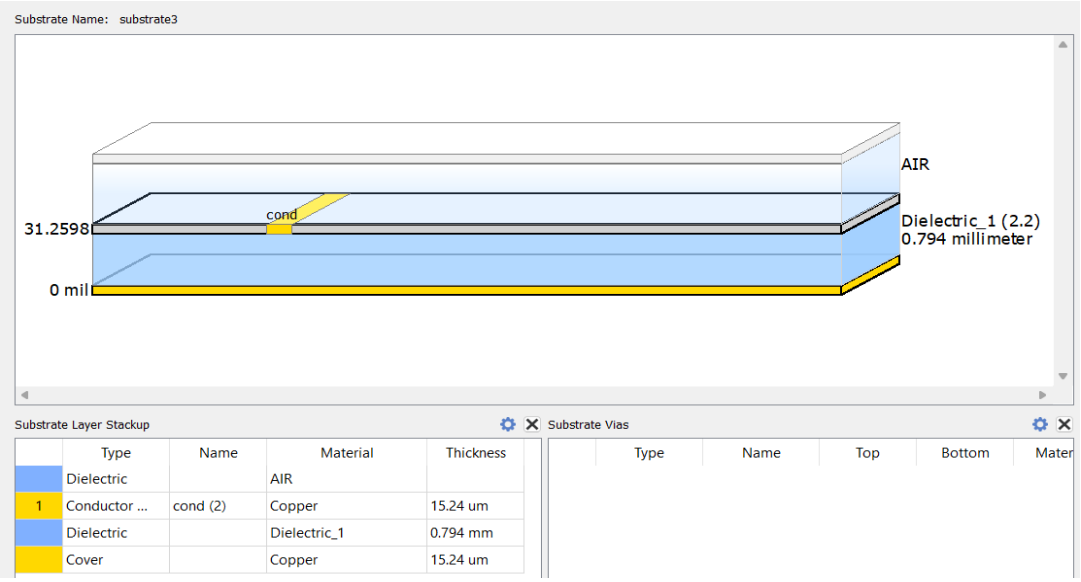

Fig. 1.15 Substrate configuration in ADS Momentum for the low-pass microstrip filter.

the full-wave EM model in ADS Momentum Microwave. The layout structure shown in Fig. 1.4 is generated in ADS from the circuit model. This layout is used to perform the full-wave EM simulation of the microstrip filter using ADS Momentum Microwave [Loera-Díaz-22], [Loera-Díaz-23a]. The optimal value for the fine model is $x_f^* = 5.906$ mm. In a similar way than the circuit model, this optimal design was obtained with a simple tuning method for the layout model in ADS Momentum.

To obtain reliable EM responses [Rayas-Sánchez-21b], the mesh dimension and other parameters of this microstrip band-stop filter are varied until response convergence is reached, as mentioned in [Loera-Díaz-22]. Table 1.1 summarizes the four configuration cases considered for ADS Momentum: M1 to M4. Fig. 1.5 shows the layout mesh for each of these cases.

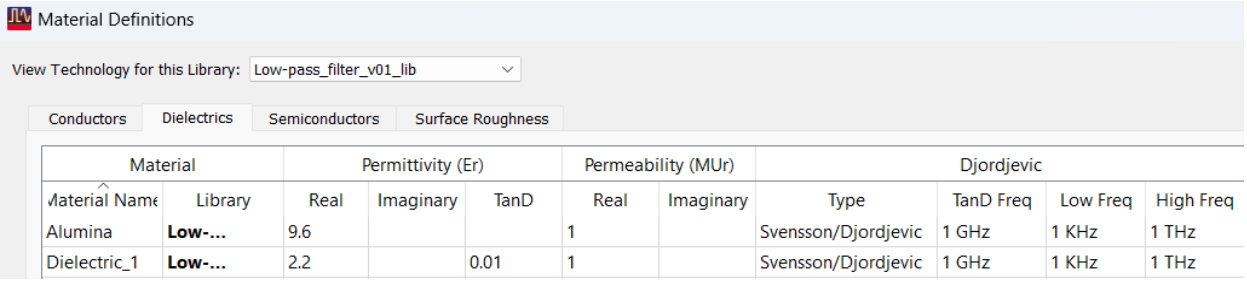

Fig. 1.16 Dielectric configuration in ADS Momentum for the low-pass microstrip filter.

S-parameter Ports

Number	Gnd Layer	Name	Feed Type	Ref Impedance [Ohm]	Ref Offset [mil]	Term Type
1	<Implicit>	P1	TML	50 + 0i	0	jumper
P1						
Gnd						
2	<Implicit>	P2	TML	50 + 0i	0	jumper
P2						

Layout Pins

Name	Layer	Net	Connected to	Purpose	X [mil]	Y [mil]	Number	Layer Num
P1	cond	P1	1(+)	drawing	0	56	1	2
P2	cond	P2	2(+)	drawing	925.276	-133.568	2	2

Fig. 1.17 Recommended port feed configuration for microstrip filters [Rayas-Sánchez-21b].

The EM simulations shown in Table 1.1 for this band-stop filter use 101 frequency points per frequency sweep. All the simulations performed in this chapter are done in a computer with a processor AMD[2] Ryzen® 7 5700U, with AMD Radeon® Graphics 1.80 GHz, and 16 GB RAM.

Fig. 1.6 shows the EM simulation responses for each case described in Table 1.1, showing that x_f^* is practically valid for configurations M2 to M4. The simulation responses obtained with ADS Momentum Microwave are regarded as more accurate than those obtained with ADS Momentum RF, as also verified in [Loera-Díaz-22].

We can see from Fig. 1.6 that the simulation response for Case M3 and Case M4 are practically the same. However, the simulation time for Case M3 is much faster than that one of

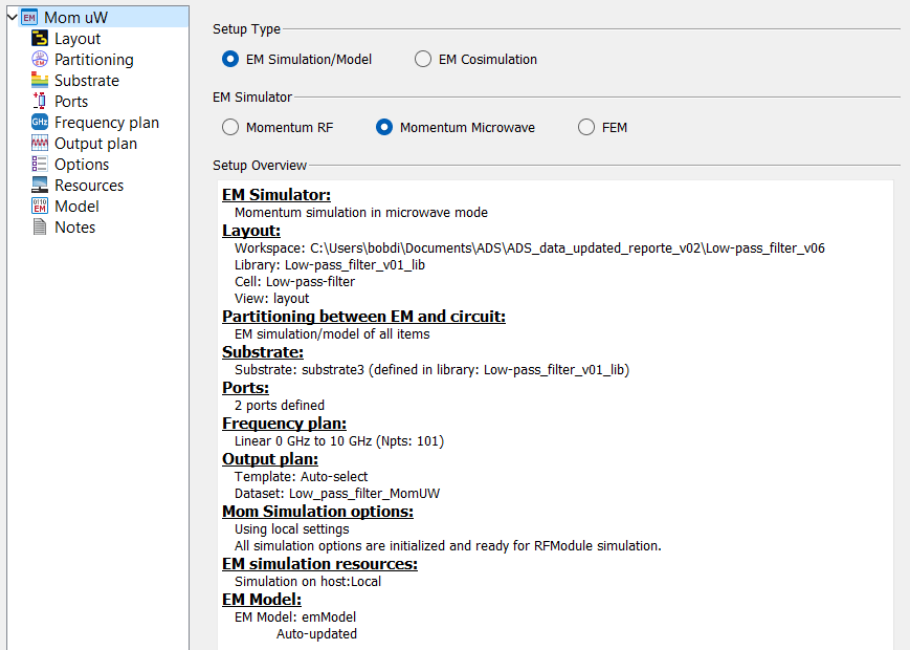

Fig. 1.18 Selecting the type of ADS EM simulator.

[2] Advanced Micro Devices (AMD) Inc., 2485 Augustine Drive, Santa Clara, CA 95054.

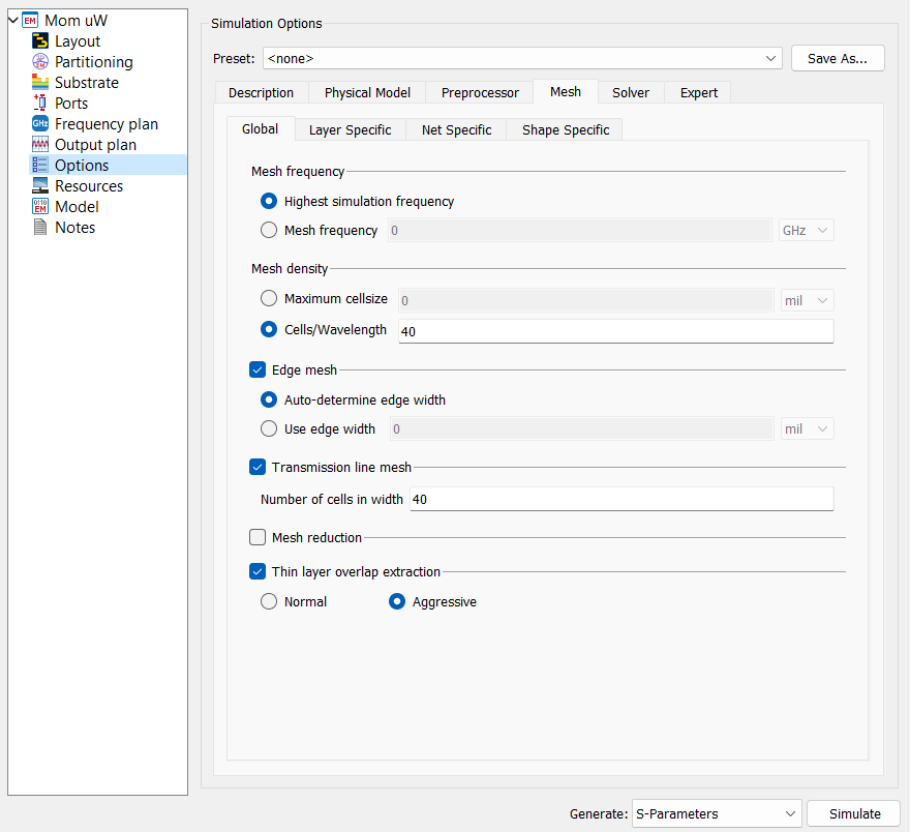

Fig. 1.19 Simulation options in ADS Momentum regarding the discretization or mesh generation.

Case M4. Therefore, the full-wave EM simulation response used as fine model in this chapter is the response obtained for Case M3 with ADS Momentum Microwave.

The configuration for Case M3 uses TML feed ports; a mesh density of 20 cells per wavelength; edge mesh option enabled, with an edge width as auto-determined; transmission line mesh option enabled, with 10 cells in width; and the thin layer overlap extraction option is selected as "aggressive", as summarized in Table 1.1.

Fig. 1.7 shows the responses for this single-stub band-stop filter for the ADS circuit model at is optimal design parameter $\boldsymbol{R}_c(x_c^*)$ against the ADS Momentum Microwave model at its optimal design parameter $\boldsymbol{R}_f(x_f^*)$.

1.3.3 Single-Stub Band-Stop Filter: ADS Momentum Simulation Responses and Validation

In addition to the full-wave EM response obtained with ADS Momentum, a full-wave EM

TABLE 1.3. CONFIGURATION OF ADS MOMENTUM FOR THE LOW-PASS MICROSTRIP FILTER

Case	Mesh density (cells/λ)	Edge mesh	Transmission line mesh	Thin layer overlap extraction	Port feed type	Simulation time (hr:min:sec)	
						Momentum Microwave	Momentum
1	1	not used	not used	Normal	Auto	0:00:05	0:00:03
2	5	not used	not used	Normal	Auto	0:00:05	0:00:03
3	20	Auto	not used	Normal	Auto	0:00:08	0:00:05
4	20	Auto	not used	Normal	TML	0:00:18	0:00:07
5	20	Auto	not used	Aggressive	TML	0:00:21	0:00:09
6	20	Auto	10	Aggressive	TML	0:02:38	0:00:51
7	20	Auto	20	Aggressive	TML	0:08:49	0:04:45
8	40	Auto	40	Aggressive	TML	1:08:18	0:36:25

response is also obtained with Sonnet[3] to validate these responses. Fig. 1.8a shows the filter layout made in Sonnet. The values shown in this figure are in mm. Fig. 1.8b shows a 3-D view of this filter layout.

Fig. 1.9 shows the configuration parameters for Sonnet. Two simulation cases are considered by varying the cell size. Fig. 1.9a shows the cell sizes considered in one of these two cases. The rest of the configuration remains the same for these two cases. A perfect conductor is considered, as illustrated in Fig. 1.9b, with a dielectric thickness of 1.0 mm, as shown in Fig. 1.9c. The distance from the horizontal microstrip line to the bottom metallic wall is around 2*W*, and the distance from the open stub to the upper metallic wall is around 2.5*W*.

The two configuration cases considered in Sonnet are denoted as S1 and S2. Case S1 uses a cell size of 0.01 mm for the X-axis with 1110 cells, and 0.01 mm for the Y-axis with 1,200 cells. Case S2 uses a size of 0.005 mm for the X-axis with 2,220 cells, and 0.005 mm for the Y-axis with 2,240 cells. Cases S1 and S2 are summarized in Table 1.2. These simulations were performed in the same computer described in Section 1.3.2. The responses from both configuration cases are shown in Fig. 1.10, confirming that they produce the same responses, however, Case S1 is much faster than Case S2. Therefore, the Sonnet response obtained for Case S1 is used for the next comparisons.

[3] Sonnet v18.52, Sonnet Software Inc., North Syracuse, NY, 2022, http://www.sonnetsoftware.com/.

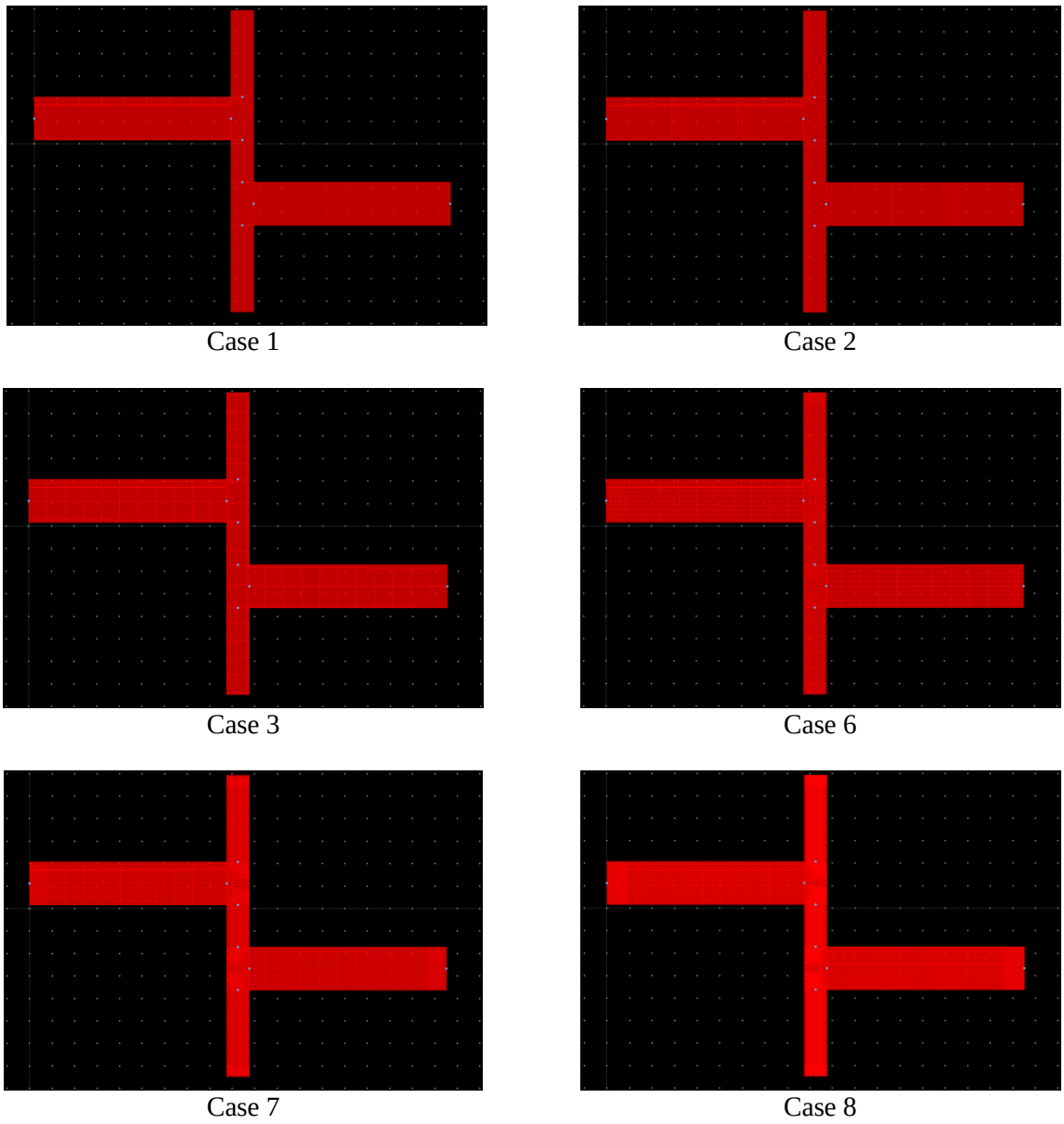

Fig. 1.20 Low-pass filter mesh for Cases 1, 2, 3, 6, 7 and 8 (see Table 1.3).

A comparison between the ADS Momentum Microwave response and the Sonnet response, both at x_f^*, is shown in Fig. 1.11, confirming a quite acceptable agreement that validates our EM full-wave responses. Fig. 1.11 also shows the circuit model response at x_c^*.

1.4. Microstrip Low-Pass Filter

The next filter to be described is a microstrip low-pass filter [Sheen-90] illustrated in Fig.

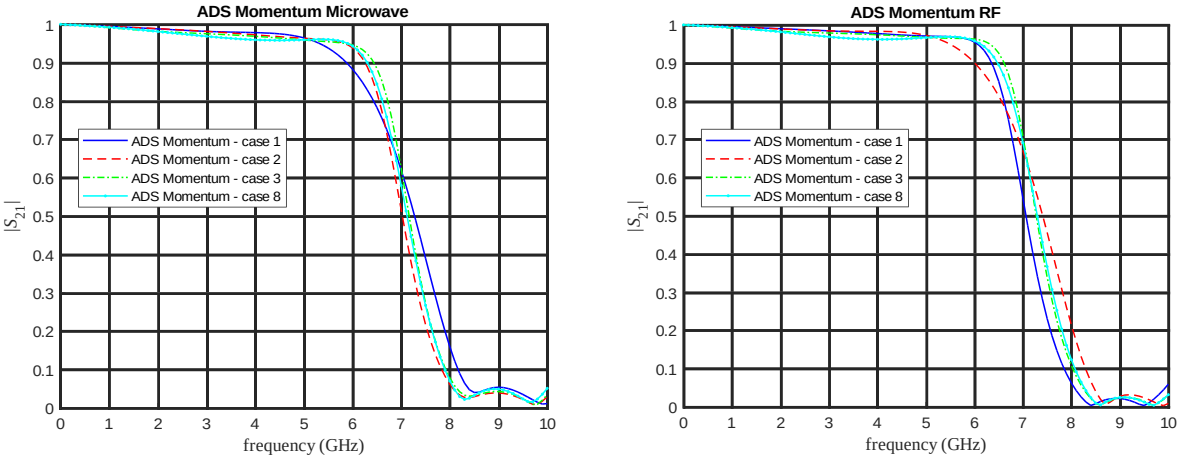

Fig. 1.21 Low-pass filter response at $\boldsymbol{x}_f^*$ for Cases 1, 2, 3 and 8: a) ADS Momentum Microwave, b) ADS Momentum RF.

1.12. This filter has also been studied in [Rayas-Sánchez-12a], [Rayas-Sánchez-12b], [D'Inzeo-79], [Loera-Díaz-22].

1.4.1 Low-Pass Filter Description

This filter has input-output 50-Ω microstrip symmetrical lines separated by a distance S_1 with a microstrip line with a width W_1 and open stubs with length L_1. The input-output 50-Ω microstrip lines have a width W_p = 2.45 mm and a length $L_p = 14H$.

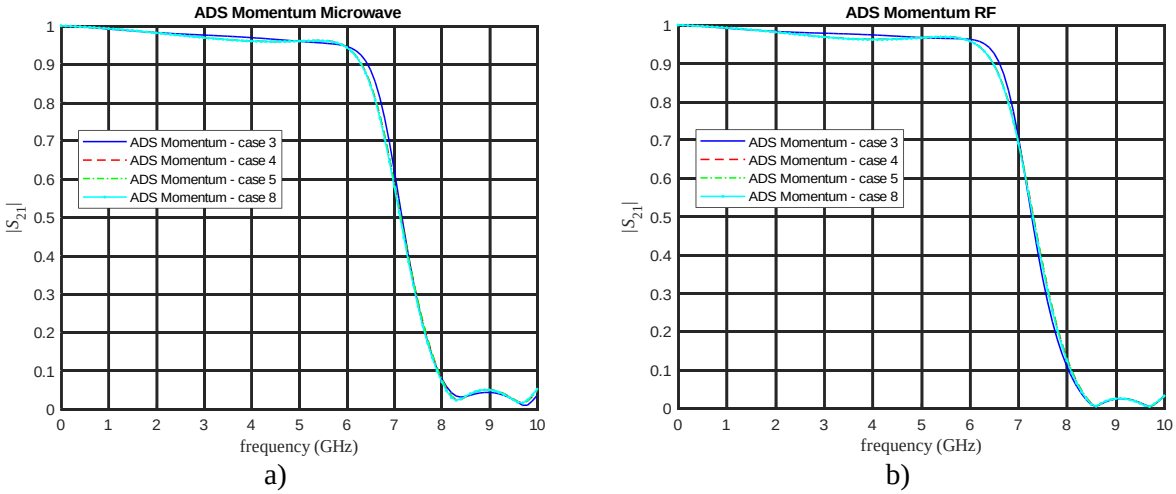

Fig. 1.22 Low-pass filter response at $\boldsymbol{x}_f^*$ for Cases 3, 4, 5 and 8: a) ADS Momentum Microwave, b) ADS Momentum RF.

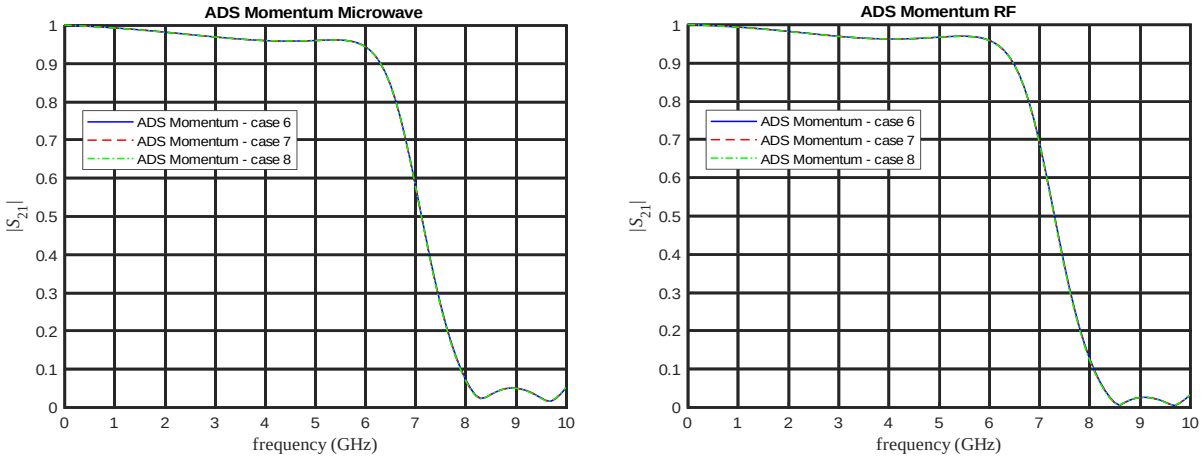

Fig. 1.23 Low-pass filter response at $\boldsymbol{x}_f^*$ for case 6, 7 and 8: a) ADS Momentum Microwave, b) ADS Momentum RF.

This filter also has a substrate thickness H = 0.794 mm, relative dielectric permittivity ε_r = 2.2, and loss tangent tan(δ) = 0.01. Metal traces and ground plane both are copper with thickness t = 0.6 mil = 15.24 μm and electrical conductivity $\sigma = 5.8\times10^7$ S/m.

This low-pass filter has three design parameters that are typically used as optimization variables in vector $\boldsymbol{x} = [W_1 \;\; L_1 \;\; S_1]^T$. The optimization pre-assigned parameters are $\boldsymbol{z} = [H \;\; \varepsilon_r \;\; W_p \;\; L_p \;\; \tan(\delta) \;\; \sigma \;\; t]^T$ [Loera-Díaz-25c]. The optimal values found in [Rayas-Sánchez-12a], for the fine model (full-wave EM model) of this filter are $\boldsymbol{x}_f^* = [1.270 \;\; 4.880 \;\; 2.365]^T$ (mm). Fig. 1.13 shows the responses in COMSOL[4] and Sonnet of this low-pass filter at $\boldsymbol{x}_f^*$ [Rayas-Sánchez-12a].

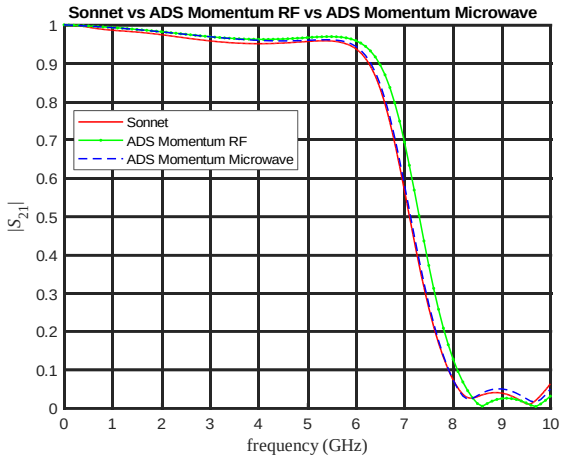

Fig. 1.24 Low-pass filter response at $\boldsymbol{x}_f^*$ with Sonnet, ADS Momentum Microwave and ADS Momentum RF using the best configuration (Case 6).

[4] COMSOL Modeling Software, COMSOL Inc., 100 District Avenue, Burlington, MA01803

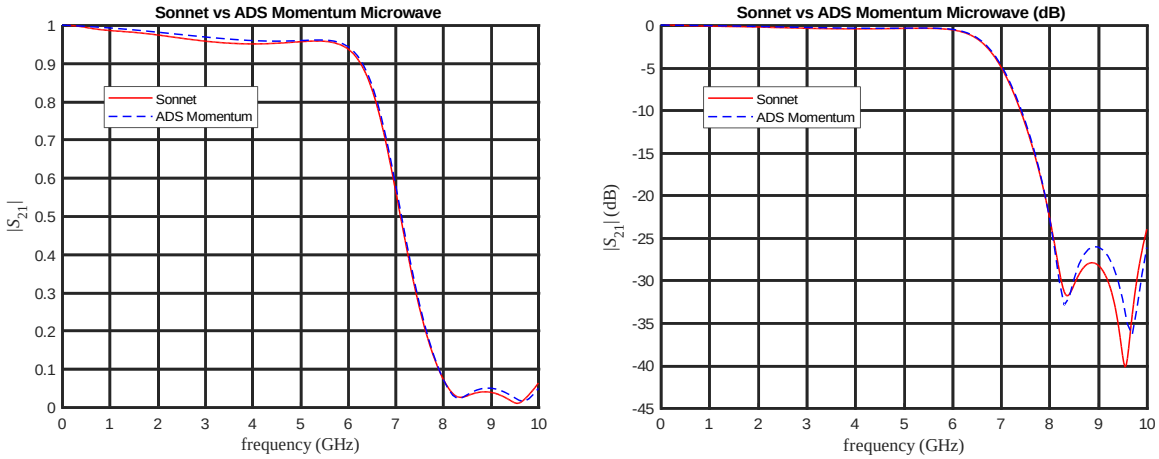

a) b)

Fig. 1.25 Low-pass filter response at $\boldsymbol{x}_f^*$ with Sonnet and ADS Momentum Microwave using the best configuration (Case 6): a) $|S_{21}|$, b) $|S_{21}|$ (dB).

1.4.2 Low-Pass Filter: ADS Momentum Configuration

As mentioned, to get reliable simulation responses, the EM simulator must be properly configured [Rayas-Sánchez-21b]. This section also describes a method to configure ADS Momentum to obtain reliable full-wave EM simulation responses of this microstrip low-pass filter.

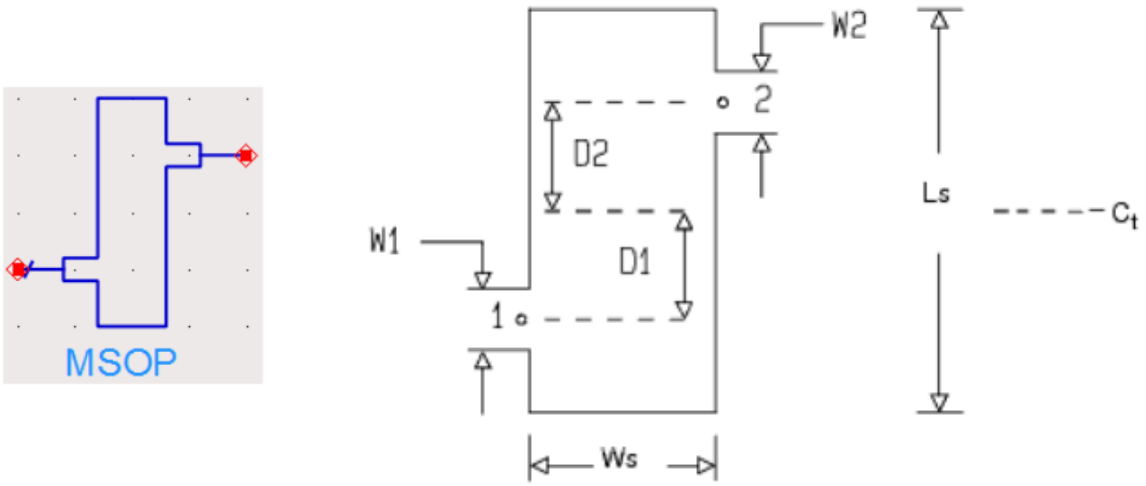

a) b)

Fig. 1.26 MSOP component from ADS, a) symbol, b) structure geometry. Figures taken from ADS help.

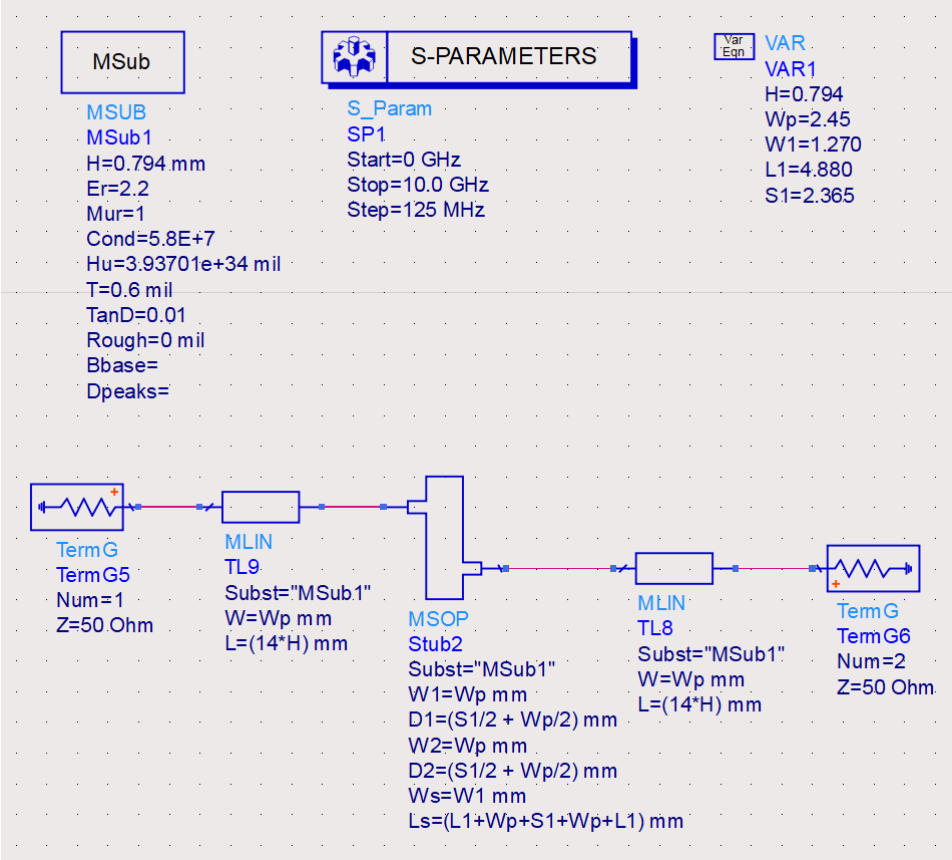

Fig. 1.27 Second circuit model in ADS for the microstrip low-pass filter (Model 2).

Fist, a circuit model of the filter is created in ADS as shown in Fig. 1.14, with all the parameters mentioned in the filter description. Then, a layout is generated from this circuit model. This layout is used to perform the full-wave EM simulation.

All the filter parameters must also be included in the layout model. Fig. 1.15 shows the substrate configuration, the dielectric layers and the kind of metal with their respective thickness. Fig. 1.16 shows the relative dielectric permittivity ε_r and loss tangent tan(δ).

Even using the same structure, dielectric, and material characteristics, the EM simulation response might be different depending on the configuration of some other parameters, such as the port feed and mesh [Rayas-Sánchez-21b]. The configuration for the port feed type is shown in Fig. 1.17. Some test cases used in this chapter use the default parameter for the feed port, named as "Auto". Other test cases consider "TML" as feed type, as recommended in [Rayas-Sánchez-21b] (see Table 1.3, Table 1.6, and Table 1.7).

Different EM simulators can provide different responses even for the same structure. Fig. 1.18 shows the EM simulators available in ADS to perform 2-D EM simulations: Momentum

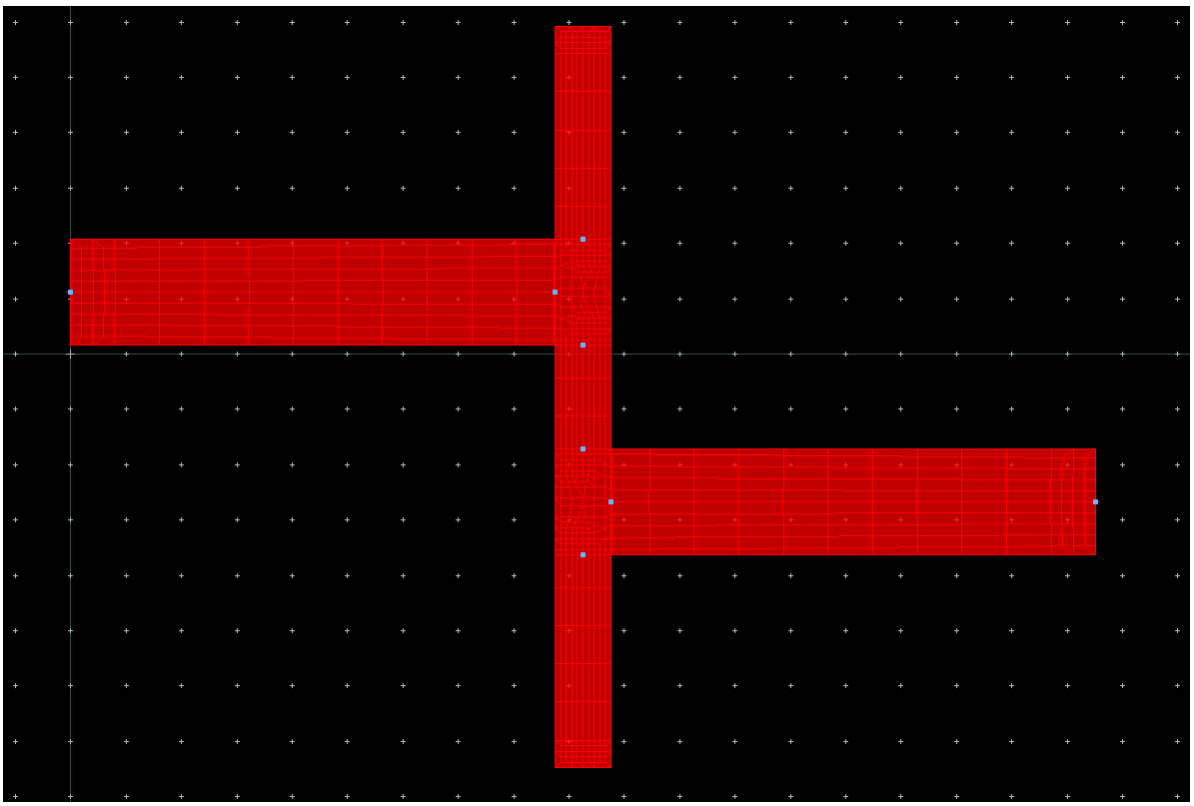

Fig. 1.28 Low-pass filter physical layout generated from Model 1 (Fig. 1.14) or Model 2 (Fig. 1.27).

Microwave and Momentum RF. This chapter compares the behavior of both. Notice that "FEM" is typically used to perform 3-D full-wave EM simulations in ADS (see Fig. 1.18).

Regarding the discretization, Fig. 1.19 illustrates some simulation options to change the mesh to be used for each simulation. The "Mesh density" option allows to change the number of cells per wavelength to be used. The "Edge mesh" option allows to obtain more accurate responses because it considers a higher density mesh at the edges of each microstrip line. Some of the configuration cases used in this chapter do not use this feature, while other cases use the "Auto-determine edge width" option. This latest option is mentioned in Table 1.3, Table 1.6, and Table 1.7 as "Auto". The "transmission line mesh" option allows to define the number of cells across the width. Finally, other simulation option is the "thin layer overlap extraction" which can be set as "normal" or "aggressive".

The EM simulations for this low-pass filter use 101 frequency points per frequency sweep.

All the simulations performed in this chapter were done in a computer with a processor AMD Ryzen® 7 5700U, with AMD Radeon® Graphics 1.80 GHz, and 16 GB RAM.

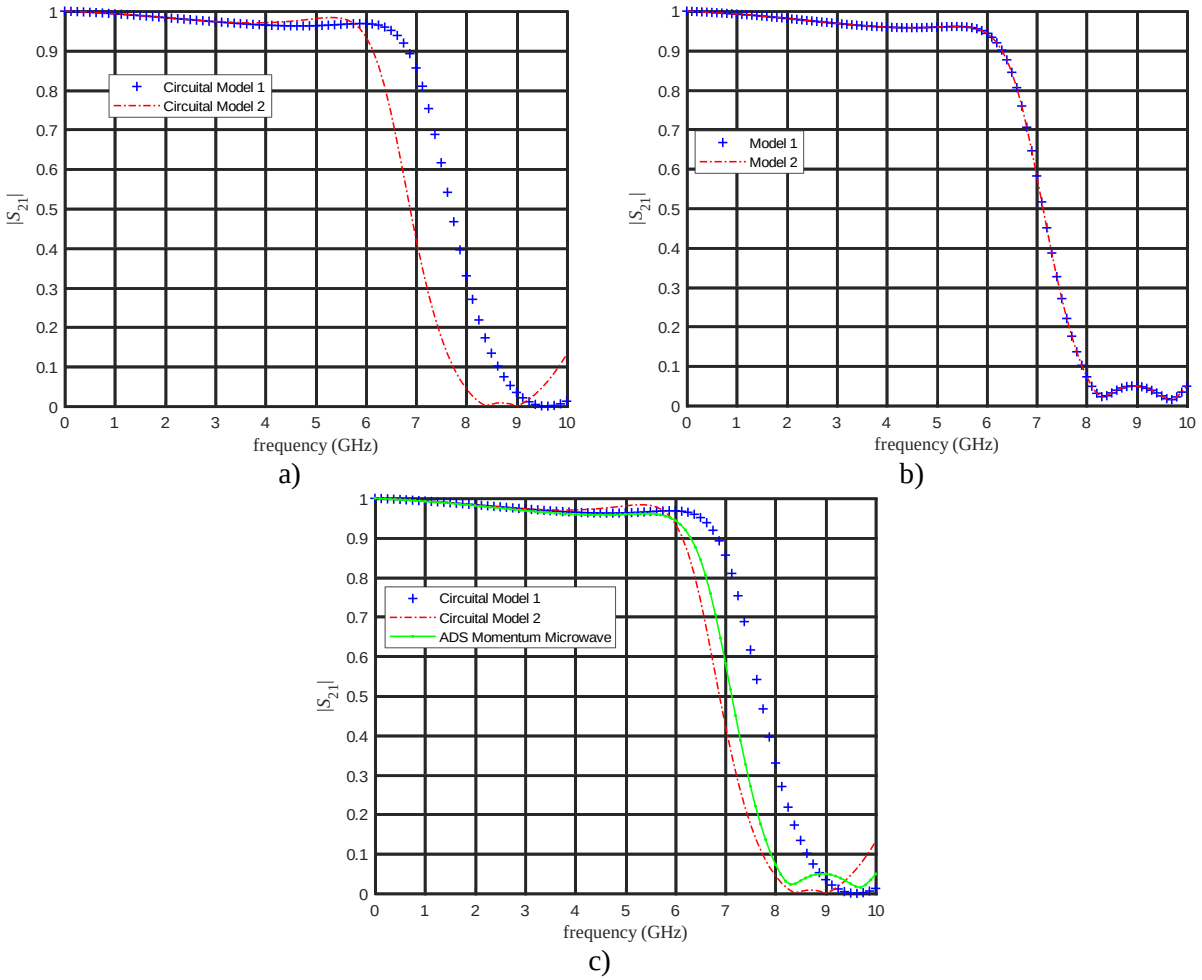

Fig. 1.29 ADS simulation responses of the low-pass filter: a) at $\boldsymbol{x}_f^*$ for circuit Models 1 and 2; b) at $\boldsymbol{x}_f^*$ for the EM Models 1 and 2. c) Comparison of simulation responses of the circuit Models 1 and 2 versus the EM simulation response from ADS Momentum Microwave.

Table 1.3 shows the simulation time for eight configuration cases, where some simulation options are changed in both ADS Momentum Microwave and ADS Momentum RF. These eight cases have been arbitrarily chosen, where Case 1 is an example of a very coarse configuration with Auto feed type, a mesh density with only one cell per wavelength, no edge mesh, and no transmission line mesh. The simulation time for Case 1 is very fast but the simulation response is not very accurate (see 1.4.3). On the other hand, Case 8 considers a mesh density with more cells per wavelength and a transmission line mesh with many cells in width. This simulation response is much more accurate (see 1.4.3), but its simulation time is too long. Cases 2 to 7 consider intermediate situations with a layout mesh between Case 1 and Case 8, as shown in Fig. 1.20. Cases 3, 4 and 5 use the same layout mesh but different configuration options (*e.g.*, feed type; see

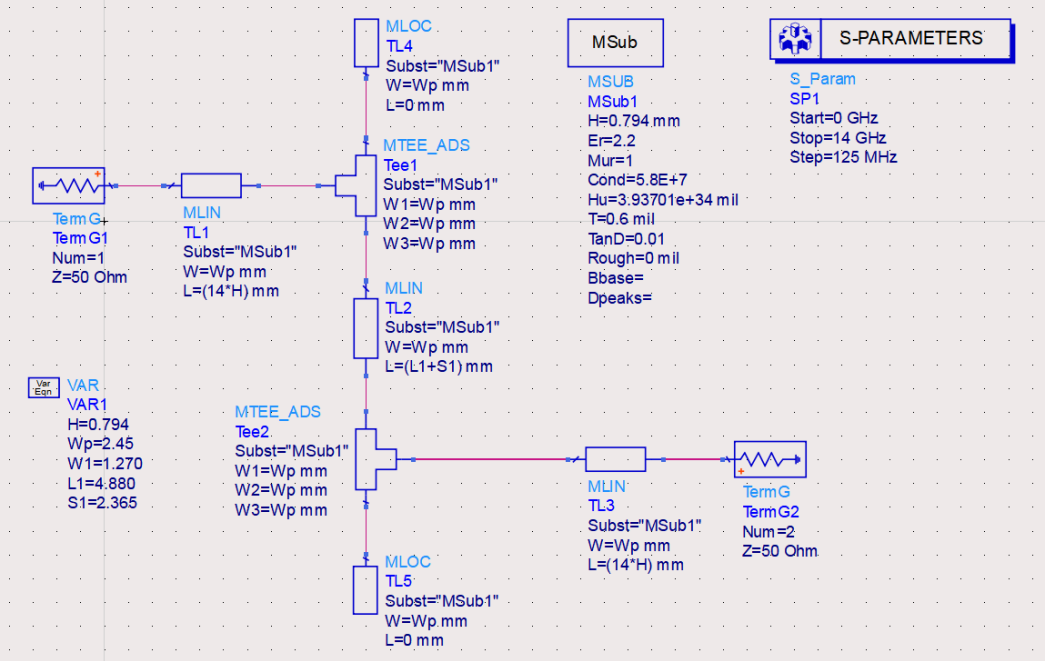

Fig. 1.30 Simple microstrip geometry using ADS components MTEE, MLOC, and MLIN.

Table 1.3). In general, Table 1.3 confirms that ADS Momentum RF is faster than ADS Momentum Microwave since the former employs some quasi-static simplifications.

1.4.3 Low-Pass Filter: ADS Momentum Simulation Responses and Validation

2-D EM simulation responses at $\boldsymbol{x}_f^*$ (optimized design parameters according to [Rayas-Sánchez-12a]) are shown in Fig. 1.21 for Cases 1, 2, 3 and 8, for both EM simulators: ADS Momentum Microwave and ADS Momentum RF. As mentioned before, Case 1 is the less accurate case while Case 8 is the most accurate one.

Fig. 1.22 shows the simulation responses for Cases 3, 4 and 5, where the layout has the same mesh, but other configuration parameters are modified. Case 8 has been included in Fig. 1.22 as reference to observe what cases have better performance. Although difficult to notice in Fig. 1.22, the responses for Cases 8, 5 and 4 are practically the same. From these responses, it is seen that the simulations with TML feed ports (Cases 5 and 4) have better performance than simulations with Auto feed port (Case 3). This can be seen for both EM simulators: ADS Momentum Microwave and ADS Momentum RF.

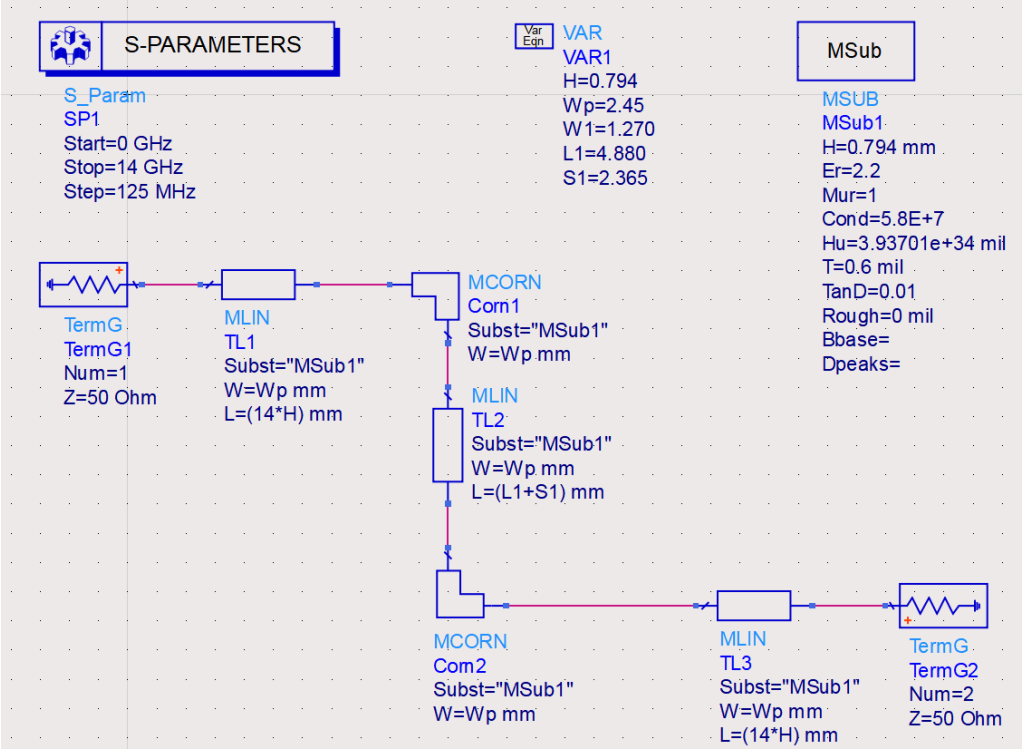

Fig. 1.31 Simple microstrip geometry using ADS components MCORN and MLIN.

Simulation responses for Cases 6, 7 and 8 are shown in Fig. 1.23. From Fig. 1.22 and Fig. 1.23, although difficult to compare, it is seen that the simulation responses for Cases 6 and 7 are slightly better than those from Cases 4 and 5. Therefore, Case 6 will be considered the one with the best behavior of these eight cases and it will be considered for the following comparisons. This is because this case has practically the same accuracy than Case 8, which is the most accurate, but the simulation time for Case 6 is much faster. Case 6 has the best performance for both, Momentum Microwave and Momentum RF.

Fig. 1.24 illustrates the simulation responses for ADS Momentum Microwave and ADS Momentum RF against the validated response from Sonnet [Rayas-Sánchez-12a]. As mentioned before, this comparison considers Case 6 because it has the best performance. Fig. 1.24 also shows that ADS Momentum Microwave has higher accuracy than ADS Momentum RF, as expected.

Finally, Fig. 1.25 shows a comparison of the 2-D EM simulation responsefrom ADS Momentum Microwave against the EM simulation response from Sonnet [Rayas-Sánchez-12a]. It can be seen from these plots that the matching between ADS Momentum Microwave and Sonnet is satisfactory.

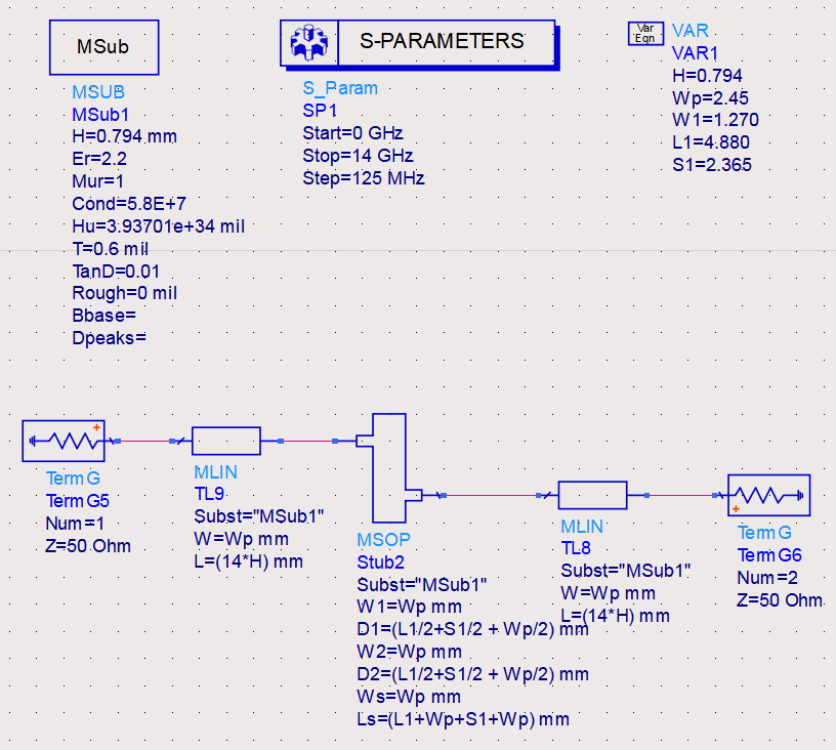

Fig. 1.32 Simple microstrip geometry using ADS components MSOP and MLIN.

1.4.4 Low-Pass Filter: Additional ADS Filter Models

Equivalent circuit models and physical layout EM models are considered for this analysis. Two circuit models are considered using different components available in ADS.

TABLE 1.4. PARAMETERS OF THE MSOP ADS COMPONENT

Name	Description	Units	Default
Subst	Substrate instance name	None	MSub1
W1	Width of input line	mil	10.0
D1	Distance between centerlines of input line and stub-pair	mil	5.0
W2	Width of output line	mil	10.0
D2	Distance between centerlines of output line and stub-pair	mil	5.0
Ws	Width of stubs	mil	10.0
Ls	Combined length of stubs	mil	30.0
Temp	Physical temperature	°C	None

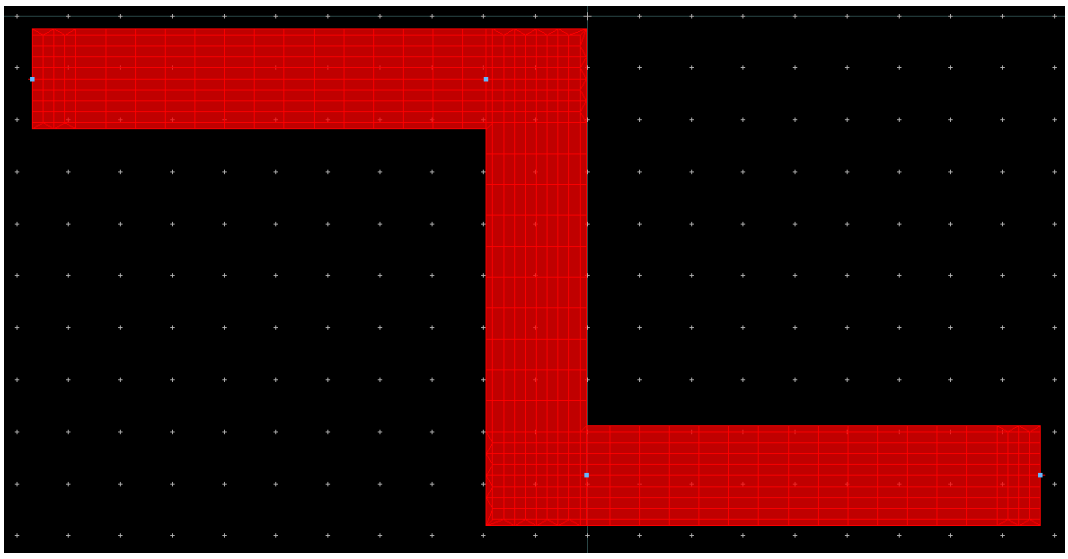

Fig. 1.33 Layout for the simple microstrip geometry obtained from the schematic in Fig. 1.30, Fig. 1.31, or Fig. 1.32.

1.4.4.1 Circuit Models

The first circuit model, referred as Model 1, is shown in Fig. 1.14 [Loera-Díaz-22]. This model uses a couple of MTEE components, a couple of MLOC components, and some MLIN components.

The second circuit model, referred as Model 2, is based on an MSOP component (also used in [Villa-Loustaunau-23]). Fig. 1.26, taken from ADS help, illustrates the ADS symbol and the geometrical structure of this ADS component, whose parameters are shown in Table 1.4. Circuit Model 2 uses an MSOP component and a couple of MLIN components, as illustrated in Fig. 1.27.

According to the ADS help, the range of validity of the MSOP component (see Table 1.4 and Fig. 1.26) is given by:

$$0.01 < \frac{W1}{H} < 100 \tag{1-1}$$

TABLE 1.5. CONFIGURATION OF ADS MOMENTUM FOR THE MICROSTRIP LOW-PASS FILTER

Mesh density (cells/λ)	Edge mesh	Transmission line mesh	Thin layer overlap extraction	Port feed type	EM Simulator
20	Auto	10	Aggressive	TML	Momentum Microwave

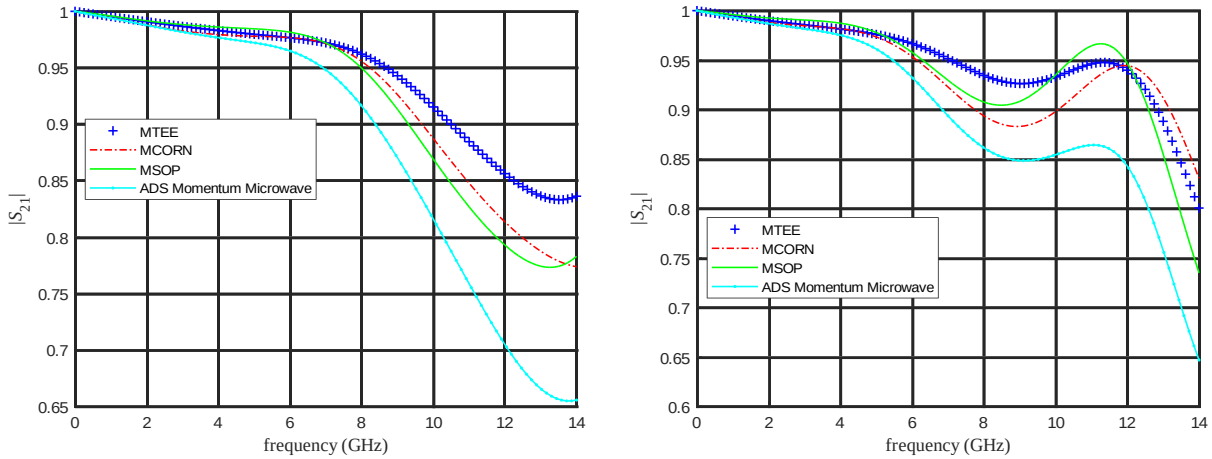

Fig. 1.34 Comparison of simulation responses of the simple microstrip geometry using circuit models in Fig. 1.30 (MTEE), Fig. 1.31 (MCORN), and Fig. 1.32 (MSOP): a) versus the EM simulation response obtained from ADS Momentum Microwave for the physical layout in Fig. 1.33; b) increasing the vertical length from L_1+S_1 to 2L_1+S_1, versus the corresponding EM simulation response.

$$0.01 < \frac{W2}{H} < 100 \tag{1-2}$$

$$0.01 < \frac{Ws}{H} < 100 \tag{1-3}$$

$$Ls > |D1 + D2| + \frac{(W1+W2)}{2} \tag{1-4}$$

where H is the thickness from the associated substrate and the remaining variables in (1-1)-(1-4) are indicated in Fig. 1.26.

1.4.4.2 Layout EM Model

A layout structure is generated from each of the two circuit models mentioned in Section 1.4.4.1. These layouts are used to perform full-wave EM simulations of the microstrip filter using ADS Momentum Microwave. Since the dimensions of both the circuit models are equivalent, they produce exactly the same layout structure. Fig. 1.28 shows the layout of the low-pass filter obtained from the circuit Model 1 or 2.

To obtain reliable full-wave EM simulation results of this low-pass filter in microstrip technology, ADS Momentum is configured following [Loera-Díaz-22] and [Rayas-Sánchez-21b]. This configuration uses: TML feed ports; a mess density of 20 cells per wavelength; edge mesh option enabled, with an edge width as auto-determined; transmission line mesh option enabled, with 10 cells in width; and the thin layer overlap extraction option is selected as “aggressive”. This

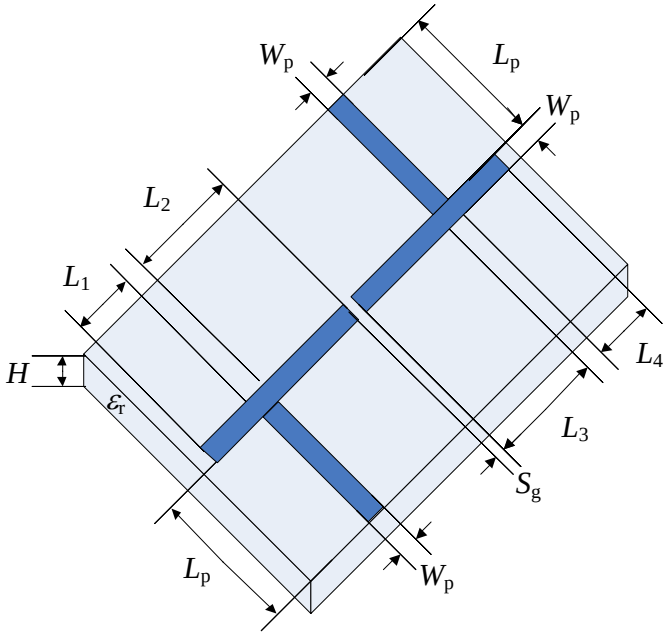

Fig. 1.35 Band-pass filter in microstrip technology [Hennings-06], [Loera-Díaz-25c]. Figure taken from [Brito-Brito-12].

configuration is summarized in Table 1.5.

1.4.4.3 Circuit Simulation Responses

The simulation results of the circuit models are shown in Fig. 1.29a. It is seen that the response from Model 1 is significantly different to that one of Model 2, despite both generate exactly the same physical layout. This implies that the internal circuit models used by ADS for these components have significant differences.

1.4.4.4 EM Simulation Responses

The full-wave EM simulation responses of the physical layout obtained from these two circuit models are shown in Fig. 1.29b. As expected, both EM simulation responses are exactly the same.

1.4.4.5 Comparing Circuit and EM Simulation Responses

Finally, Fig. 1.29c shows a comparison between the simulation responses of the circuit Models 1 and 2 against the full-wave EM simulation response obtained with ADS Momentum

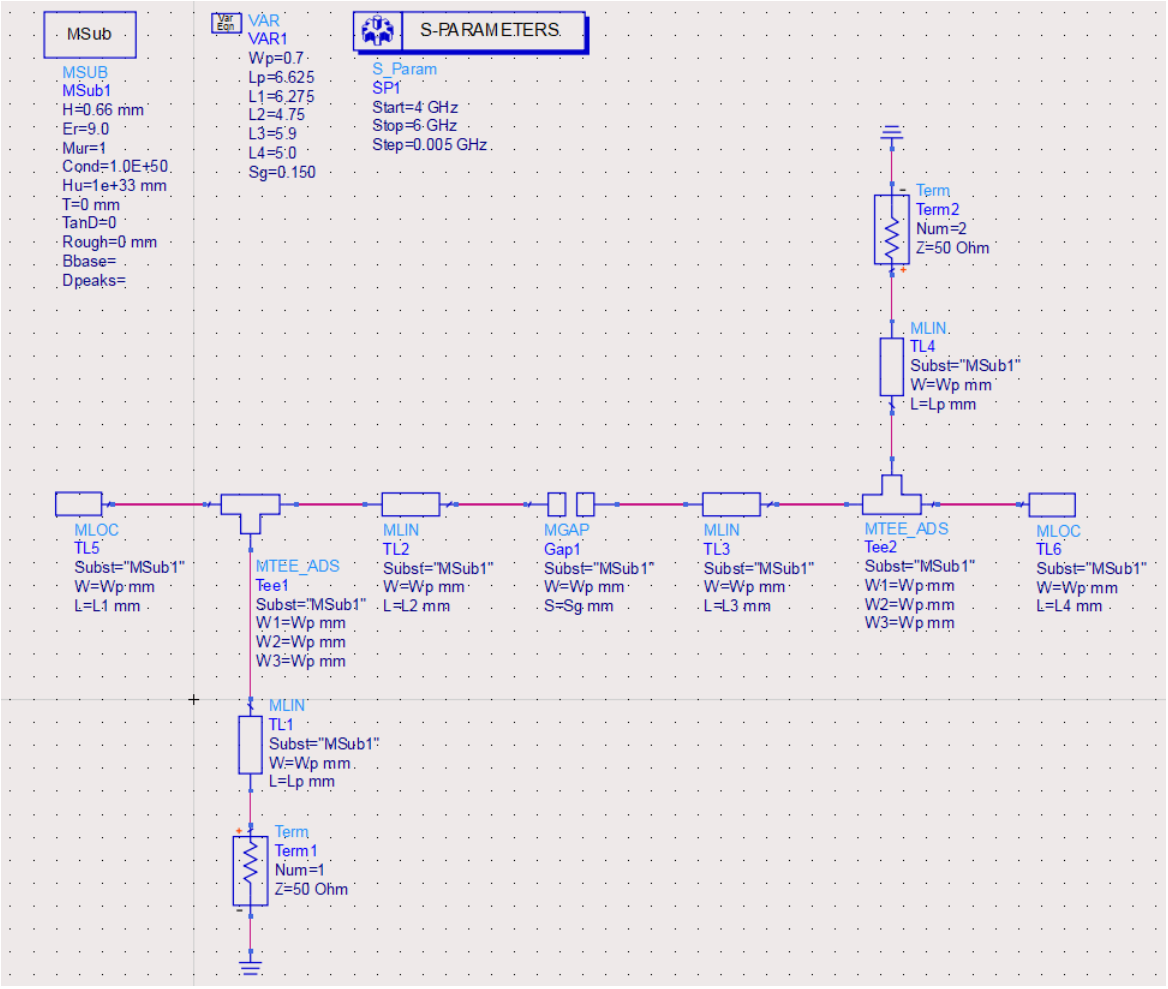

Fig. 1.36 Circuit model in ADS for the microstrip band-pass filter.

Microwave. It is seen that the response from the circuit Model 2 (using MSOP component) is more accurate than that one of circuit Model 1.

1.4.4.6 Additional Comparison of ADS Key Components

As an additional comparison of the simulation results obtained with different components available in ADS to create circuit models, in this section we focus on a simple microstrip geometry created with the following key ADS components: MTEE, MCORN and MSOP.

Fig. 1.30 shows the simple microstrip geometry using MTEE, MLOC, and MLIN ADS components. Fig. 1.31 shows the same microstrip geometry but now using MCORN and MLIN ADS component. Finally, Fig. 1.32 shows the same microstrip geometry but now using the MSOP and MLIN components.

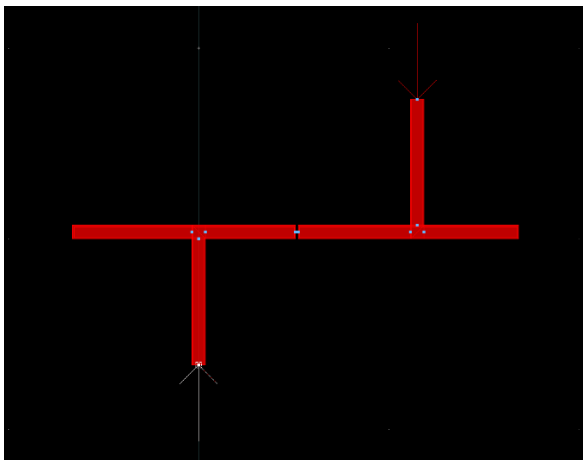

Case 1

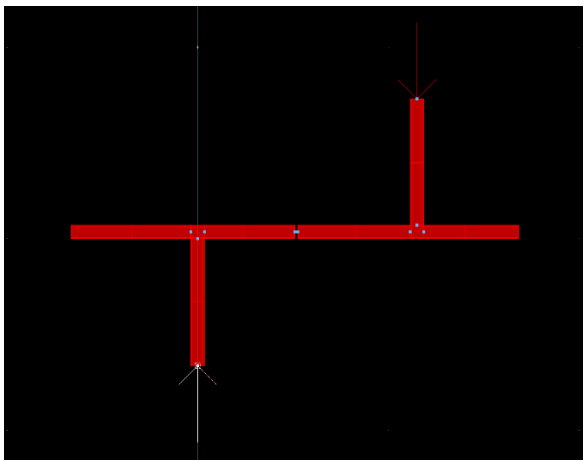

Case 2

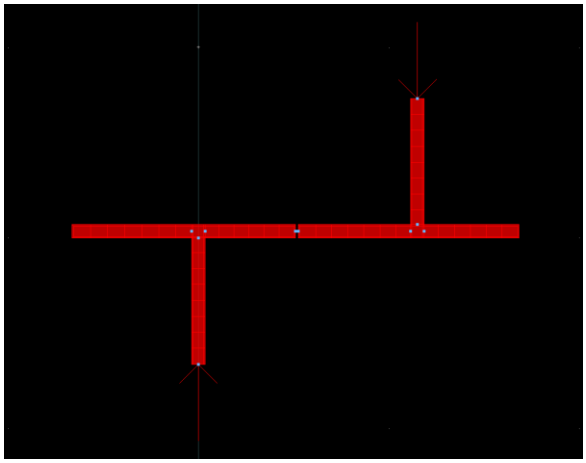

Case 3

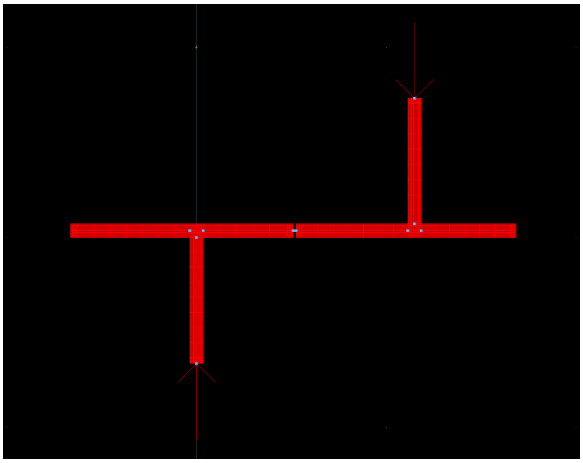

Case 4

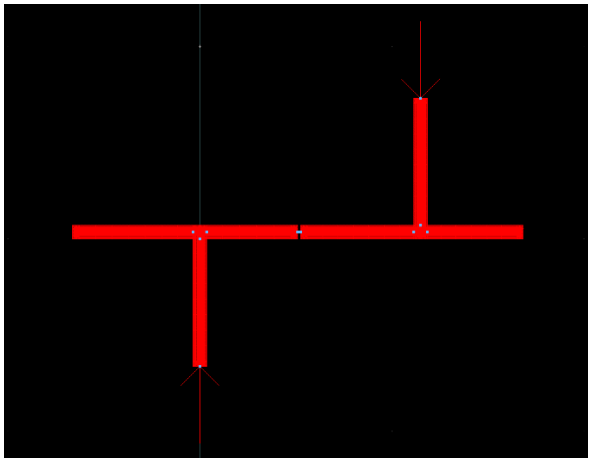

Case 5

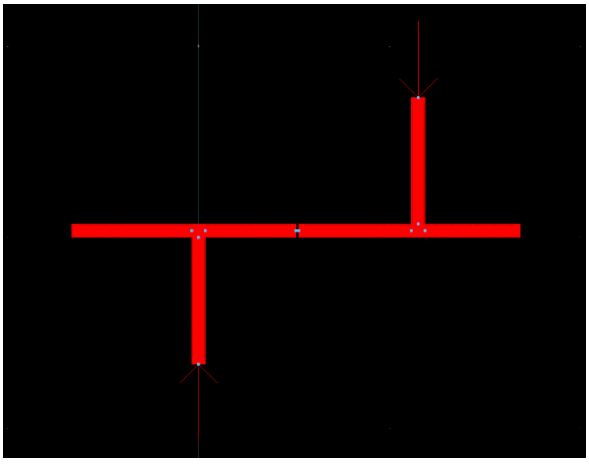

Case 6

Fig. 1.37 Low-pass filter mesh for Cases 1, 2, 3, 6, 7 and 8 (see Table 1.3).

Unlike the circuit model for the low-pass filter illustrated in Fig. 1.27, the dimensions of the MSOP circuit model for the simple microstrip structure, shown in Fig. 1.32, do not meet the

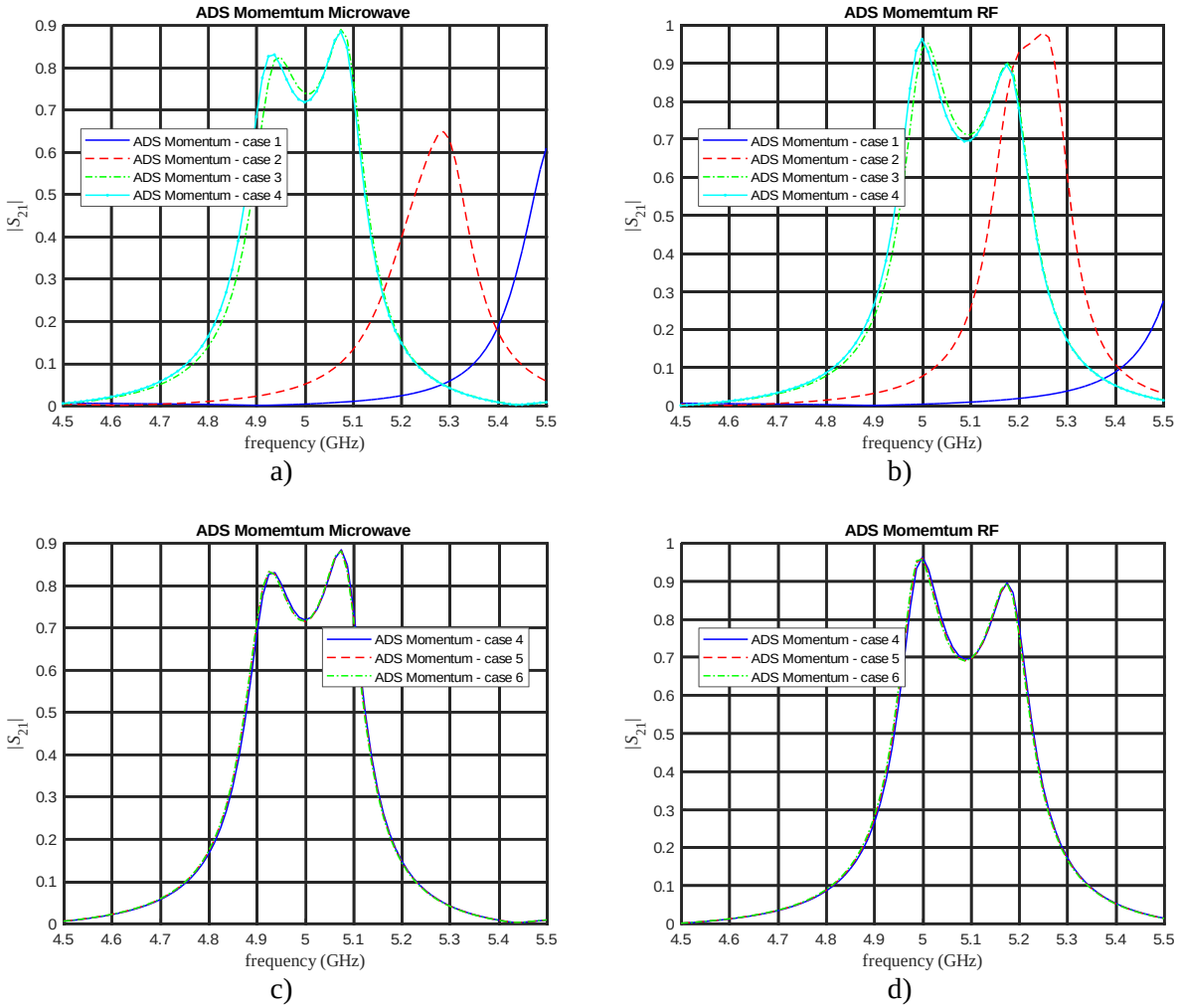

Fig. 1.38 Band-pass filter response at $\boldsymbol{x}_f^*$: a) Cases 1 to 4 ADS Momentum Microwave, b) Cases 1 to 4 ADS Momentum RF, c) Cases 4 to 6 ADS Momentum Microwave, d) Cases 4 to 6 ADS Momentum RF.

range of validity of the MSOP component defined by (1-1)-(1-4), since it violates (1-4). Therefore, the simulation response for this structure using MSOP might not be as accurate as the one obtained for the low-pass filter.

As expected, the layout generated from these three schematic circuit models is the same. The layout obtained from the schematic models from Fig. 1.30, Fig. 1.31 or Fig. 1.32 is illustrated in Fig. 1.33.

The circuit simulation results of these models are shown in Fig. 1.34a. It is seen that the responses of the circuit models using MTEE, MCORN and MSOP are different. Fig. 1.34a also shows the full-wave EM response of the layout (see Fig. 1.33) generated from any of these three models. It is seen from Fig. 1.34a that the circuit model response that uses the MSOP component

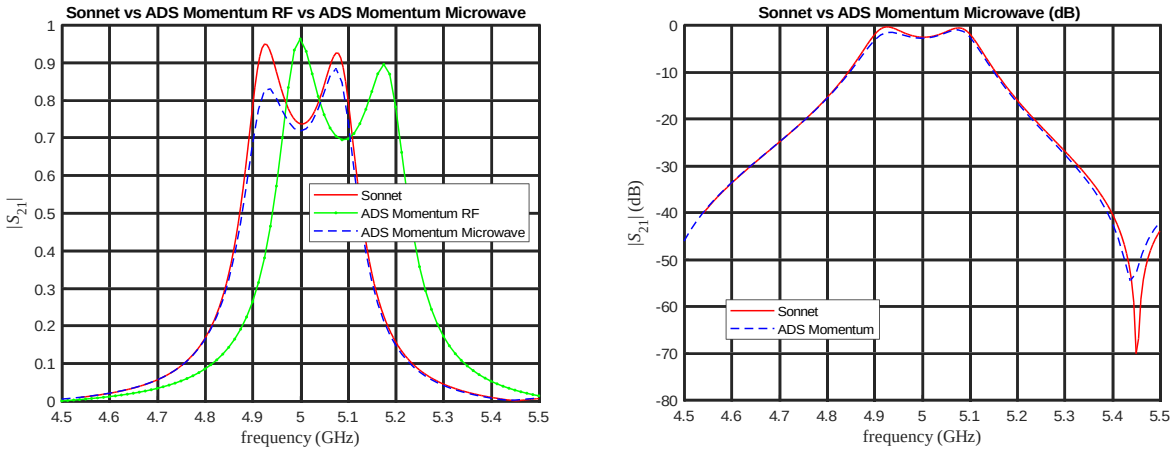

Fig. 1.39 Band-pass filter response at $\boldsymbol{x}_f^*$ with Sonnet and ADS Momentum using the best configuration (Case 4): a) $|S_{21}|$, b) $|S_{21}|$ (dB).

is slightly closer to the EM response almost in the whole frequency range, than those obtained from the circuit models using MTEE or MCORN components. These results are consistent with those obtained for the complete low-pass filter (see Fig. 1.29c).

As a very last test, we implemented the same simple structure shown in Fig. 1.33 but modifying the vertical length, from 7.245 mm (L_1+S_1) to 12.125 mm ($2L_1$+S_1). We can see in Fig. 1.34b that the responses of the circuit models using MTEE, MCORN and MSOP are again different, as expected. Of course, the EM response obtained from the layout generated from each circuit model is the same and is also included in Fig. 1.34b. It is seen from Fig. 1.34b that, in this case, the circuit response of the model using the MSOP component is closer to the EM response

TABLE 1.6. CONFIGURATION OF ADS MOMENTUM FOR THE BAND-PASS MICROSTRIP FILTER

Case	Mesh density (cells/λ)	Edge mesh	Transmission line mesh	Thin layer overlap extraction	Port feed type	Simulation time (hr:min:sec)	
						Momentum Microwave	Momentum RF
1	1	not used	not used	Normal	Auto	0:00:03	0:00:02
2	5	not used	not used	Normal	Auto	0:00:04	0:00:02
3	20	Auto	not used	Aggressive	TML	0:00:12	0:00:02
4	20	Auto	10	Aggressive	TML	0:01:57	0:00:35
5	20	Auto	20	Aggressive	TML	0:07:45	0:01:48
6	40	Auto	40	Aggressive	TML	1:05:25	0:59:24

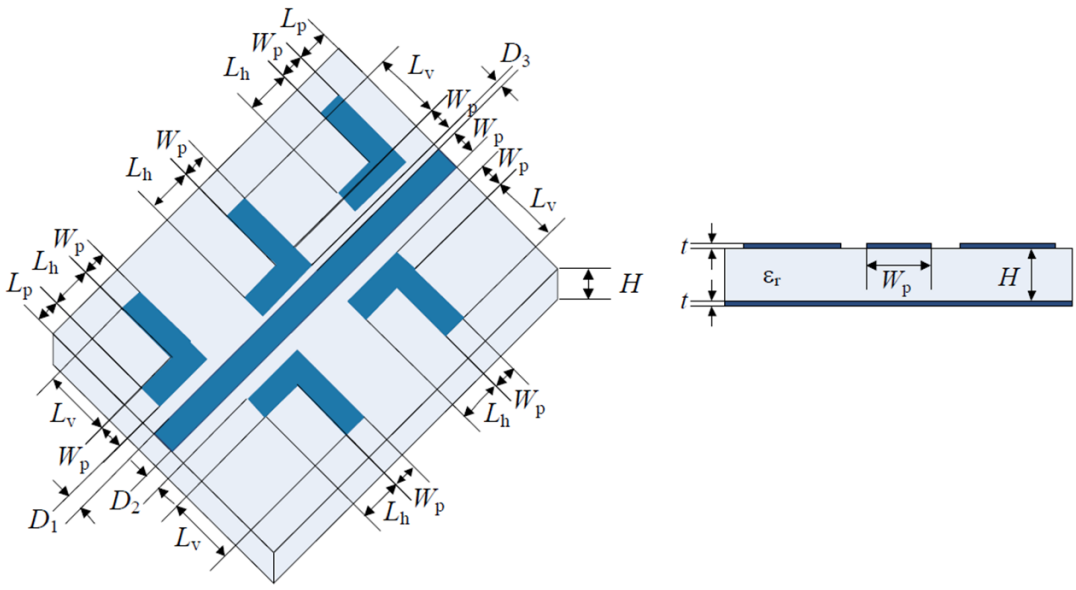

Fig. 1.40 Microstrip band-stop filter [Hong-01]. Figure taken from [Chávez-Hurtado-13].

only at frequencies higher than 12 GHz. For lower frequencies, the model using MCORN yields slightly more accurate results.

1.5. Microstrip Band-Pass Filter

The next filter is the microstrip band-pass filter [Hennings-06] shown in Fig. 1.35. This band-pass filter has been studied in [Brito-Brito-12], [Cervantes-Gónzalez-12], [Chávez-Hurtado-16], [Gutiérrez-Ayala-10], [Koziel-06] and [Loera-Díaz-18].

1.5.1 Band-Pass Filter Description

This filter has five design parameters $\boldsymbol{x} = [L_1 \;\; L_2 \;\; L_3 \;\; L_4 \;\; S_g]^T$ and five pre-assigned parameters $\boldsymbol{z} = [H \;\; \varepsilon_r \;\; \tan(\delta) \;\; W_p \;\; L_p]$, with a substrate (lossless Alumina) thickness H = 0.66 mm, relative dielectric permittivity ε_r = 9, and loss tangent $\tan(\delta)$ = 0.

Metal in this second example is considered as a perfect conductor. Moreover, it is considered as infinitesimally thin metal, t = 0, with W_p = 0.7 mm and L_p = 0.625 mm. The optimal values for the fine model (full-wave EM model) of this filter are $\boldsymbol{x}_f^*$ = [6.62 5.10 6.26 5.35 0.150]^T (mm) [Loera-Díaz-25c]. The simulation responses of this band-pass filter at $\boldsymbol{x}_f^*$ in Sonnet

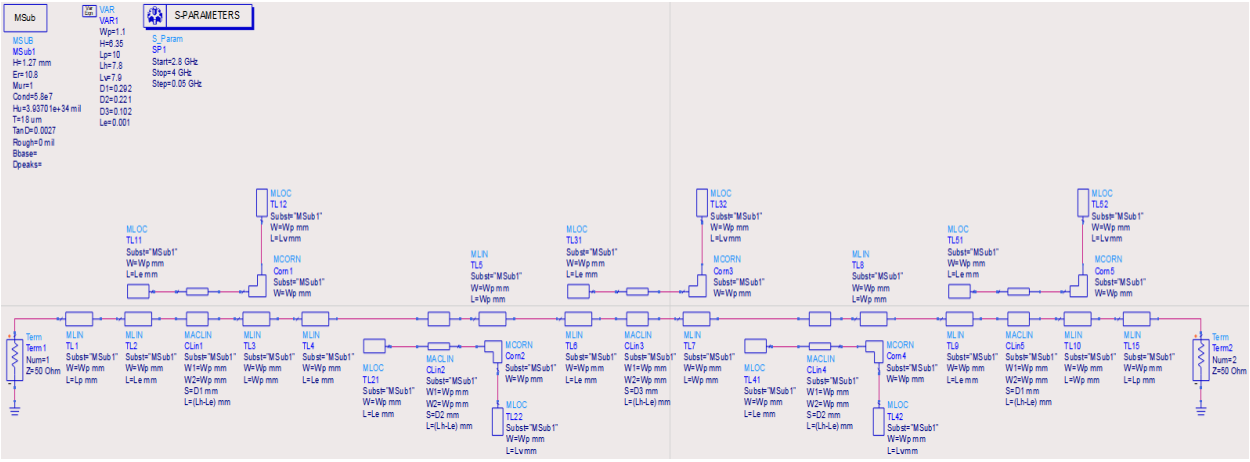

Fig. 1.41 Circuit model in ADS for the microstrip band-stop filter.

are shown in Section 1.5.3.

1.5.2 Band-Pass Filter: ADS Momentum Configuration

This filter has been configured in the same manner as described in Section 1.4.2. In a similar way, Table 1.6 shows the configurations cases arbitrarily chosen in Momentum Microwave and Momentum RF. For this example, only six configuration cases are considered instead of the eight cases from the previous example, as shown in Table 1.6 (the omitted cases resulted irrelevant).

This example uses 81 frequency points per frequency sweep.

1.5.3 Band-Pass Filter: ADS Momentum Simulation Responses and Validation

Fig. 1.36 shows the circuit model in ADS of the band-pass filter, which is used to generate the layout for the full-wave EM simulations. Fig. 1.37 shows the filter mesh for the layout for Cases 1 to 6.

The band-pass filter responses at $\boldsymbol{x}_{\mathrm{f}}^{*}$ for Cases 1 to 4 are shown in Fig. 1.38a and Fig. 1.38b. Again, Case 1 is the less accurate case because it only considers one cell per wavelength. Fig. 1.38c and Fig. 1.38d show the simulation responses for Cases 4, 5 and 6. In this example, Case 6 is the most accurate case of the six cases. It is seen from Fig. 1.38 and Table 1.6 that Case 4 has

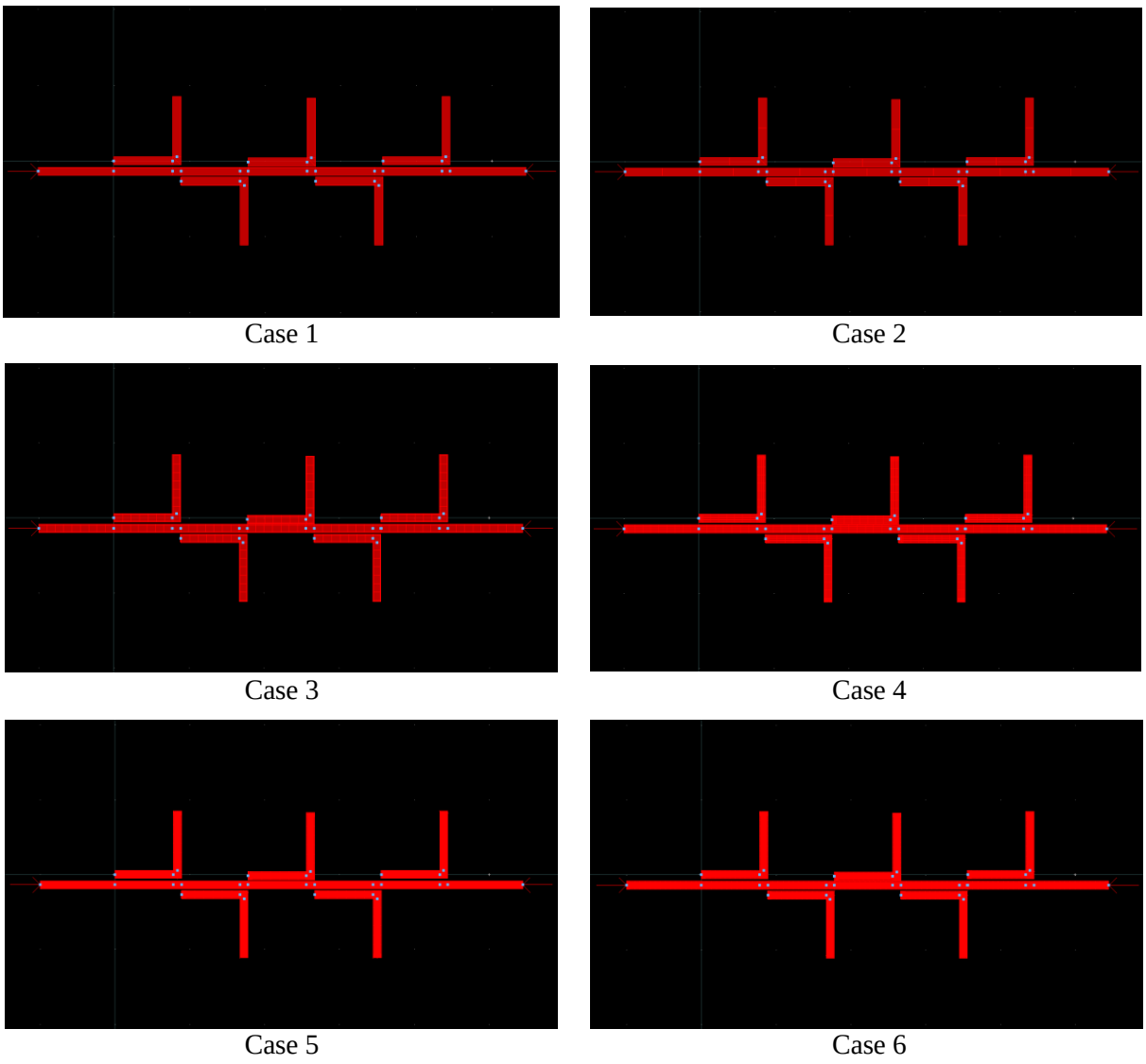

Fig. 1.42 Band-stop filter mesh for Cases 1 to 6 (see Table 1.7).

the best behavior for these configuration cases, since Cases 4 and 6 yield practically the same simulation response, but Case 4 has faster simulation time than Case 6, as shown in Table 1.6.

Fig. 1.39a shows that, once again, ADS Momentum Microwave yields a more accurate response than ADS Momentum RF, as expected. Finally, Fig. 1.39b shows a satisfactory matching between the EM simulation responses from ADS Momentum Microwave (Case 4) and Sonnet.

1.6. Microstrip Band-Stop Filter

The last filter is a fifth order Chebyshev band-stop microstrip filter with L-shaped

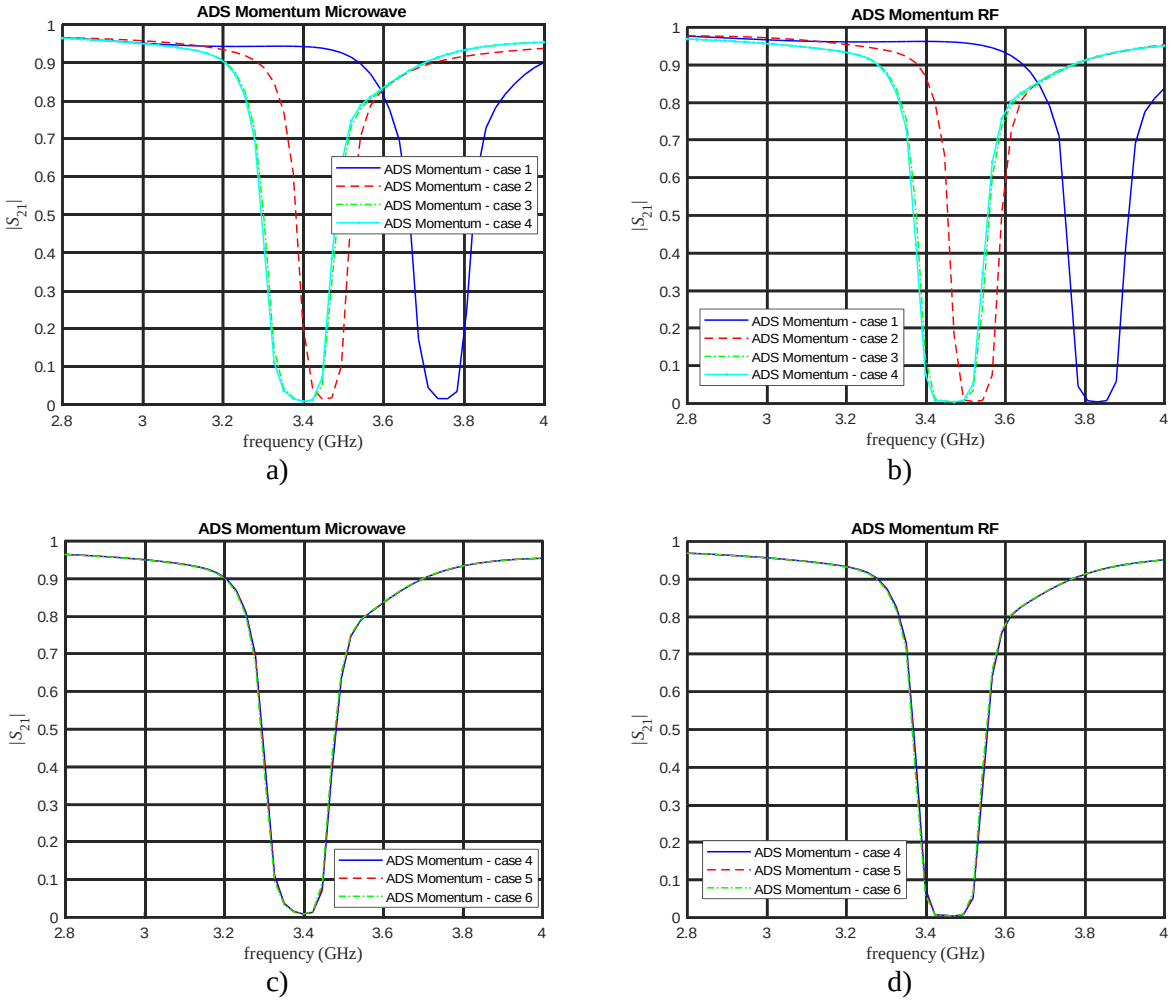

Fig. 1.43 Band-pass filter response at $\boldsymbol{x}_f^*$: a) Cases 1 to 4 ADS Momentum Microwave, b) Cases 1 to 4 ADS Momentum RF, c) Cases 4 to 6 ADS Momentum Microwave, d) Cases 4 to 6 ADS Momentum RF.

resonators [Hong-01], as shown in Fig. 1.40. This band-stop filter has been studied in [Chávez-Hurtado-13].

1.6.1 Band-Stop Filter Description

This Chebyshev filter has five design parameters $\boldsymbol{x} = [L_h \;\; L_v \;\; D_1 \;\; D_2 \;\; D_3]^T$ and six pre-assigned parameters $\boldsymbol{z} = [H \;\; \varepsilon_r \;\; W_p \;\; \tan(\delta) \;\; \sigma \;\; t]$.

In this case, the filter substrate uses a Rogers 6010 laminate with thickness H = 1.27 mm, relative dielectric permittivity ε_r = 10.8, and loss tangent $\tan(\delta)$ = 0.0027. In this last example,

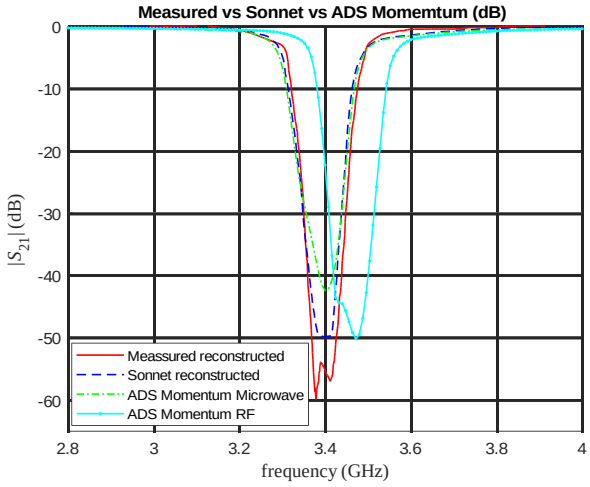

Fig. 1.44 Band-stop filter response at $\boldsymbol{x}_f^*$ with measured data [Chávez-Hurtado-13], Sonnet information [Chávez-Hurtado-13], ADS Momentum Microwave and RF using the best configuration (Case 4).

metal is considered as copper with electrical conductivity $\sigma = 5.8\times10^7$ S/m and thickness $t = 18$ μm. The 50-ohm lines have a width $W_p = 1.1$ mm. All the resonators have the same lengths L_v and L_h.

According to [Chávez-Hurtado-13] the optimal values for the fine model (full-wave EM model) of this filter are $\boldsymbol{x}_f^* = [7.8 \;\; 7.9 \;\; 0.292 \;\; 0.221 \;\; 0.102]^T$ (mm).

1.6.2 Band-Stop Filter: ADS Momentum Configuration

This last example considers 51 frequency points per frequency sweep. Table 1.7 shows the configuration of ADS Momentum for the microstrip band-stop filter and the simulation time for the same six test cases considered in Section 1.5.2.

Similarly to the previous examples, a circuit model in ADS is created as shown in Fig. 1.41. Once again, this model is used to generate the layout that will be used for the full-wave EM simulations in ADS Momentum. The layout mesh for Cases 1 to 6 are illustrated in Fig. 1.42.

1.6.3 Band-Stop Filter: ADS Momentum Simulation Responses

Fig. 1.43a and Fig. 1.43b show the full-wave EM simulation responses for Cases 1 to 4 in ADS Momentum Microwave and ADS Momentum RF, respectively. Again, Case 1 is the less

TABLE 1.7. CONFIGURATION OF ADS MOMENTUM FOR THE BAND-STOP MICROSTRIP FILTER

Case	Mesh density (cells/λ)	Edge mesh	Transmission line mesh	Thin layer overlap extraction	Port feed type	Simulation time (hr:min:sec)	
						Momentum Microwave	Momentum RF
1	1	not used	not used	Normal	Auto	0:00:02	0:00:01
2	5	not used	not used	Normal	Auto	0:00:02	0:00:02
3	20	Auto	not used	Aggressive	TML	0:00:14	0:00:06
4	20	Auto	10	Aggressive	TML	0:02:14	0:00:46
5	20	Auto	20	Aggressive	TML	0:14:18	0:05:38
6	40	Auto	40	Aggressive	TML	3:14:21	1:22:04

accurate one because it only has one cell per wavelength while Case 6 is the most accurate one. For this example, Case 4 has the best performance of these six cases. This can be confirmed from Fig. 1.43c and Fig. 1.43d that show how Cases 4 and 6 have practically the same response. However, the simulation time for Case 4 is much faster than the simulation time required for Case 6, as seen in Table 1.7.

Finally, Fig. 1.44 illustrates the simulation responses of Case 4 in dB obtained with ADS Momentum Microwave and ADS Momentum RF against the reconstructed responses obtained from [Chávez-Hurtado-13]. This figure shows that the matching of the simulation responses obtained with Momentum Microwave and Sonnet are satisfactory.

1.7. Conclusion

This chapter presented a simulation procedure of how to configure ADS Momentum to obtain reliable 2-D EM simulations for filters in microstrip technology. We analyzed four different microstrip filters and obtained similar results in terms of the most suitable configuration. For all the cases studied in this chapter, Momentum Microwave shows higher accuracy than Momentum RF, as expected. An adequate configuration of the feed type parameter produces slightly better results; the best performance was obtained with the "TML" feed port. In addition to this, if a coarse layout mesh is configured for the EM model, the obtained responses are not accurate. Using "edge mesh" and "transmission line mesh" in the configuration of ADS Momentum also increase

accuracy in the filter responses. On the other hand, if a too fine mesh is configured, the responses are more accurate but the simulation time becomes too long. Regarding the mesh resolution, the best configuration is obtained when the simulation responses reach convergence, that is, when they practically do not change regardless of how fine the layout mesh is. In general, the best configuration is obtained when a good accuracy and a fast simulation time are simultaneously obtained.

This chapter also presented a comparison of simulation responses for the low-pass microstrip filter with different circuit models and compares them with the corresponding full-wave EM model response. The physical layout obtained from these circuit models is exactly the same, and hence, the full-wave EM simulation responses of the physical layouts obtained from these circuit models are the same. It was confirmed that the circuit simulation responses of apparently equivalent circuit models can be different, depending on the ADS components used to represent the physical structure. Some circuit models can be more accurate than others. It was found that the circuit model that uses an MSOP component is more accurate than that one using MTEE for the low-pass filter. However, we found that for other simpler microstrip structures, the accuracy of the MSOP component is not necessarily always better than the MTEE or MCORN components, indicating that attention must be given to the validity range of these ADS components.

2. An Objective Function Formulation for Circuit Parameter Extraction Based on the Kullback-Leibler Distance

Numerical circuit parameter extraction is widely used for modeling many kinds of high-frequency structures. In particular, parameter extraction can be used to find the optimal parameter values of an equivalent circuit model to match as close as possible a given target response. This chapter corresponds to a slightly modified version of our work in [Loera-Díaz-20a]. This chapter presents a novel objective function formulation for parameter extraction based on the Kullback-Leibler distance [Kullback-51]. A rigorous graphical and numerical comparison of the proposed new formulation against classical *l*-th norm formulations is included. One- and two-dimensional synthetic examples are used to illustrate the advantages of the proposed Kullback-Leibler distance formulation. Our results indicate that the proposed new formulation yields similar or better-behaved parameter extraction objective functions than those obtained from *l*-th norm formulations.

2.1. Introduction

The EM response of a high-frequency structure can be locally approximated by using numerical parameter extraction (PE) if there is available an initial parameterized model that approximates the structure performance. PE formulations can be used to minimize the error between the approximating model response and the target EM response. To measure the error between these two responses, formulations with *l*-th norms are widely used. Parameter extraction is also the most critical process in several space mapping (SM) optimization algorithms [Bandler-04], [Koziel-08], [Rayas-Sánchez-16] and [Søndergaard-03]; using better formulations for parameter extraction can positively impact on the convergence of SM algorithms that require performing PE at each iteration.

To the best of our knowledge, our work in [Loera-Díaz-20a] presented for the first time a formulation of the objective function for parameter extraction exploiting concepts related to Shannon entropy theory, more specifically, by using the Kullback-Leibler (K-L) distance

[Kullback-51]-[Veldhuis-03] to represent the error function to be minimized during numerical PE. A rigorous graphical and numerical comparison between the proposed K-L formulation and classical Manhattan, Euclidean, and Chebyshev formulations is presented, exploiting one- and two-dimensional synthetic examples where it is feasible to plot the PE objective function versus the model parameters [Loera-Díaz-19a], [Loera-Díaz-19b]. The results obtained considering these synthetic cases indicate that the proposed formulation based on the Kullback-Leibler distance yields similar or better behaved PE objective functions than those obtained from *l*-th norm formulations [Loera-Díaz-20a], which might be useful for more robust SM algorithms.

2.2. Circuit PE

Numerical circuit parameter extraction (PE) can be formulated as the following optimization problem:

$$\boldsymbol{x}^{\mathrm{PE}} = \arg\min_{\boldsymbol{x}} U_{\mathrm{PE}}(\boldsymbol{R}(\boldsymbol{x}), \boldsymbol{R}^{\mathrm{t}}) \tag{2-1}$$

where vector $\boldsymbol{x} \in \Re^n$ contains the model parameters, vector function $\boldsymbol{R}(\boldsymbol{x}): \Re^n \rightarrow \Re^r$ generates the model responses, and vector $\boldsymbol{R}^{\mathrm{t}} \in \Re^r$ contains the target or desired response. The scalar parameter extraction objective function, $U_{\mathrm{PE}}: \Re^n \rightarrow \Re^1$, measures the difference between the model response $\boldsymbol{R}(\boldsymbol{x})$ and the target response $\boldsymbol{R}^{\mathrm{t}}$. When performing PE, we aim at finding the optimal model parameters $\boldsymbol{x}^{\mathrm{PE}} \in \Re^n$ that make the model response $\boldsymbol{R}(\boldsymbol{x})$ as close as possible to the target response $\boldsymbol{R}^{\mathrm{t}}$. Ideally, $\boldsymbol{R}(\boldsymbol{x}^{\mathrm{PE}}) = \boldsymbol{R}^{\mathrm{t}}$.

As mentioned before, PE is also used as an important sub-process in several SM optimization algorithms [Bandler-04]. SM techniques employ at least two models for the device to be optimized: a highly accurate but computationally expensive model, named as fine model, and a fast but insufficiently accurate representation, named as coarse model. In the context of SM, the target response $\boldsymbol{R}^{\mathrm{t}}$ is usually obtained from the fine model response $\boldsymbol{R}_{\mathrm{f}}$ at some fine model design parameters $\boldsymbol{x}_{\mathrm{f}}$, *i.e.*, $\boldsymbol{R}^{\mathrm{t}} = \boldsymbol{R}_{\mathrm{f}}(\boldsymbol{x}_{\mathrm{f}})$, and PE is used to find the coarse model parameters $\boldsymbol{x}_{\mathrm{c}}$ that makes the coarse model response $\boldsymbol{R}_{\mathrm{c}}$ as close as possible to the fine model response. Ideally, $\boldsymbol{R}_{\mathrm{c}}(\boldsymbol{x}_{\mathrm{c}}^{\mathrm{PE}}) = \boldsymbol{R}_{\mathrm{f}}(\boldsymbol{x}_{\mathrm{f}})$, where $\boldsymbol{x}_{\mathrm{c}}^{\mathrm{PE}}$ is the solution of the corresponding PE optimization sub-problem, which is normally inexpensive since $\boldsymbol{R}_{\mathrm{f}}(\boldsymbol{x}_{\mathrm{f}})$ remains fixed during PE. However, PE can be very problematic for SM if U_{PE} has multiple local minima [Rayas-Sánchez-16], [Bandler-99].

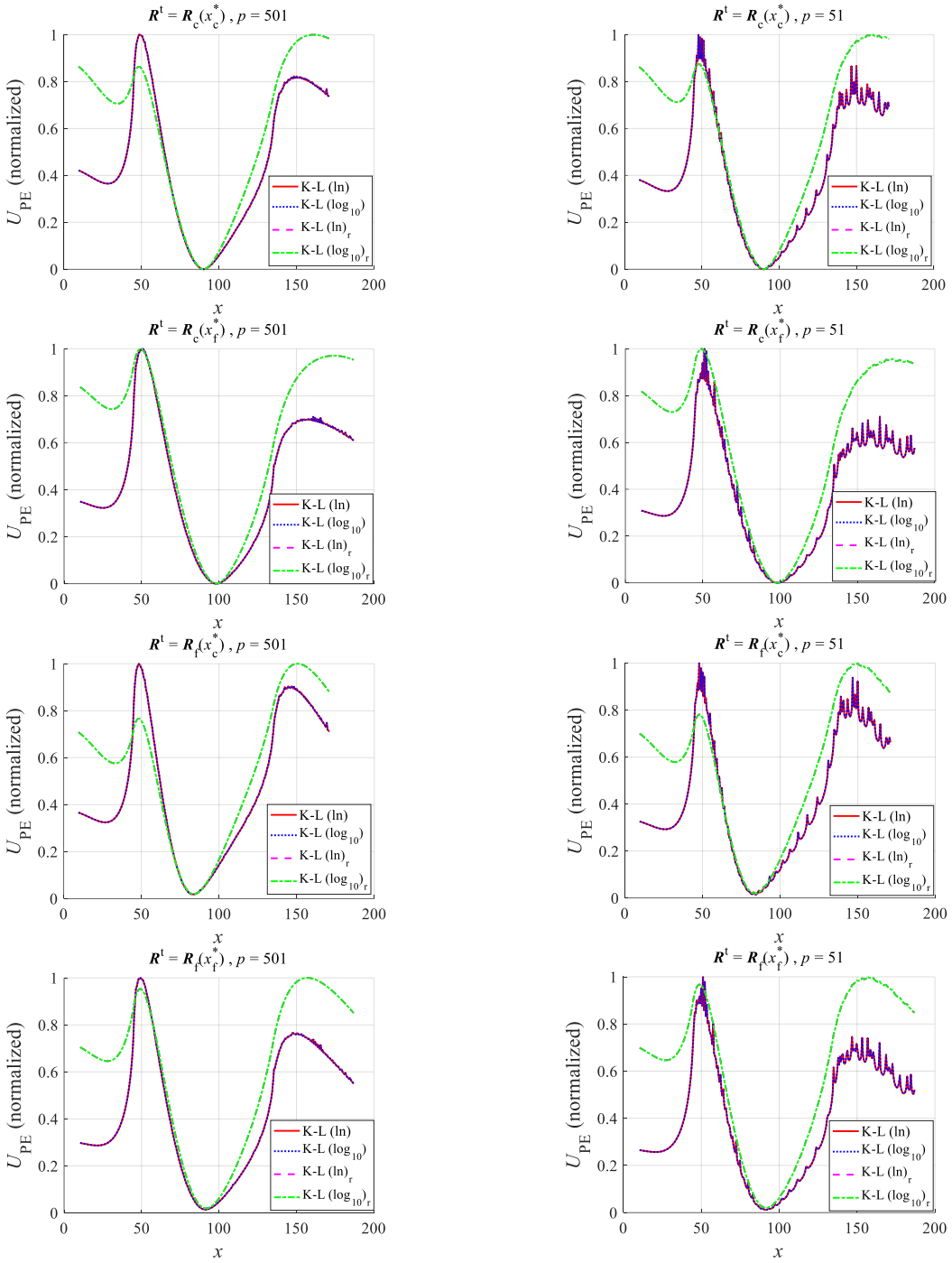

Fig. 2.1 Kullback-Leibler parameter extraction (PE) objective functions for a one-dimensional problem: comparing formulation with natural logarithm *vs.* base-10 logarithm, and comparing formulation in "regular order" (as in [Loera-Díaz-19a]), *vs.* "reverse order" (as in (2-7) and (2-8)), varying the number of frequency points p for frequencies f in the range 0.01 GHz $\leq f \leq$ 2 GHz.

Several formulations for the PE objective function U_{PE} can be considered. In Section 2.3, the PE objective function U_{PE} using generalized l-th norms is revisited. In Section 2.4, the

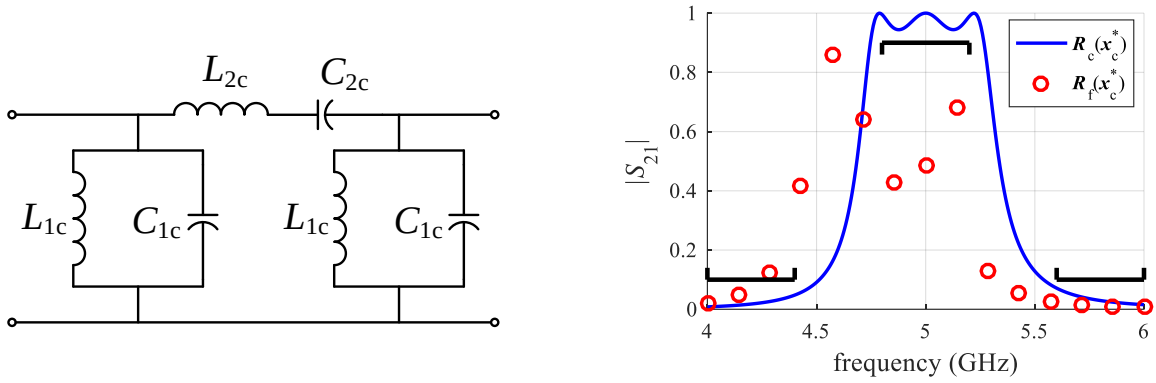

Fig. 2.2 Coarse model of a sixth-order band-pass filter, its optimal response (continued blue trace) and a fine model target response sampled at p = 15 frequency points from 4 to 6 GHz (circled red trace).

proposed new formulation based on the Kullback-Leibler distance is used to formulate U_{PE}.

2.3. Classical Norms Formulations for PE

The PE objective function can be formulated as an l-th norm,

$$U_{\mathrm{PE}}(\boldsymbol{x}) = \|\boldsymbol{e}(\boldsymbol{x})\|_l \tag{2-2}$$

where $\boldsymbol{e}(\boldsymbol{x}) \in \Re^r$ is the error of the model response with respect to the target response, $\boldsymbol{e}(\boldsymbol{x}) = \boldsymbol{R}(\boldsymbol{x}) - \boldsymbol{R}^{\mathrm{t}}$. The most widely used norms are as follows.

2.3.1 Manhattan

The l_1 norm formulation, also known as Manhattan, uses

$$U_{\mathrm{PE}}(\boldsymbol{R}(\boldsymbol{x}), \boldsymbol{R}^{\mathrm{t}}) = \sum_{i=1}^{r} |e_i(\boldsymbol{x})| \tag{2-3}$$

and it emphasizes the average absolute error.

2.3.2 Euclidean

The l_2 norm formulation, also known as Euclidean, uses

$$U_{\mathrm{PE}}(\boldsymbol{R}(\boldsymbol{x}), \boldsymbol{R}^{\mathrm{t}}) = \left(\sum_{i=1}^{r} e_i^2(\boldsymbol{x})\right)^{\frac{1}{2}} \tag{2-4}$$

and it emphasizes the mean square error.

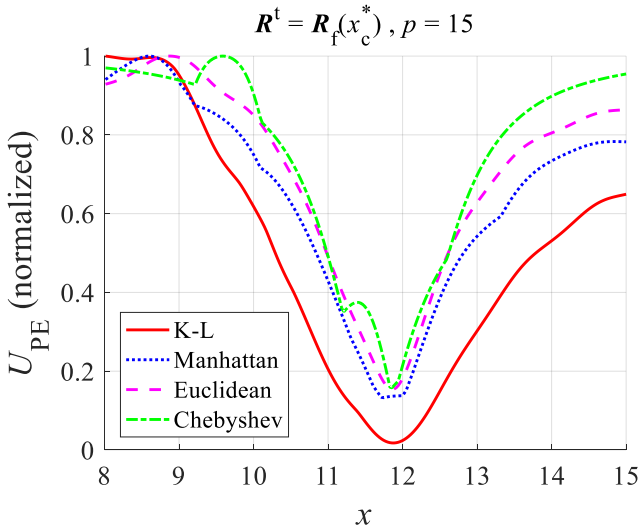

Fig. 2.3 PE objective functions for sixth-order band-pass filter in Fig. 2.2 varying $x_c = C_{1c}$ from 8 to 15 pF.

2.3.3 Chebyshev

The infinite norm or Chebyshev formulation uses

$$U_{PE}(\boldsymbol{R}(\boldsymbol{x}), \boldsymbol{R}^{t}) = \max_{i}\{\cdots |e_i(\boldsymbol{x})| \cdots\} \tag{2-5}$$

and it emphasizes the maximum absolute error.

2.4. Kullback-Leibler (K-L) Formulation for PE

According to Shannon information theory [McEliece-01], the degree of difference between the states of two systems *A* and *B* can be represented by relative entropy [Zhao-05]. This difference can be measured using the "Kullback-Leibler measure" [Cui-02], [Veldhuis-03], [Lee-11], also known in other publications as "K-L divergence" [Hershey-07], [Chen-08], [Erven-14], [Bouhlel-19], or "K-L distance" [Kullback-87], [Do-02], [Vergara-09], [Nafornita-12], [Zhou-20], [Han-22]. According to [Zhao-05] and [Matsuoka-91], the Kullback-Leibler distance [Zhu-02] can be defined as

$$C = \sum_{i=1}^{N}\left\{A_i \ln\frac{A_i}{B_i} + (1-A_i)\ln\frac{1-A_i}{1-B_i}\right\} \tag{2-6}$$

where *C* is the relative entropy between the systems *A* and *B*. The *i*-th states of these systems are

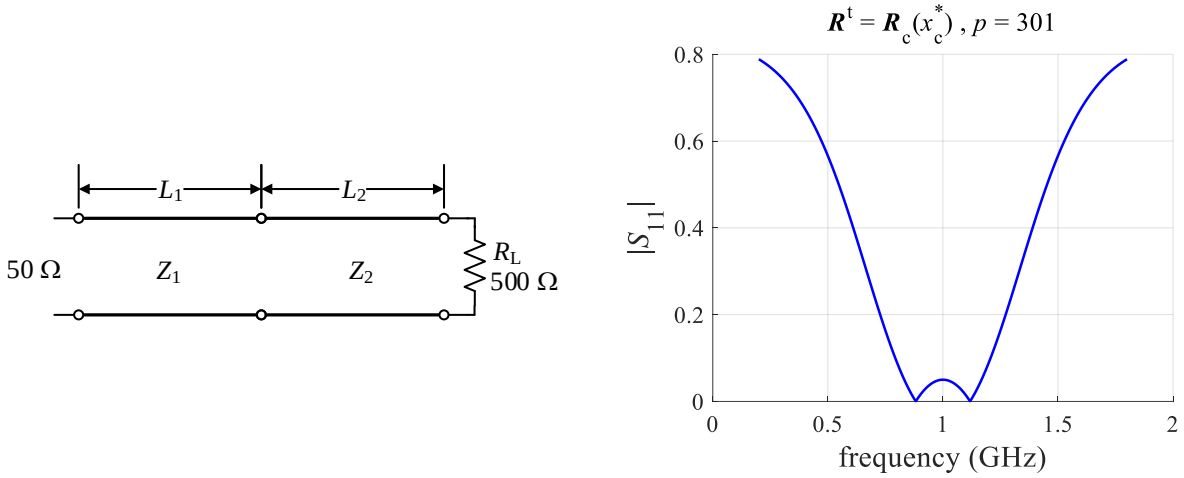

Fig. 2.4 Ideal 10:1 two-section impedance transformer used as a coarse model and its optimal response taken as target, sampled at p = 301 frequency points from 0.2 to 1.8 GHz.

represented by A_i and B_i (i = 1, 2, … , N) [Zhao-05]. As mentioned in [Matsuoka-91], it is assumed that A lies in [0, 1] and that $0 \times ln\,(0) = 0$. Moreover, each pair of A_i and $1–A_i$, and each pair of B_i and $1–B_i$ are treated as probabilities in [Matsuoka-91]. Notice that (2-6) becomes zero only when A_i is equal to B_i, for every i; otherwise this expression becomes positive [Matsuoka-91]. This formulation provides a quantitative measure of the difference between two probability distributions [Vergara-09]. Extending (2-6) to the PE problem, the following alternative objective function is proposed [Loera-Díaz-20a]:

$$U_{\mathrm{PE}}(\boldsymbol{R}(\boldsymbol{x}), \boldsymbol{R}^{\mathrm{t}}) = \sum_{i=1}^{r} \left\{ R_i \ln \left| \frac{R_i}{R_i^{\mathrm{t}}} \right| + (1 - R_i) \ln \left| \frac{1-R_i}{1-R_i^{\mathrm{t}}} \right| \right\} \tag{2-7}$$

where R_i is the i-th model response at model parameters $\boldsymbol{x}$, and R_i^{t} is the i-th target response. By analogy to the expression (2-6), we assume that R_i lies in [0, 1]. This may be due to the nature of the model response itself, *e.g.*, S-parameters (such as $|S_{11}|$ and $|S_{21}|$ for passive circuits) with values between 0 and 1, or because the model response has been normalized. The aim of (2-7), in the context of PE, is to provide a quantitative measure of the difference between the model response and the target response.

A potential limitation of the proposed K-L formulation emerges from (2-7); it is not feasible when the response values have opposite signs. Moreover, R_i^{t} must satisfy $0 < R_i^{\mathrm{t}} < 1$ to avoid undefined logarithms.

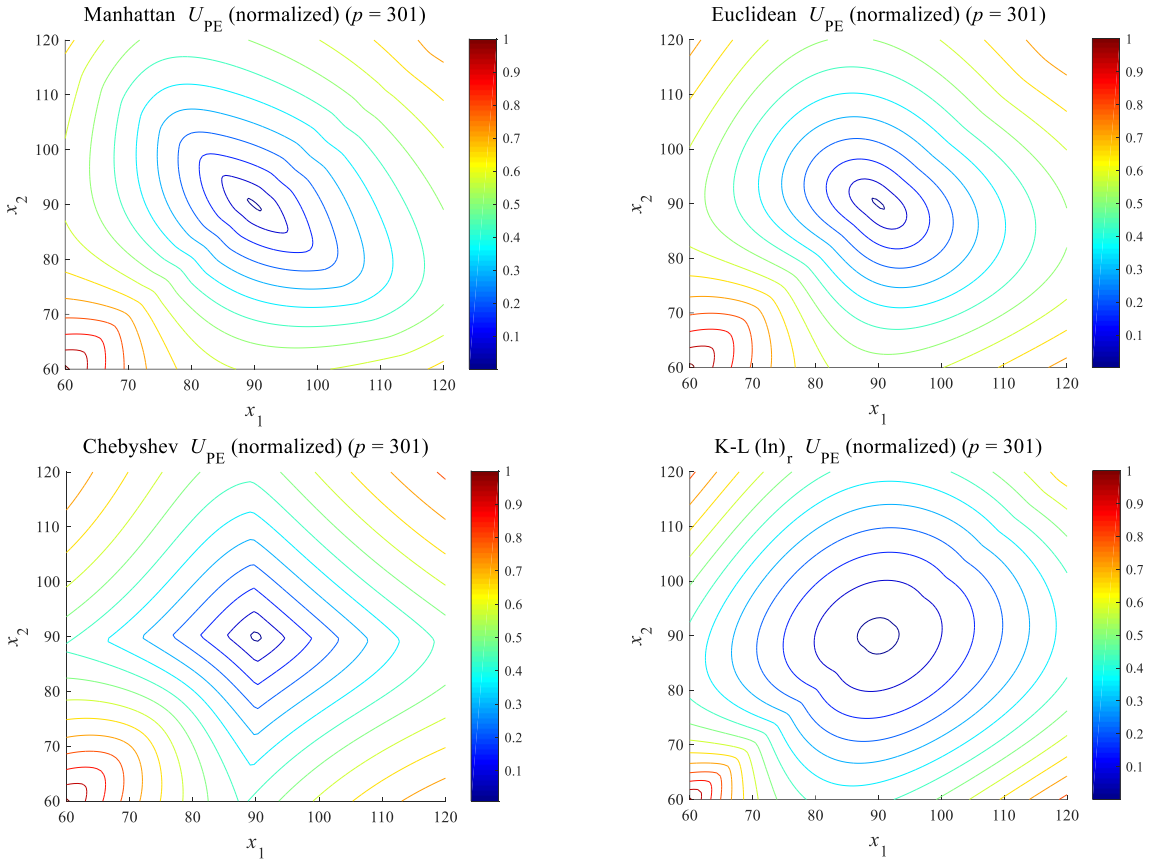

Fig. 2.5 Normalized PE objective functions for example in Fig. 2.4 varying L_1 and L_2 from 60º to 120º.

2.4.1 K-L Formulation with Base-10 and Natural Logarithms

We have experimentally confirmed, with several PE circuit examples, that the Kullback-Leibler distance PE objective function calculated with base-10 logarithm, as follows,

$$U_{\mathrm{PE}}(\boldsymbol{R}(\boldsymbol{x}), \boldsymbol{R}^{\mathrm{t}}) = \sum_{i=1}^{r} \left\{ R_i \log \left| \frac{R_i}{R_i^{\mathrm{t}}} \right| + (1 - R_i) \log \left| \frac{1-R_i}{1-R_i^{\mathrm{t}}} \right| \right\} \tag{2-8}$$

and calculated with natural logarithm (2-7) yield practically the same numerical results (the corresponding comparison is omitted for the sake of brevity). In consequence, only formulation (2-7) is used in the following section for the comparison with *l*-th norm formulations.

It should be noticed that formulations (2-7) and (2-8) are using the model response R_i and the target response R_i^{t} in reverse order with respect to that one used in [Loera-Díaz-19a]. We have also experimentally confirmed, with several PE circuit examples, that the Kullback-Leibler

TABLE 2.1. ONE-DIMENTIONAL EXAMPLE SOLVED BY NUMERICAL PE USING THE NELDER-MEAD METHOD

$\boldsymbol{x}^{(0)}$	Obj. Func.	i	$\boldsymbol{x}^{\mathrm{PE}}$	$\varepsilon_{\mathrm{avg}}$	$\varepsilon_{\mathrm{max}}$	$\varepsilon_{\mathrm{nmse}}$
8.5	Manhattan	33	11.7251	0.0504	0.2447	0.1937
	Euclidean	28	6.4742	0.2873	0.9800	0.9105
	Chebyshev	31	9.2177	0.3342	0.9187	1.0506
	K-L	28	11.8747	0.0523	0.1599	0.1663
10.1624	Manhattan	30	11.7251	0.0504	0.2447	0.1937
	Euclidean	26	11.8623	0.0522	0.1573	0.1660
	Chebyshev	30	11.8365	0.0520	0.1518	0.1671
	K-L	26	11.8747	0.0523	0.1599	0.1663
14.5	Manhattan	32	11.7251	0.0504	0.2447	0.1937
	Euclidean	27	11.8623	0.0522	0.1573	0.1660
	Chebyshev	31	11.8365	0.0520	0.1518	0.1671
	K-L	27	11.8747	0.0523	0.1599	0.1663

distance in "regular order", as used in [Loera-Díaz-19a], is severely affected when the responses are calculated using a small number of frequency (or independent-variable) points. The corresponding exhaustive comparison is also omitted for the sake of brevity. However, in Fig. 2.1 we illustrate that problem for a one-dimensional example in Matlab[5]. In that figure, labels "K-L ($\log_{10}$)" and "K-L (ln)" denote the Kullback-Leibler PE objective function formulation in "regular order" as used in [Loera-Díaz-19a], using base-10 logarithm and natural logarithm, respectively, while those labels using sub-index r denote the formulations in reverse order, as in (2-7) and (2-8). It is seen from Fig. 2.1 that formulations in "reverse order" yield soft PE objective functions, while those in "regular or direct order" present sharp variations and multiple local minima, especially when a small number of frequency (or independent-variable) points is used. It is also confirmed in Fig. 2.1 that the Kullback-Leibler PE objective function calculated with base-10 logarithm and with natural logarithm yield the same results.

Based on all the above, only the the Kullback-Leibler distance with natural logarithm in "reverse order", as in (2-7), is used through this thesis.

[5] MATLAB, Version R2022b, The MathWorks, Inc., 1 Apple Hill Drive, Natick MA 01760-2098, 2022.

TABLE 2.2. TWO-DIMENTIONAL EXAMPLE SOLVED BY NUMERICAL PE USING THE NELDER-MEAD METHOD

$\boldsymbol{x}^{(0)}$	Objective Function	i	$\boldsymbol{x}^{\mathrm{PE}}$
$[70 \quad 80]^{\mathrm{T}}$	Manhattan	86	$[90.0000 \quad 90.0000]^{\mathrm{T}}$
	Euclidean	80	$[90.0000 \quad 90.0000]^{\mathrm{T}}$
	Chebyshev	80	$[90.0000 \quad 90.0000]^{\mathrm{T}}$
	K-L	75	$[90.0000 \quad 90.0000]^{\mathrm{T}}$
$[110 \quad 80]^{\mathrm{T}}$	Manhattan	90	$[90.0000 \quad 90.0000]^{\mathrm{T}}$
	Euclidean	77	$[90.0000 \quad 90.0000]^{\mathrm{T}}$
	Chebyshev	78	$[90.0000 \quad 90.0000]^{\mathrm{T}}$
	K-L	67	$[90.0000 \quad 90.0000]^{\mathrm{T}}$
$[90 \quad 115]^{\mathrm{T}}$	Manhattan	84	$[90.0000 \quad 90.0000]^{\mathrm{T}}$
	Euclidean	78	$[90.0000 \quad 90.0000]^{\mathrm{T}}$
	Chebyshev	76	$[90.0000 \quad 90.0000]^{\mathrm{T}}$
	K-L	72	$[90.0000 \quad 90.0000]^{\mathrm{T}}$

2.5. PE Comparison Using Classical Norms and Kullback-Leibler (K-L) Formulations

Graphical and numerical comparisons between K-L and *l*-th norm formulations are presented by synthetic examples. The following figures of merit to measure the corresponding matching errors are used: average absolute relative error ($\varepsilon_{\mathrm{avg}}$), normalized mean square error ($\varepsilon_{\mathrm{nmse}}$), and maximum absolute relative error ($\varepsilon_{\mathrm{max}}$), defined as

$$\varepsilon_{\mathrm{avg}} = \frac{\frac{1}{r}\|\boldsymbol{e}_{\mathrm{PE}}\|_1}{\|\boldsymbol{R}^{\mathrm{t}}\|_\infty} \tag{2-9}$$

$$\varepsilon_{\mathrm{max}} = \frac{\|\boldsymbol{e}_{\mathrm{PE}}\|_\infty}{\|\boldsymbol{R}^{\mathrm{t}}\|_\infty} \tag{2-10}$$

$$\varepsilon_{\mathrm{nmse}} = \frac{\|\boldsymbol{e}_{\mathrm{PE}}\|_2}{\|\boldsymbol{R}^{\mathrm{t}}\|_2} \tag{2-11}$$

where $\boldsymbol{e}_{\mathrm{PE}}$ is the error vector after PE, $\boldsymbol{e}_{\mathrm{PE}} = \boldsymbol{R}(\boldsymbol{x}^{\mathrm{PE}}) - \boldsymbol{R}^{\mathrm{t}}$.

TABLE 2.3. TWO-DIMENTIONAL EXAMPLE SOLVED BY NUMERICAL PE USING THE TRUST REGION INTERIOR-REFLECTIVE NEWTON METHOD

$\boldsymbol{x}^{(0)}$	Obj. Func.	i	$\boldsymbol{x}^{\mathrm{PE}}$	$\varepsilon_{\mathrm{avg}}$	$\varepsilon_{\max}$	$\varepsilon_{\mathrm{nmse}}$
$[70\ \ 80]^{\mathrm{T}}$	Manhattan	12	$[89.9999\ \ 90.0001]^{\mathrm{T}}$	0.0023×10^{-7}	0.1774×10^{-7}	0.0179×10^{-7}
	Euclidean	16	$[90.0001\ \ 89.9999]^{\mathrm{T}}$	0.0029×10^{-7}	0.2080×10^{-7}	0.0209×10^{-7}
	Chebyshev	14	$[90.0002\ \ 89.9998]^{\mathrm{T}}$	0.1460×10^{-7}	0.3664×10^{-7}	0.2829×10^{-7}
	K-L	13	$[90.0033\ \ 89.9968]^{\mathrm{T}}$	0.0878×10^{-5}	0.5782×10^{-5}	0.1777×10^{-5}
$[110\ \ 80]^{\mathrm{T}}$	Manhattan	16	$[90.0002\ \ 89.9998]^{\mathrm{T}}$	0.0041×10^{-7}	0.4442×10^{-7}	0.0429×10^{-7}
	Euclidean	12	$[89.9997\ \ 90.0003]^{\mathrm{T}}$	0.0051×10^{-7}	0.5286×10^{-7}	0.0519×10^{-7}
	Chebyshev	17	$[90.0038\ \ 89.9965]^{\mathrm{T}}$	0.2279×10^{-5}	0.5910×10^{-5}	0.4419×10^{-5}
	K-L	12	$[89.9972\ \ 90.0029]^{\mathrm{T}}$	0.0341×10^{-5}	0.4006×10^{-5}	0.0788×10^{-5}
$[90\ \ 115]^{\mathrm{T}}$	Manhattan	20	$[89.9999\ \ 90.0001]^{\mathrm{T}}$	0.0333×10^{-7}	0.1122×10^{-7}	0.0646×10^{-7}
	Euclidean	16	$[89.9999\ \ 90.0001]^{\mathrm{T}}$	0.1856×10^{-8}	0.9690×10^{-8}	0.3660×10^{-8}
	Chebyshev	3	$[83.0220\ \ 90.1578]^{\mathrm{T}}$	0.0567	0.1106	0.1047
	K-L	11	$[89.9977\ \ 90.0023]^{\mathrm{T}}$	0.0450×10^{-5}	0.2442×10^{-5}	0.0905×10^{-5}

2.5.1 One-Dimensional PE Example

The ideal sixth-order π bandpass symmetrical lumped filter shown in Fig. 2.2, is taken as a coarse model [Rayas-Sánchez-01]. It uses L_{1c} = 0.0997 nH, L_{2c} = 17.455 nH, and C2c = 0.058048 pF. To treat it as a one-dimensional problem, we use $x_c = C_{1c}$ as the only coarse model parameter.

The target response $\boldsymbol{R}^{t}$ is some fine model response $\boldsymbol{R}_f$ at the optimal coarse model design $x_c^* = 10.1624$ pF, using p = 15 frequency points from 4 to 6 GHz, as shown in Fig. 2.2. The PE objective function plots for the four corresponding formulations are in Fig. 2.3, where the K-L formulation exhibits the best-behaved objective function (unimodal, smoother and with larger dynamic range).

This is confirmed by the numerical results shown in Table 2.1, where i is the number of iterations.

2.5.2 Two-Dimensional PE Example

The ideal 10:1 two-section impedance transformer shown in Fig. 2.4 is used as a coarse model [Loera-Díaz-20a]. Reference impedance is Z0 = 50 Ω. Load impedance is R_L = 500 Ω. The transmission lines characteristic impedances are Z_1 = 1.8233Z_0 Ω, and Z_2 = 5.4845Z_0 Ω, using coefficients for a Chebyshev profile with a 10:1 transformation ratio and a 0.05 ripple. Model parameters are $\boldsymbol{x} = [L_1 \;\; L_2]^T$ (degrees). To test a case with an exact match, the target response is the optimal coarse model response from 0.2 to 1.8 GHz using p = 301 frequency points (see Fig. 2.4).

The contour plots for the four corresponding PE objective functions are shown in Fig. 2.5, where the K-L formulation shows the best-behaved surface, since the contour plots of the K-L objective function are softer and less non-linear in the overall parameter space (yielding a better defined minimum) than those defined by the contour plots of the objective function using classical norms.

This is re-confirmed by numerical results in Table 2.2 and Table 2.3, where *i* is again the number of iterations.

2.6. Conclusion

This chapter presented a formulation for parameter extraction (PE) in terms of the Kullback-Leibler (K-L) distance and a comparison with the classical *l*-th norm formulations. Our results indicate that the K-L distance formulation yields similar or better PE performance than the corresponding *l*-th norm formulations. This was confirmed by two findings: 1) smoother objective functions were observed; and 2) similar or smaller number of iterations were needed to obtain satisfactory response matching after numerical optimization.

3. Parameter Extraction Graphical and Numerical Study Using Classical Norms and the Kullback-Leibler Formulation

This chapter first shows a graphical study using Kullback-Leibler (K-L) distance formulations as objective function. A further comparison is made between formulations that consider natural logarithms against 10-base logarithms. This comparison is also made between formulations that consider "direct order" versus "reverse order" of the target and model responses in the Kullback-Leibler formulation. This graphical study is applied to some synthetic examples: a capacitively-loaded 2:1 one-section impedance transformer (1-D example), a capacitively-loaded 10:1 two-section impedance transformer (2-D example), and a third-order low-pass symmetrical lumped filter (2-D example). A final example is presented using a single-stub band-stop microstrip filter simulated in ADS (1-D example) where the full-wave EM simulation response is used as target.

Next, this chapter continues the proposal of using the Kullback-Leibler distance formulation as objective function for parameter extraction instead of the classical *l*-th norms, *i.e.*, Manhattan, Euclidean, and Chebyshev norms. A parameter extraction graphical and numerical study using *l*-th norms and the Kullback-Leibler formulation is performed for the single-stub band-stop microstrip filter simulated in ADS. This study is done to illustrate the advantages of this proposed Kullback-Leibler formulation with respect to *l*-th norm formulations.

3.1. Introduction

As mentioned, parameter extraction (PE) is an important subprocess of space mapping; any improvement in PE can create a positive impact in space mapping. This chapter presents a parameter extraction graphical study employing Kullback-Leibler (K-L) distance formulations as objective functions using coarse and fine models for several examples [Loera-Díaz-23b]. We compare formulations using natural logarithms against 10-base logarithms. Moreover, we compare formulations that consider the "direct order" versus the "reverse order" of the target responses and

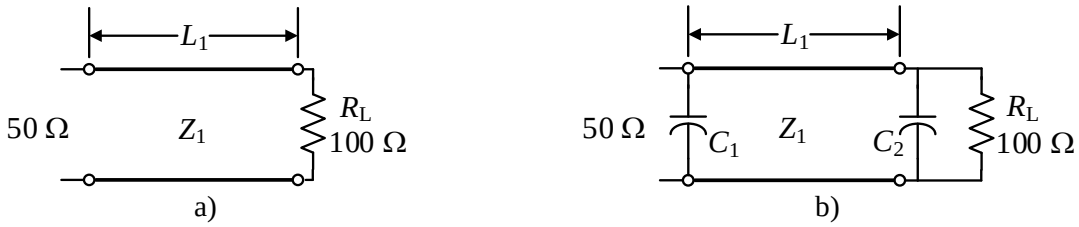

Fig. 3.1 One-section 2:1 impedance transformer: a) using an ideal transmission line (coarse model), b) using a capacitively-loaded ideal transmission line (fine model).

the model responses in the Kullback-Leibler formulation. This graphical study is applied to some synthetic circuit examples and to a single-stub band-stop microstrip filter. As synthetic examples, we consider a capacitively-loaded 2:1 one-section impedance transformer (1-D example), a capacitively-loaded 10:1 two-section impedance transformer (2-D example), and a third-order low-pass π-topology symmetrical lumped filter (2-D example). As a last example, we present a microstrip single-stub band-stop filter simulated in ADS (1-D example) where the full-wave EM simulation response is used as target.

Next, this microstrip filter is used to show a comparison of the performance of objective functions used for PE based on the K-L distance and the classical *l*-th norms [Loera-Díaz-24a]. A circuit model for this microstrip filter is implemented in Keysight ADS as a coarse model vehicle to perform PE, while the target response is obtained from a full-wave electromagnetic (EM) model implemented in ADS Momentum Microwave (fine model). Since this microstrip filter is a 1-variable PE problem and the coarse model is computationally cheap, we plot the objective function for each formulation to compare their behavior and to draw conclusions for more complex problems.

3.2. Study of the Kullback-Leibler Formulation for Parameter Extraction

As demonstrated in Chapter 2 [Loera-Díaz-20a], formulations based on the Kullback-Leibler distance [Kullback-51], [Do-02], [Veldhuis-03], [Vergara-09] can be effectively used as objective functions for the PE problem.

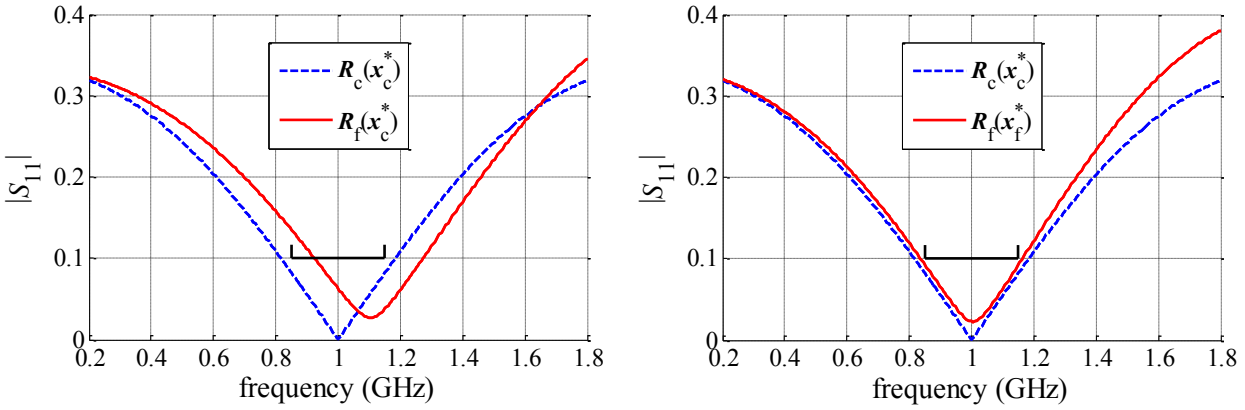

Fig. 3.2 One-section 2:1 impedance transformer coarse and fine model responses from 0.2 GHz to 1.8 GHz.

The objective function formulation based on the K-L distance using natural logarithm [Loera-Díaz-19b], can be defined as

$$U_{\mathrm{PE}}(\boldsymbol{R}^{\mathrm{t}}, \boldsymbol{R}(\boldsymbol{x})) = \sum_{i=1}^{r} \left\{ R_i^{\mathrm{t}} \ln \left| \frac{R_i^{\mathrm{t}}}{R_i(\boldsymbol{x})} \right| + (1 - R_i^{\mathrm{t}}) \ln \left| \frac{1-R_i^{\mathrm{t}}}{1-R_i(\boldsymbol{x})} \right| \right\} \tag{3-1}$$

where R_i is the i-th model response at model parameters $\boldsymbol{x}$, and R_i^{t} is the corresponding i-th target response (see Section 2.4).

This formulation using 10-base logarithms becomes

$$U_{\mathrm{PE}}(\boldsymbol{R}^{\mathrm{t}}, \boldsymbol{R}(\boldsymbol{x})) = \sum_{i=1}^{r} \left\{ R_i^{\mathrm{t}} \log_{10} \left| \frac{R_i^{\mathrm{t}}}{R_i(\boldsymbol{x})} \right| + (1 - R_i^{\mathrm{t}}) \log_{10} \left| \frac{1-R_i^{\mathrm{t}}}{1-R_i(\boldsymbol{x})} \right| \right\} \tag{3-2}$$

We refer to (3-1) and (3-2) as "direct order" K-L formulations.

If we consider the inverted order of (3-1) and (3-2), we get the following expressions

$$U_{\mathrm{PE}}(\boldsymbol{R}(\boldsymbol{x}), \boldsymbol{R}^{\mathrm{t}}) = \sum_{i=1}^{r} \left\{ R_i(\boldsymbol{x}) \ln \left| \frac{R_i(\boldsymbol{x})}{R_i^{\mathrm{t}}} \right| + (1 - R_i(\boldsymbol{x})) \ln \left| \frac{1-R_i(\boldsymbol{x})}{1-R_i^{\mathrm{t}}} \right| \right\} \tag{3-3}$$

$$U_{\mathrm{PE}}(\boldsymbol{R}(\boldsymbol{x}), \boldsymbol{R}^{\mathrm{t}}) = \sum_{i=1}^{r} \left\{ R_i(\boldsymbol{x}) \log_{10} \left| \frac{R_i(\boldsymbol{x})}{R_i^{\mathrm{t}}} \right| + (1 - R_i(\boldsymbol{x})) \log_{10} \left| \frac{1-R_i(\boldsymbol{x})}{1-R_i^{\mathrm{t}}} \right| \right\} \tag{3-4}$$

We refer to (3-3) and (3-4) as "reverse order" K-L formulations.

Contrary to the l-th norms, this formulation based on the K-L distances is not commutative in general, *i.e.*, (3-1) yields different numerical values than those in (3-3), and the same is applicable for (3-2) and (3-4).

To make better comparisons between the formulations used in this graphical study, the PE objective functions are normalized as follows,

$$U_{\mathrm{PE}}^{\mathrm{n}} = \frac{U_{\mathrm{PE}}(\boldsymbol{x})}{\max\limits_{i} \{\ldots U_{\mathrm{PE}}(\boldsymbol{x}^i) \ldots\}} \tag{3-5}$$

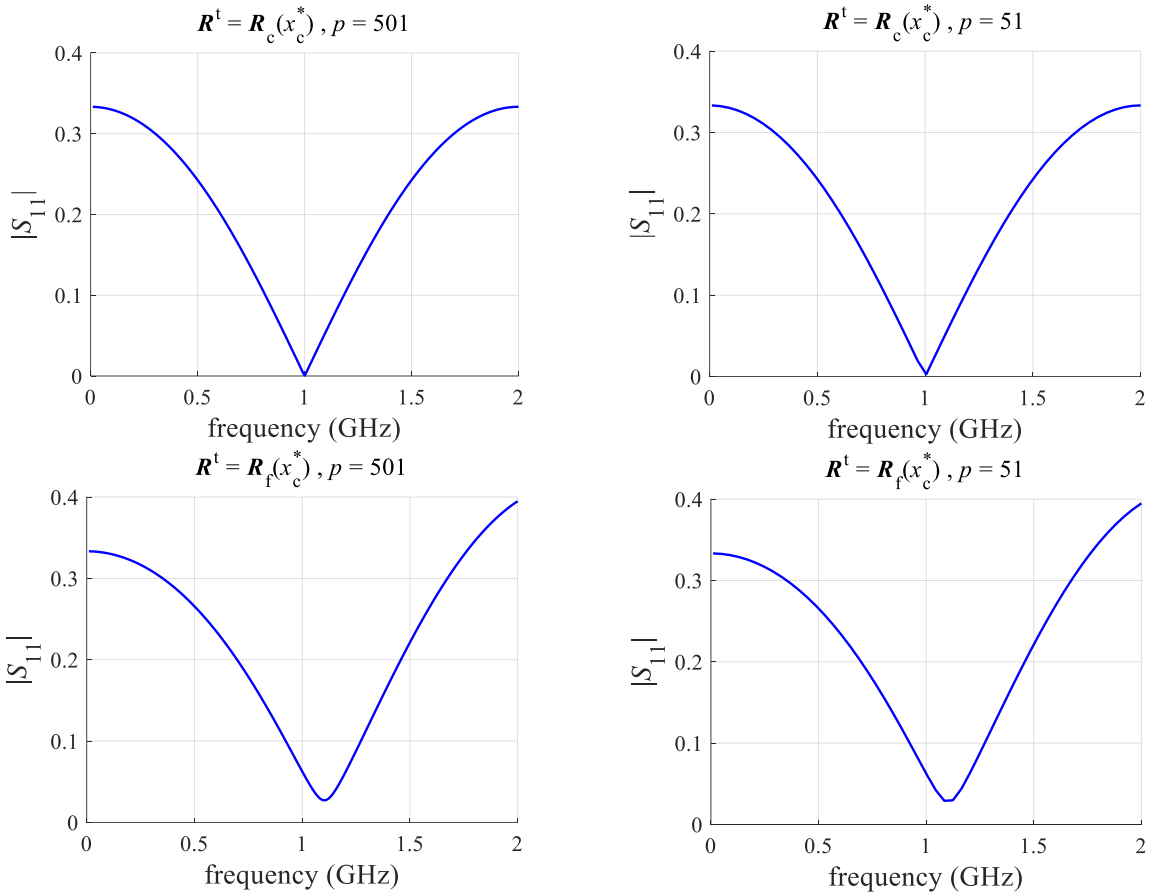

Fig. 3.3 Two different target responses for PE of the one-section 2:1 impedance transformer using a large and a small number of frequency points p.

where $U_{\mathrm{PE}}^{\mathrm{n}}$ is the normalized parameter extraction objective function, and the model parameters $\boldsymbol{x}^i \in \Re^n$ are evaluated in the whole domain of interest for plotting to get the maximum value of U_{PE}.

3.3. One-Section Impedance Transformer

As a first example, consider the capacitively-loaded 2:1 one-section impedance transformer shown in Fig. 3.1 (coarse and fine models).

3.3.1 Models Description

This 2:1 one-section impedance transformer uses a reference impedance Z_0 = 50 Ω and a

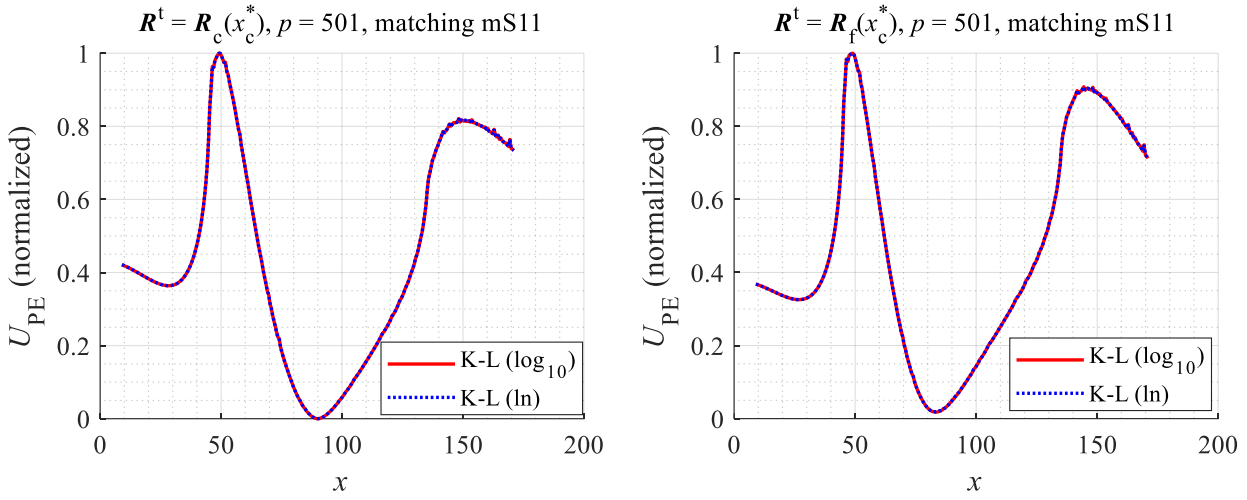

Fig. 3.4 Comparing Kullback-Leibler normalized PE objective functions using natural logarithm versus 10-base logarithm for the one-section 2:1 impedance transformer when matching $|S_{11}|$ for two different targets. It is seen that both objective function formulations yield equivalent results.

load impedance R_L = 100 Ω. The transmission line characteristic impedance in both coarse and fine models is kept fixed at $Z_1 = \sqrt{Z_0 R_L} = 70.7107$ Ω [Pozar-98].

The design parameter for this impedance transformer is $x = L_1$ (degrees); see Fig. 3.1. The fine model considers the following capacitances: C_1 = 0.5 pF and C_2 = 0.05 pF. The design specification is $|S_{11}| \leq 0.1$ for 0.85 GHz $\leq f \leq$ 1.15 GHz. The optimal design of the coarse model is x_c^* = 90 (degrees), and the optimal design of the fine model is x_f^* = 98.3721 (degrees).

3.3.2 Optimal Coarse and Fine Model Responses

The response of the coarse model at the optimal coarse model parameters, $\boldsymbol{R}_c(x_c^*)$, the response of the fine model at the optimal coarse model parameters, $\boldsymbol{R}_f(x_c^*)$, and the response of the fine model at the optimal fine model parameters, $\boldsymbol{R}_f(x_f^*)$, are compared in Fig. 3.2. The first target used for parameter extraction in a typical space mapping algorithm is $\boldsymbol{R}_f(x_c^*)$, while the last target is (ideally) $\boldsymbol{R}_c(x_c^*)$ [Rayas-Sánchez-16].

Fig. 3.3 shows a couple of target responses, $\boldsymbol{R}^t = \boldsymbol{R}_c(x_c^*)$ and $\boldsymbol{R}^t = \boldsymbol{R}_f(x_c^*)$, with a small ($p$ = 51) and large (p = 501) number of frequency points p. It is seen that in this frequency range, using 51 frequency points is a reduced but still reasonable number of points.

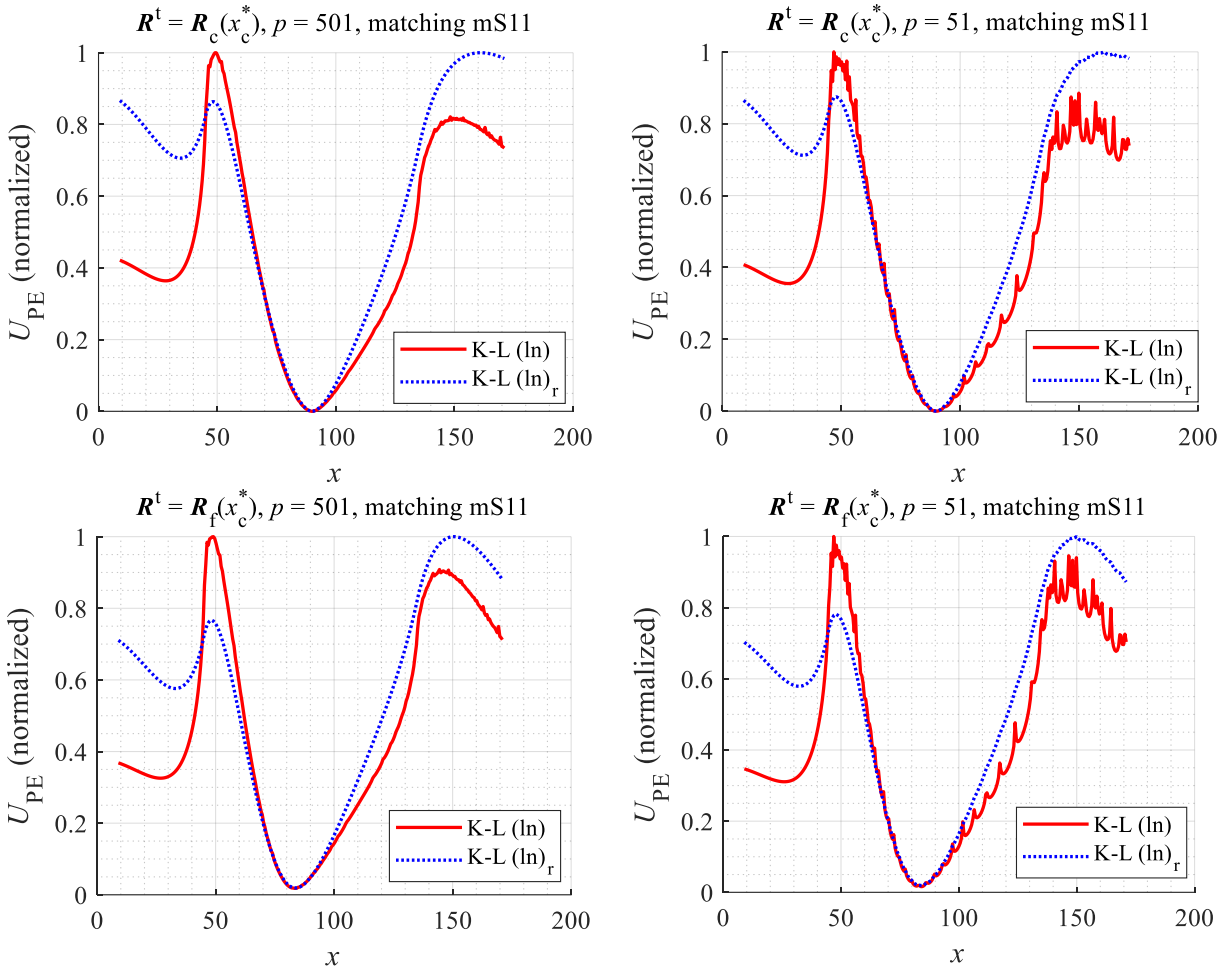

Fig. 3.5 Comparing Kullback-Leibler normalized PE objective functions with natural logarithm using direct formulation versus reverse formulation for the 2:1 one-section impedance transformer when matching $|S_{11}|$ with a large and a small number of frequency points p. It is seen that the reverse formulation yields much better results.

3.3.3 PE Objective Function Plots

A comparison of PE objective functions (3-1) and (3-2) is shown in Fig. 3.4 considering the target $\boldsymbol{R}^t = \boldsymbol{R}_c(x_c^*)$ and $\boldsymbol{R}^t = \boldsymbol{R}_f(x_c^*)$ with p = 501; these responses have been normalized according to (3-5). We can see from these plots that the normalized PE objective functions using the K-L formulation with natural logarithm and 10-base logarithm are the same. This behavior is true also when using other targets, such as $\boldsymbol{R}^t = \boldsymbol{R}_c(x_f^*)$ or $\boldsymbol{R}^t = \boldsymbol{R}_f(x_f^*)$, (the corresponding results are omitted for brevity).

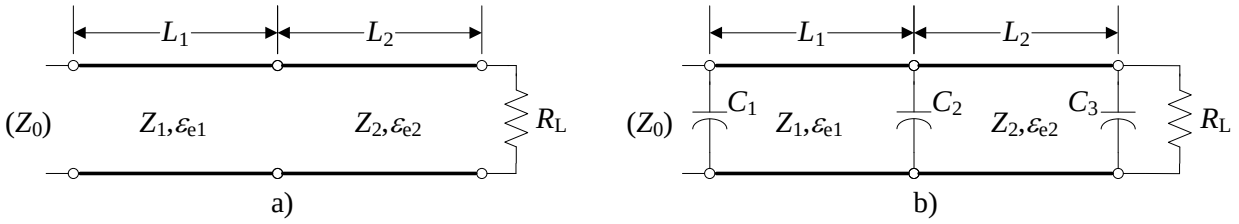

Fig. 3.6 Two-section 10:1 impedance transformer: a) using ideal transmission lines (coarse model), b) using capacitively-loaded ideal transmission lines (fine model).

Finally, we compare in Fig. 3.5 the normalized PE objective functions obtained using the direct K-L formulation (3-1) versus the reverse K-L formulation (3-3) for the targets $\boldsymbol{R}^t = \boldsymbol{R}_c(x_c^*)$ and $\boldsymbol{R}^t = \boldsymbol{R}_f(x_c^*)$ with a small number of frequency points (p = 51) and a large number of frequency points (p = 501). As we can see from this figure, the K-L formulation in the direct order can be severely affected when the responses are calculated using a relatively small number of frequency points, yielding too many local minima. On the other hand, many local minima do not appear for the reverse formulation regardless of the number of points used as the independent variable. Once again, this behavior is also true for the targets $\boldsymbol{R}^t = \boldsymbol{R}_c(x_f^*)$ and $\boldsymbol{R}^t = \boldsymbol{R}_f(x_f^*)$, (results are omitted for brevity).

3.4. Two-Section Impedance Transformer

As a second example, consider the capacitively-loaded 10:1 two-section impedance transformer shown in Fig. 3.6 (coarse and fine models).

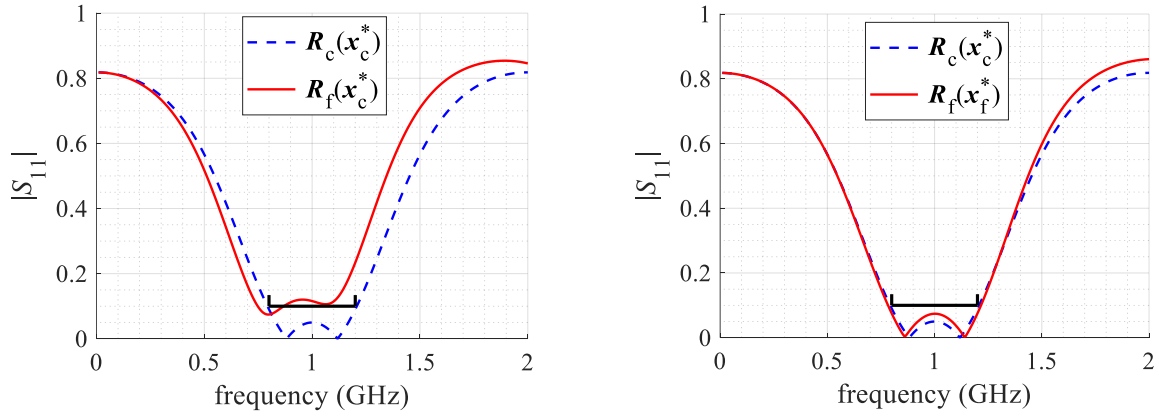

Fig. 3.7 Two-section 10:1 impedance transformer coarse and fine model responses from 0 GHz to 2 GHz.

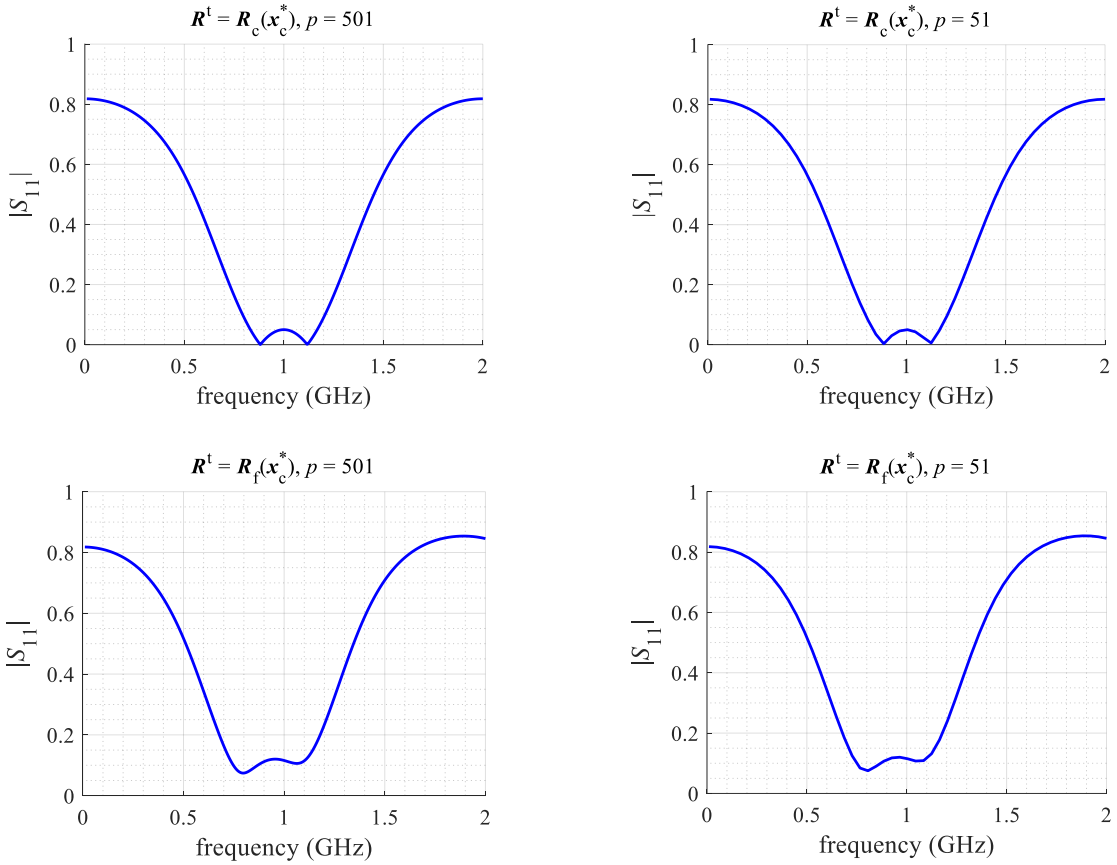

Fig. 3.8 Two different target responses for PE for the two-section 10:1 impedance transformer using a large and a small number of frequency points p.

3.4.1 Models Description

The reference impedance of this impedance transformer is Z_0 = 50 Ω and load impedance is R_L = 500 Ω. The design parameters for this impedance transformer are $\boldsymbol{x} = [L_1 \quad L_2]^T$ (degrees); see Fig. 3.6 [Pozar-98].

The transmission line characteristic impedances in both coarse and fine models are kept fixed at $Z_1 = 1.8233Z_0$ Ω and $Z_2 = 5.4845Z_0$ Ω, with $\varepsilon_{e1} = \varepsilon_{e2} = 1$, and using coefficients for Chebyshev profile with a 10:1 transformation ratio and a 0.05 ripple [Pozar-98]. The fine model capacitors are C_1 = 0.4 pF, C_2 = 0.2 pF, C_3 = 0.1 pF.

The design specification for this impedance transformer is $|S_{11}| \leq 0.1$ for 0.8 GHz $\leq f \leq$ 1.2 GHz. The optimal design parameters of the coarse model are $\boldsymbol{x}_c^* = [90 \quad 90]^T$ and the optimal design parameters for the fine model are $\boldsymbol{x}_f^* = [79.0673 \quad 88.6163]^T$.

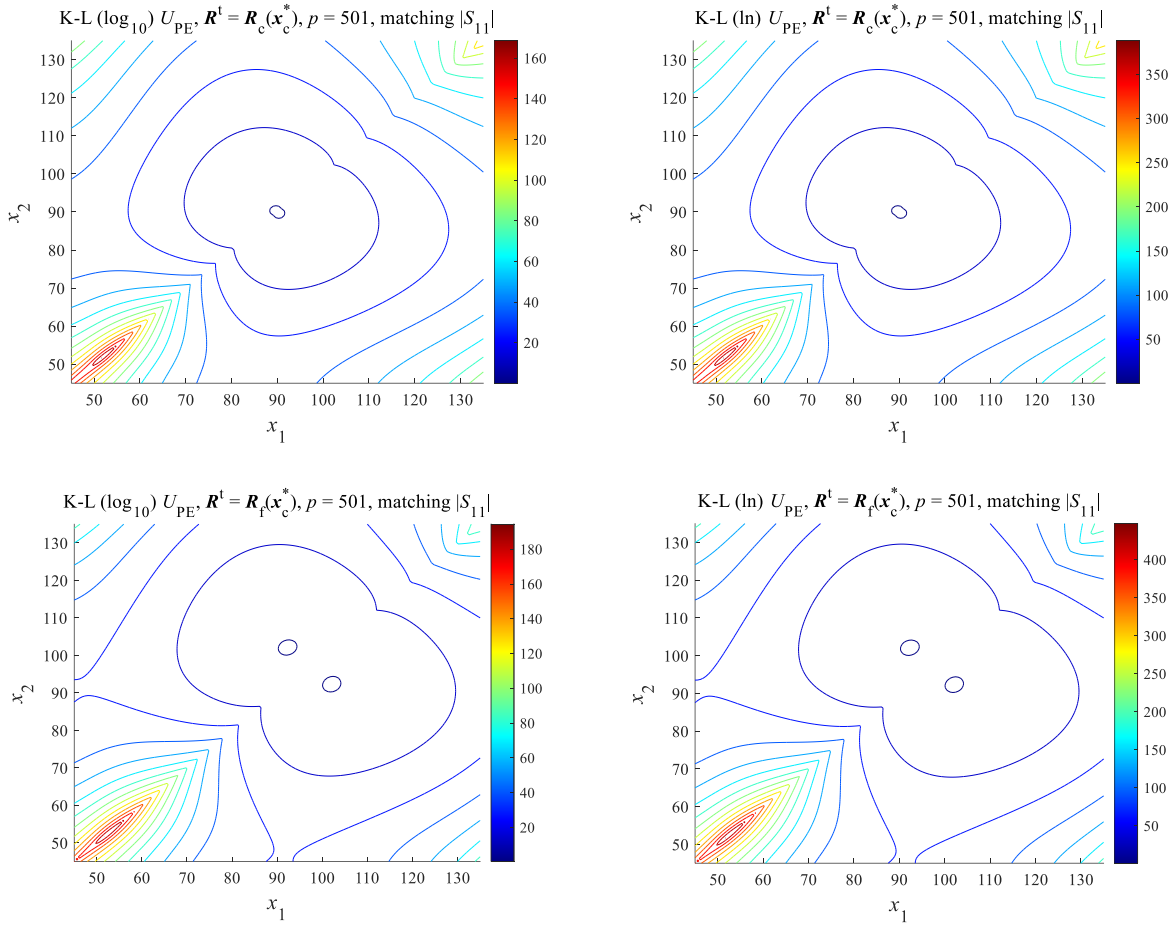

Fig. 3.9 Comparing Kullback-Leibler PE objective functions using 10-base logarithm (left hand side plots) versus natural logarithm (right hand side plots) for the two-section 10:1 impedance transformer when matching $|S_{11}|$ for two different targets. It is seen that both K-L formulations yield equivalent results (same contour plots).

3.4.2 Optimal Coarse and Fine Model Responses

Fig. 3.7 shows a comparison of the coarse model response at the optimal coarse model parameters, $\boldsymbol{R}_c(x_c^*)$, the response of the fine model at the optimal coarse model parameters, $\boldsymbol{R}_f(x_c^*)$, and the response of the fine model at the optimal fine model parameters $\boldsymbol{R}_f(x_f^*)$.

Fig. 3.8 shows some target responses, $\boldsymbol{R}^t = \boldsymbol{R}_c(x_c^*)$ and $\boldsymbol{R}^t = \boldsymbol{R}_f(x_c^*)$, with a large number of frequency points (p = 501) and a small number of frequency points (p = 51). Once again, it is seen that using p = 51 the responses are sufficiently well represented.

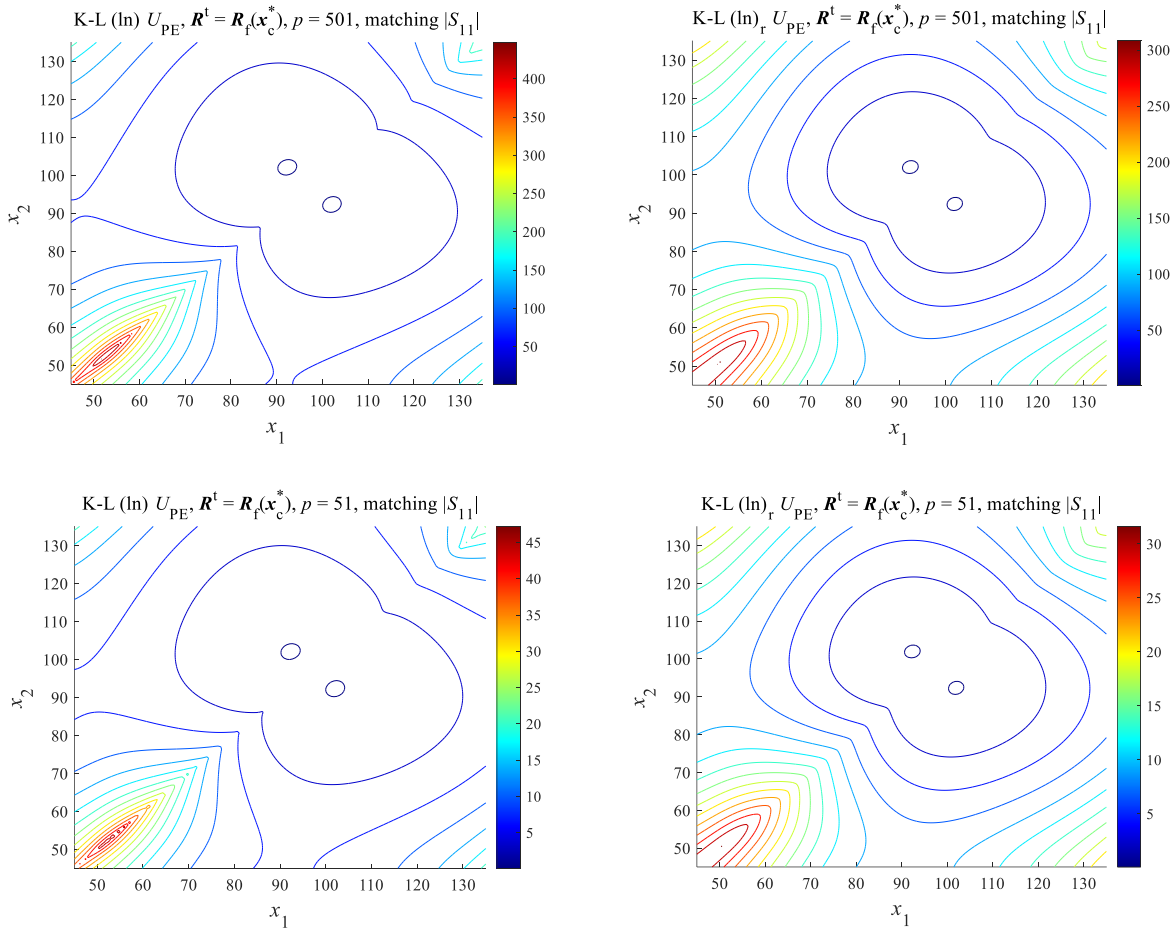

Fig. 3.10 Comparing Kullback-Leibler PE objective functions with direct (left hand side plots) versus reverse (right hand side plots) formulations using natural logarithm for the two-section 10:1 impedance transformer when matching $|S_{11}|$ with a large and a small number of frequency points p. It is seen that the reverse formulation yields better results.

3.4.3 PE Objective Function Plots

Fig. 3.9 shows some 2D plots of the (unnormalized) PE objective functions for a couple of targets, $\boldsymbol{R}^t = \boldsymbol{R}_c(x_c^*)$ and $\boldsymbol{R}^t = \boldsymbol{R}_f(x_c^*)$, with 501 frequency points, using natural logarithm versus 10-base logarithm. We can see from this figure that the PE formulation with natural algorithm (3-1) and the formulation with 10-base algorithm (3-2) yield equivalent results (the same contour plots). This behavior is also observed for $\boldsymbol{R}^t = \boldsymbol{R}_c(x_f^*)$ and $\boldsymbol{R}^t = \boldsymbol{R}_f(x_f^*)$, (results are omitted for brevity).

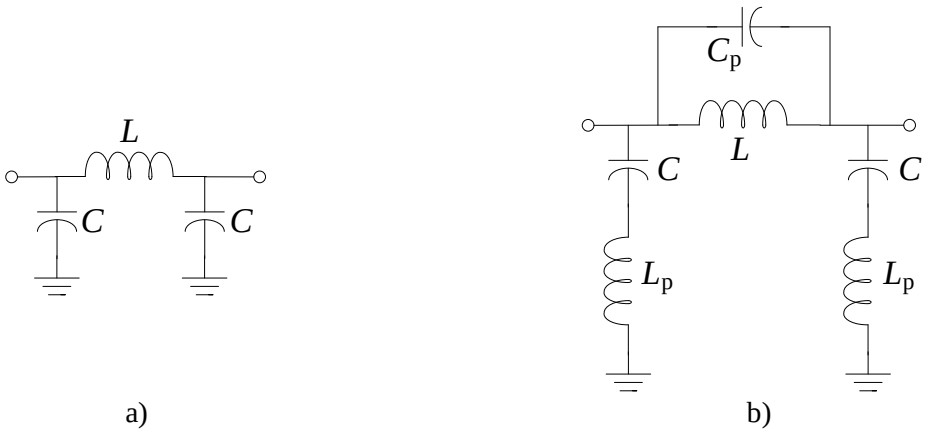

Fig. 3.11 Third-order low-pass π-topology symmetrical lumped filter: a) coarse model, b) fine model considering the parasitic elements L_p and C_p.

Fig. 3.10 shows a comparison of the PE objective functions with direct K-L formulation (3-1) versus the reverse K-L formulation (3-3) for the target $\boldsymbol{R}^t = \boldsymbol{R}_f(x_c^*)$ using a small and a large number of frequency points for the natural logarithm formulations. We can see from this figure that the PE objective function using K-L distance with reverse formulation yields better results than the ones obtained with direct formulation, since the reverse formulation produces softer contours with better defined minima, especially when the number of frequency points is relatively small. A similar behavior is observed when using other target responses: $\boldsymbol{R}^t = \boldsymbol{R}_c(x_c^*)$, $\boldsymbol{R}^t = \boldsymbol{R}_f(x_f^*)$ and $\boldsymbol{R}^t = \boldsymbol{R}_c(x_f^*)$ (results omitted for brevity).

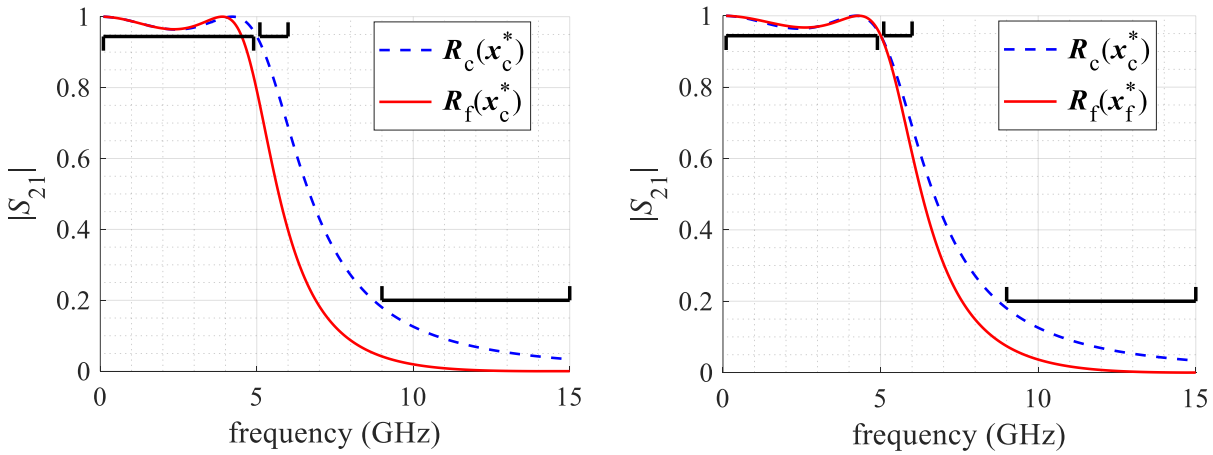

Fig. 3.12 Third-order low-pass π-topology symmetrical lumped filter coarse and fine model responses from 0 GHz to 15 GHz.

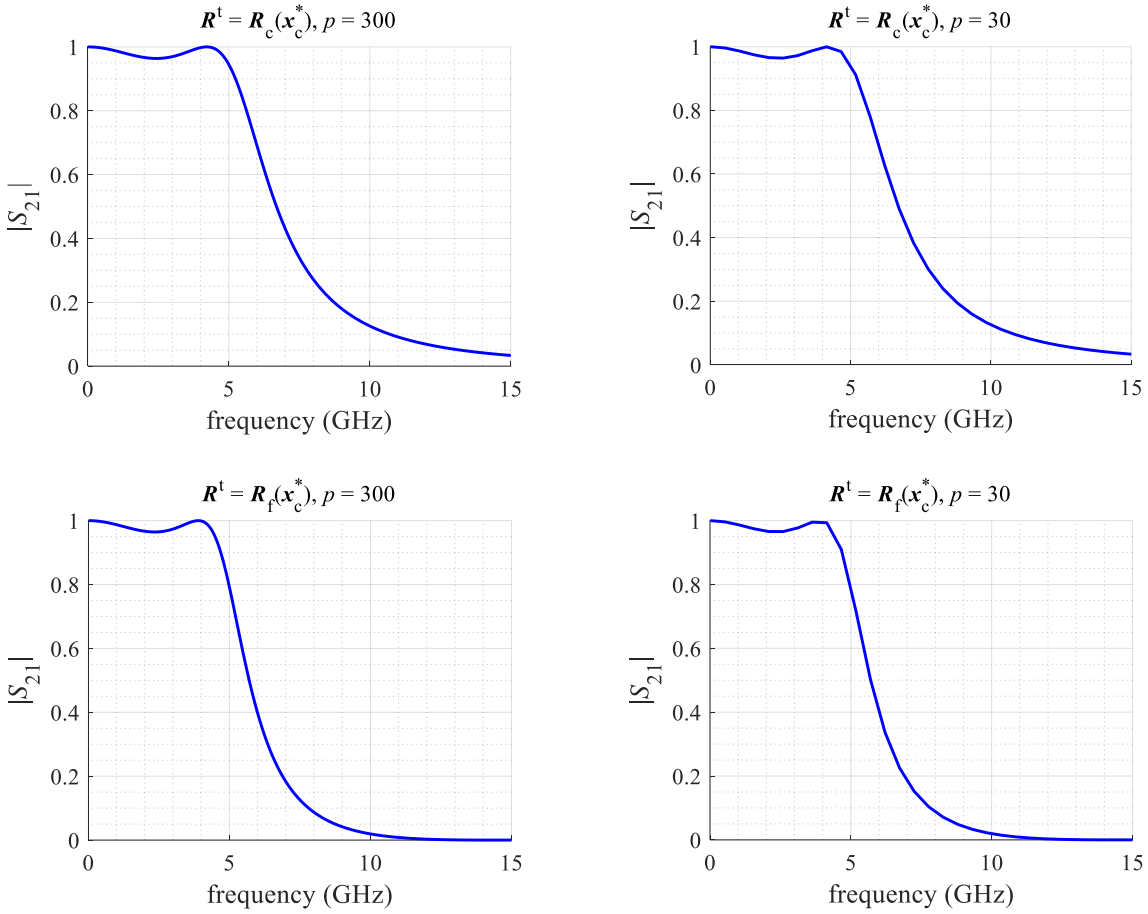

Fig. 3.13 Two different target responses for PE for the third-order low-pass symmetrical π-topology lumped filter with a large and a small number of frequency points *p*.

3.5. Third-Order Low-Pass Symmetrical Lumped Filter

As a third example, consider the third-order low-pass π-topology symmetrical lumped filter shown in Fig. 3.11 (coarse and fine models).

3.5.1 Models Description

The coarse model of this lumped filter does not consider parasitic components. On the other hand, the fine model includes the parasitic inductance L_p and the parasitic capacitance C_p.

The design parameters for this low-pass filter are $\boldsymbol{x} = [L(\text{nH}) \quad C(\text{pF})]^T$. The fine model considers the parasitic inductance $L_p = 0.11$ nH and the parasitic capacitance $C_p = 0.07$ pF.

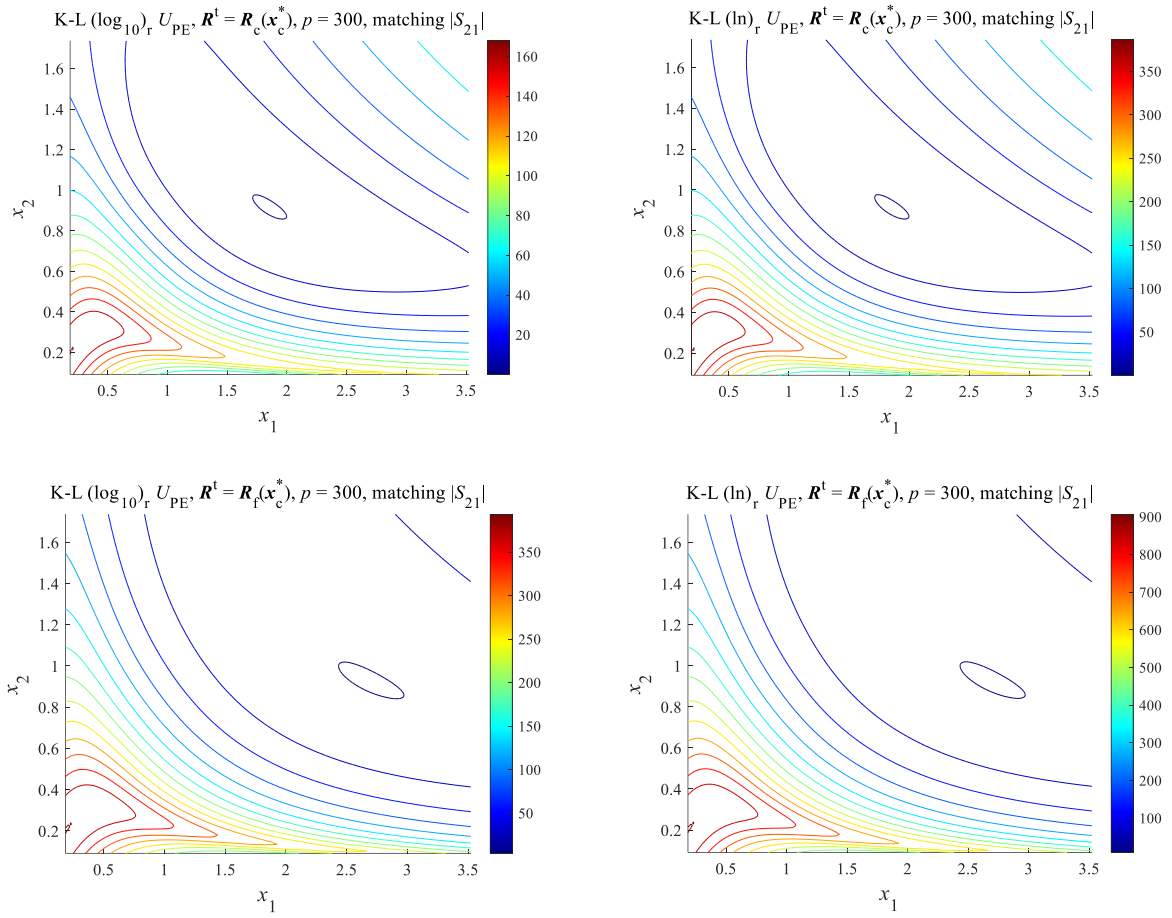

Fig. 3.14 Comparing Kullback-Leibler PE objective functions using 10-base logarithm (left hand side plots) versus natural logarithm (right hand side plots) for the third-order low-pass symmetrical π-topology lumped filter when matching $|S_{21}|$ for two different targets. It is seen that both K-L formulations yield equivalent results (same contour plots).

The design specifications for this filter are $|S_{21}| \geq 0.9441$ for 0.1 GHz $\leq f \leq$ 4.9 GHz, $|S_{21}| \leq 0.9441$ for 5.1 GHz $\leq f \leq$ 6.0 GHz, and $|S_{21}| \leq 0.2$ for 9 GHz $\leq f \leq$ 15 GHz. The optimal design parameters for the coarse model are $\boldsymbol{x}_c^* = [1.8538 \quad 0.9136]^T$, and the optimal design parameters for the fine model are $\boldsymbol{x}_f^* = [1.6703 \quad 0.8031]^T$.

3.5.2 Optimal Coarse and Fine Model Responses

The response of the coarse model at its optimal design parameters $\boldsymbol{R}_c(x_c^*)$, the response of the fine model at the optimal coarse model parameters $\boldsymbol{R}_f(x_c^*)$, and the response of the fine model at its optimal design parameters $\boldsymbol{R}_f(x_f^*)$ are shown in Fig. 3.12.

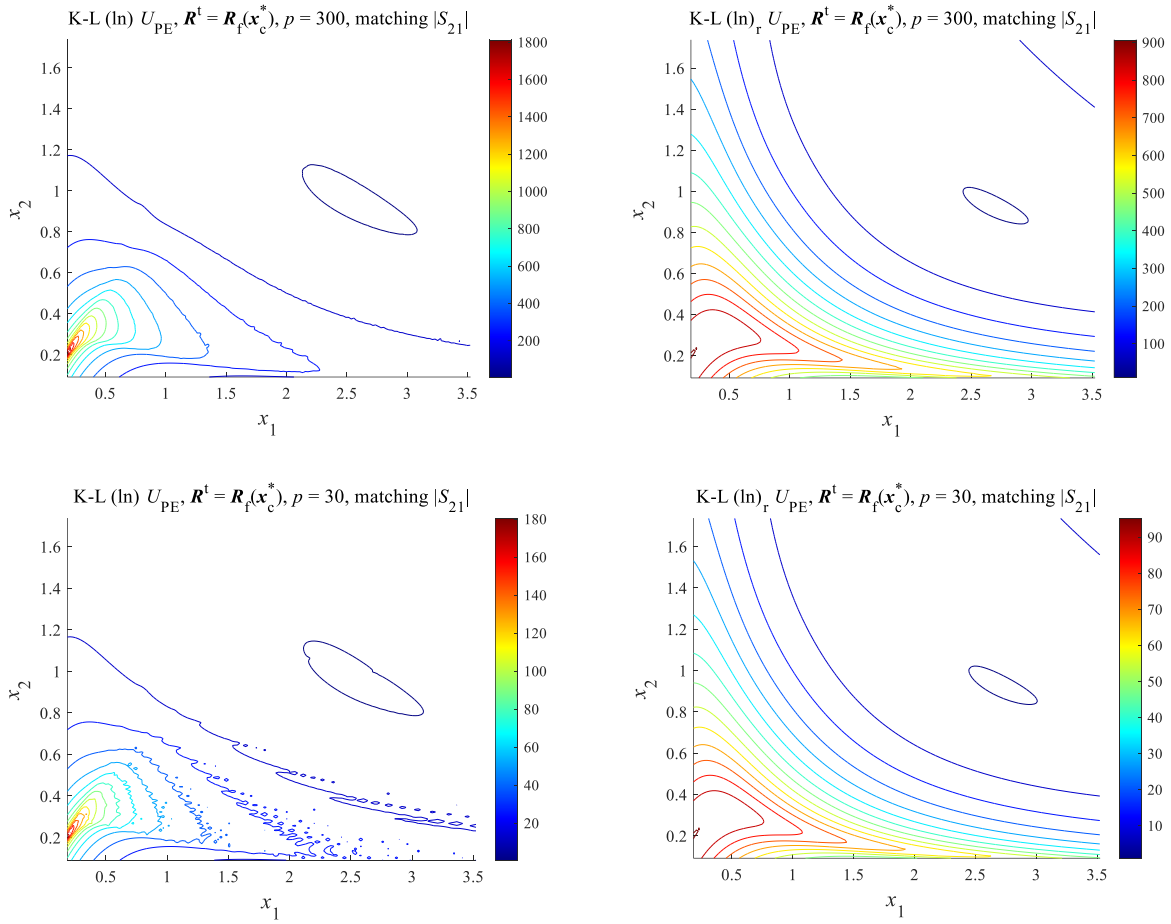

Fig. 3.15 Comparing Kullback-Leibler PE objective functions using direct (left hand side plots) versus reverse (right hand side plots) formulations with natural logarithm for the third-order low-pass symmetrical π-topology lumped filter when matching $|S_{21}|$ with a large and a small number of frequency points p. It is seen that the reverse formulation yields much better results.

Fig. 3.13 shows the target responses $\boldsymbol{R}^t = \boldsymbol{R}_c(x_c^*)$ and $\boldsymbol{R}^t = \boldsymbol{R}_f(x_c^*)$ with a large number of frequency points (p = 300) and a relatively small number of frequency points (p = 30). Again, it is seen that 30 frequency points in this frequency range is a small but reasonable number of points.

3.5.3 PE Objective Function Plots

Fig. 3.14 shows some 2D plots of the (unnormalized) PE objective functions for the targets $\boldsymbol{R}^t = \boldsymbol{R}_c(x_c^*)$ and $\boldsymbol{R}^t = \boldsymbol{R}_f(x_c^*)$, with 300 frequency points, using natural logarithm (3-1) versus 10-base logarithm (3-2). We can see from these plots that both logarithms yield an equivalent behavior for both targets (the same contour plots). Once again, this behavior is true for $\boldsymbol{R}^t = \boldsymbol{R}_c(x_f^*)$ and $\boldsymbol{R}^t$

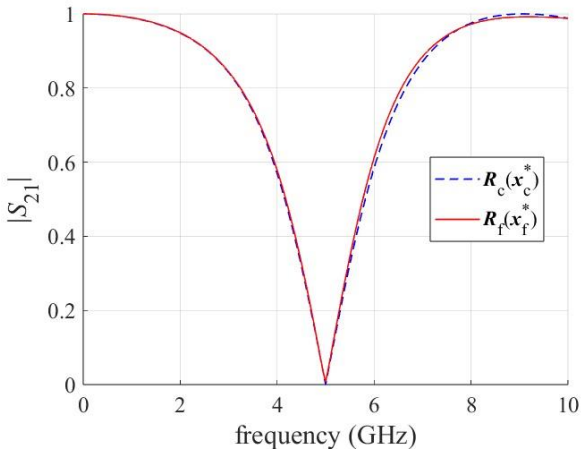

Fig. 3.16 Microstrip single-stub stop-band filter coarse and fine model optimal responses from 0 GHz to 10 GHz using p = 101 frequency points.

$= \boldsymbol{R}_f(x_f^*)$, (results are omitted for brevity).

Finally, Fig. 3.15 shows a comparison of the PE objective functions with the direct formulation (3-1) and the reverse formulation (3-3) for the target $\boldsymbol{R}^t = \boldsymbol{R}_f(x_c^*)$, using natural logarithm, with a large number of frequency points (p = 300) versus a small number of frequency points (p = 30). We can see from these plots that the reverse formulation yields much better results than the direct formulation since the reverse formulation produces softer contours and better defined minima, especially when the number of frequency points used is relatively small. In this last case, the direct formulation produces many local minima. This behavior is also true for $\boldsymbol{R}^t = \boldsymbol{R}_c(x_c^*)$, $\boldsymbol{R}^t = \boldsymbol{R}_c(x_f^*)$ and $\boldsymbol{R}^t = \boldsymbol{R}_f(x_f^*)$, (results are omitted for brevity).

3.6. Microstrip Single-Stub Band-Stop Filter

We consider as last example the microstrip single-stub band-stop filter described in Section 1.3, reported in [Koziel-08] (see Fig. 1.1).

TABLE 3.1. CONFIGURATION OF ADS MOMENTUM FOR THE MICROSTRIP SINGLE-STUB BAND-STOP FILTER

Mesh density (cells/λ)	Edge mesh	Transmission line mesh	Thin layer overlap extraction	Port feed type
20	Auto	20	Aggressive	TML

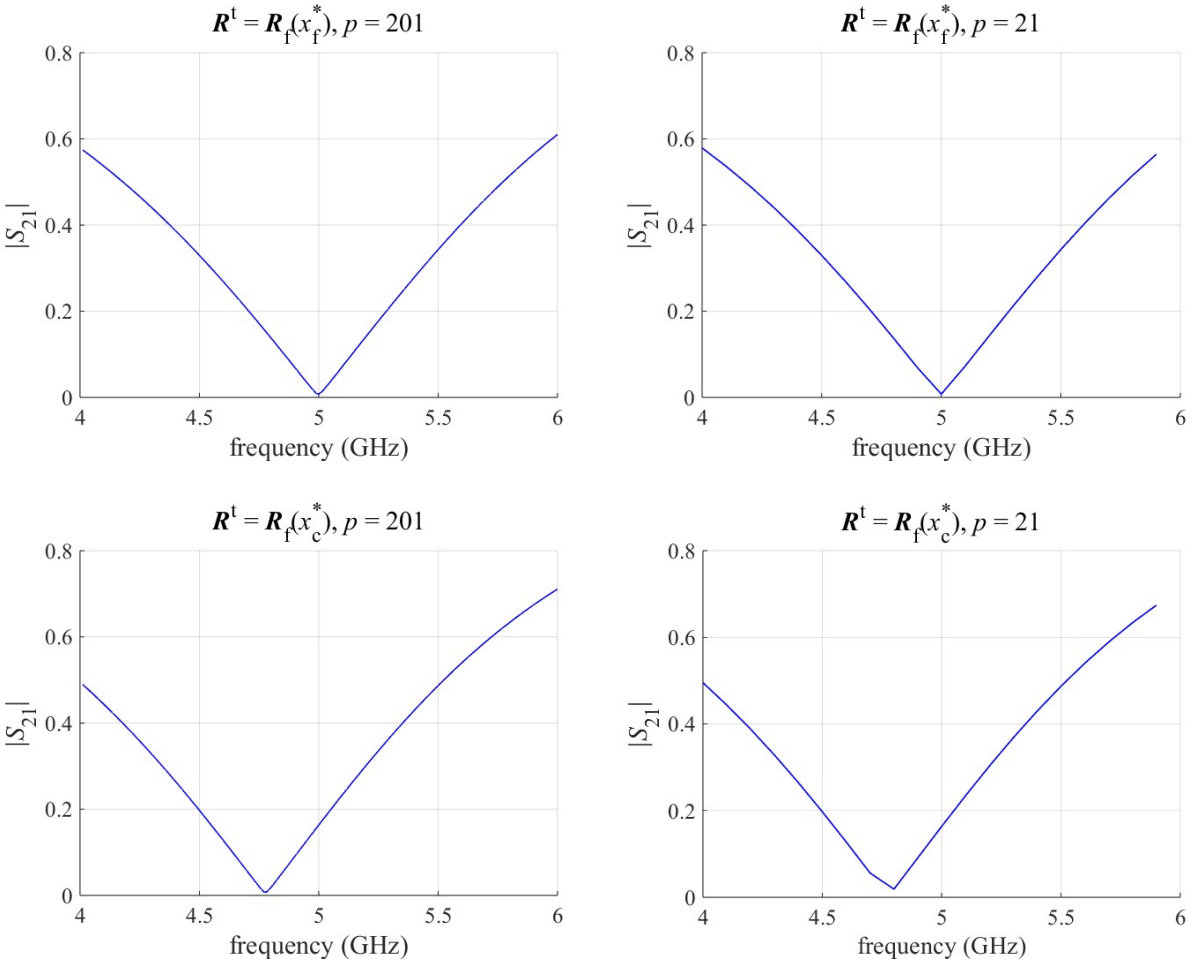

Fig. 3.17 Two different target responses for PE for the microstrip single-stub stop-band filter using a large and a small number of frequency points p.

3.6.1 Models Description

As mentioned in [Loera-Díaz-23b], some parameter values are modified in the microstrip single-stub band-stop filter used in this chapter with respect to those used in [Koziel-08]. Fig. 1.2 shows the microstrip filter used in this chapter.

This microstrip filter has only one design parameter, $x = L$ (mm), which corresponds to the open stub length. The pre-assigned parameters are $\boldsymbol{z} = [H\ \ \varepsilon_{\mathrm{r}}\ \ W\ \ L_1]^{\mathrm{T}}$. In this example, the substrate thickness is $H = 1$ mm, the relative permittivity is $\varepsilon_{\mathrm{r}} = 9.3$, and the microstrips width is $W = 1$ mm, so that the input and output microstrips are matched, *i.e.*, $Z_0 = 50.04\ \Omega \approx 50\ \Omega$, with a fixed length $L_1 = 5$ mm. Losses are neglected (zero loss tangent and infinitesimally thin perfect metals).

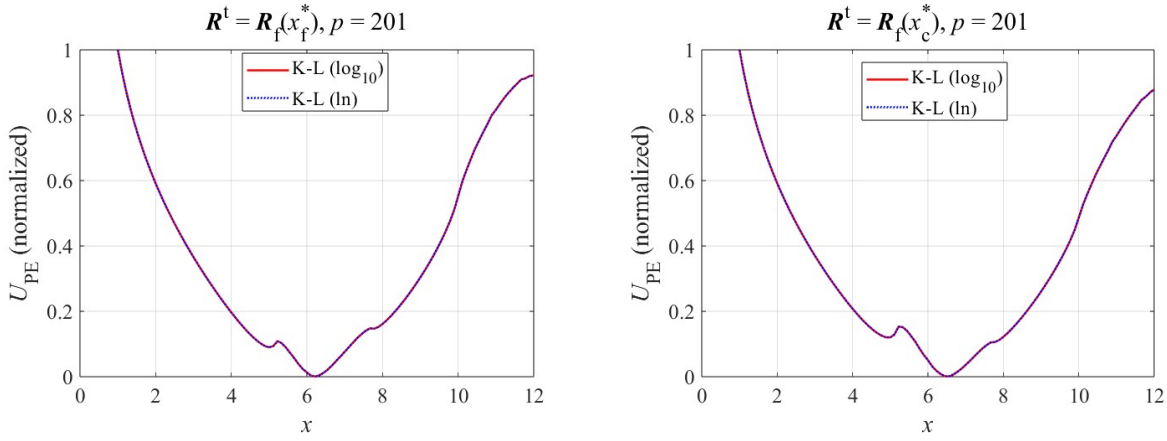

Fig. 3.18 Comparing Kullback-Leibler normalized PE objective functions using natural logarithm versus 10-base logarithm for the microstrip single-stub stop-band filter when matching $|S_{21}|$ for two different targets.

To obtain the responses of the PE objective functions varying the design parameter x, a utility Matlab function is required to drive Keysight ADS. This Matlab driver for ADS was made according to [Leal-Romo-17] and [Rayas-Sánchez-20].

3.6.2 Optimal Coarse and Fine Model Responses

The response of the coarse model for the microstrip single-stub band-stop filter is obtained from the circuit model in ADS shown in Fig. 1.3. The response of the fine model is obtained from the layout shown in Fig. 1.4, simulated in ADS Momentum Microwave with the configuration shown in Table 3.1. Fig. 3.16 shows the responses of the coarse and fine models at their optimal design parameters, $\boldsymbol{R}_c(x_c^*)$ and $\boldsymbol{R}_f(x_f^*)$. In this example, the design specification simply consists of making $|S_{21}| = 0$ at 5 GHz.

The target responses for PE are shown in Fig. 3.17, where we use $\boldsymbol{R}^t = \boldsymbol{R}_f(x_f^*)$ and $\boldsymbol{R}^t = \boldsymbol{R}_f(x_c^*)$ with a large ($p = 201$) and a small ($p = 21$) number of frequency points. Once again, using $p = 21$ is a much reduced number of frequency points but still sufficient to reproduce the essential behavior of the response.

3.6.3 PE Objective Function Plots

A comparison between normalized PE objective functions using natural logarithm (3-1)

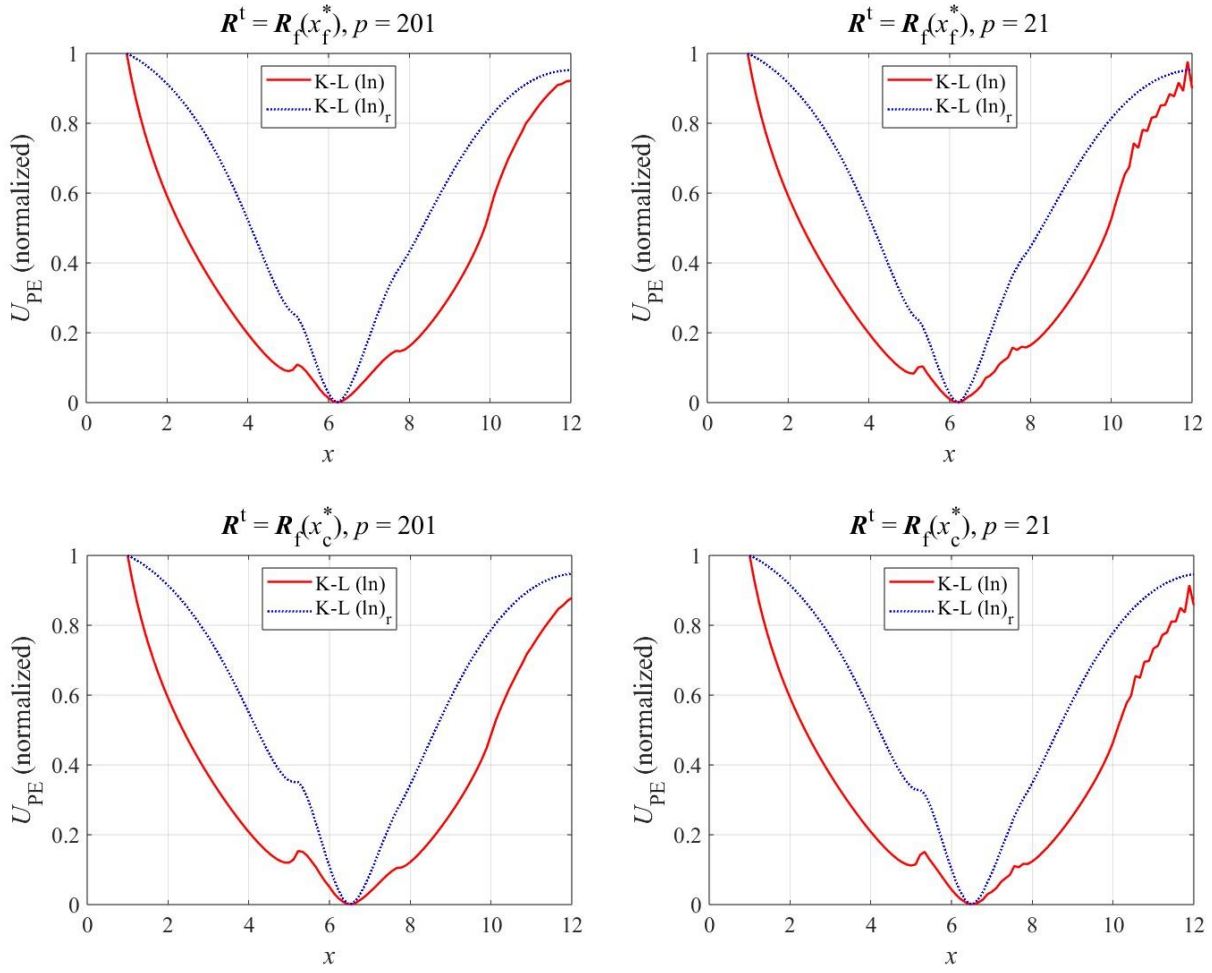

Fig. 3.19 Two different target responses for PE for the microstrip single-stub stop-band filter using a large and a small number of frequency points p.

versus 10-base logarithm (3-2) for the targets $\boldsymbol{R}^t = \boldsymbol{R}_f(x_f^*)$ and $\boldsymbol{R}^t = \boldsymbol{R}_f(x_c^*)$ with 201 frequency points is shown in Fig. 3.18. We can see from this figure that both natural and 10-base logarithms yield the same results.

Finally, a comparison of normalized PE objective functions using the direct and reverse K-L formulation for the same previous targets, with natural logarithm, using a large (p = 201) and a small (p = 21) number of frequency points is shown in Fig. 3.19. We can see from these plots that the direct formulation yields more local minima, especially when the number of frequency points is relatively small, and the reverse formulation yields a softer objective function with a better defined minimum, as in all the previous examples.

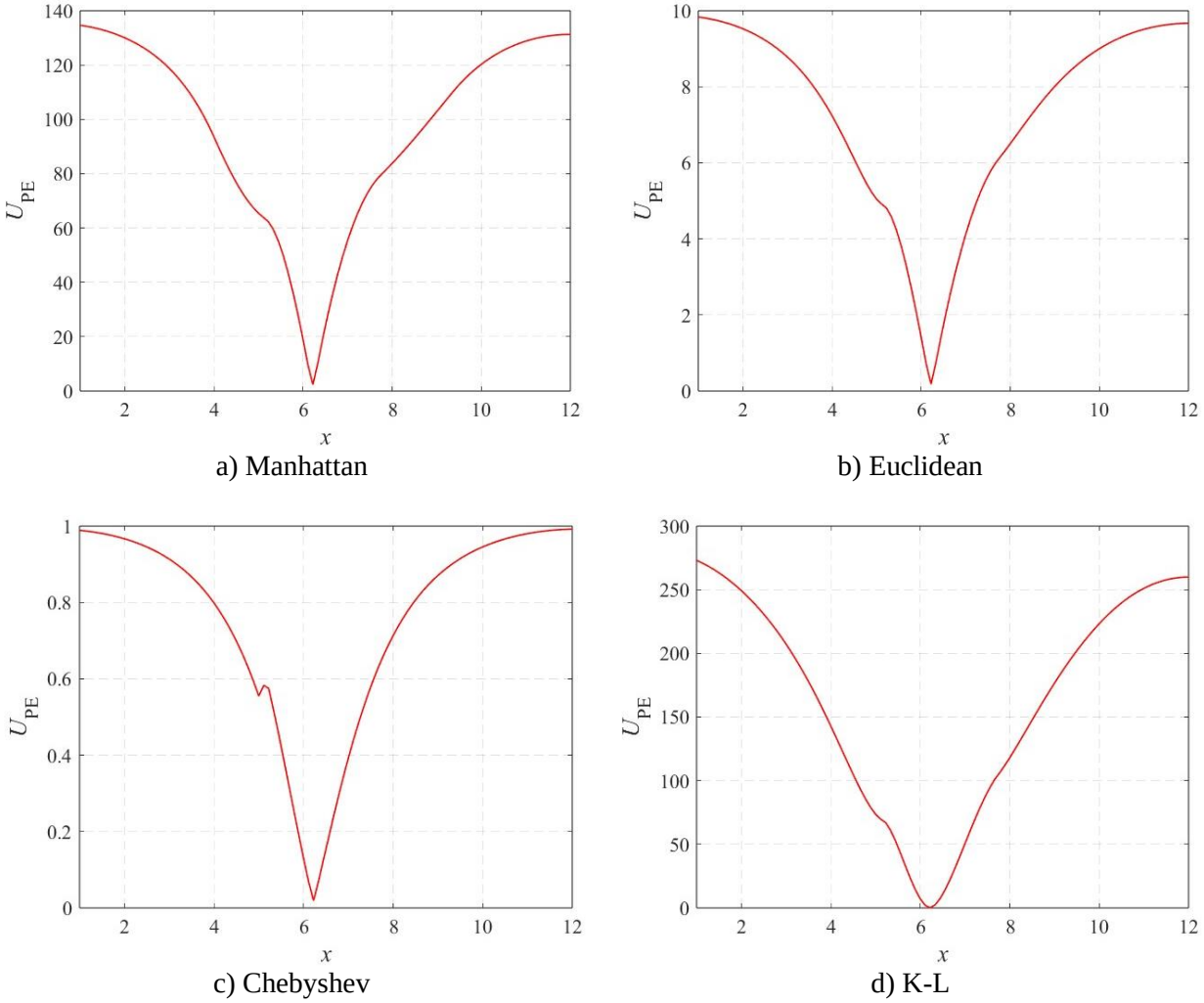

Fig. 3.20 PE objective functions U_{PE} versus x for $\boldsymbol{R}^t = \boldsymbol{R}_f(x_f^*)$, varying $x = L$ from 1 mm to 12 mm, using frequency sweeps from 4 GHz to 6 GHz with 201 frequency points.

3.6.4 Parameter Extraction

The objective functions defined in Section 2.3 (classical norms) and Section 2.4 (K-L formulation) are now employed in the following two different cases for parameter extraction.

3.6.4.1 Case 1: Using as Target the Fine Model Response at its Optimal Design

As first case for PE, we consider as target response the full-wave EM response obtained in ADS Momentum Microwave at the optimum design parameters of the fine model, *i.e.*, $\boldsymbol{R}^t = \boldsymbol{R}_f(x_f^*)$.

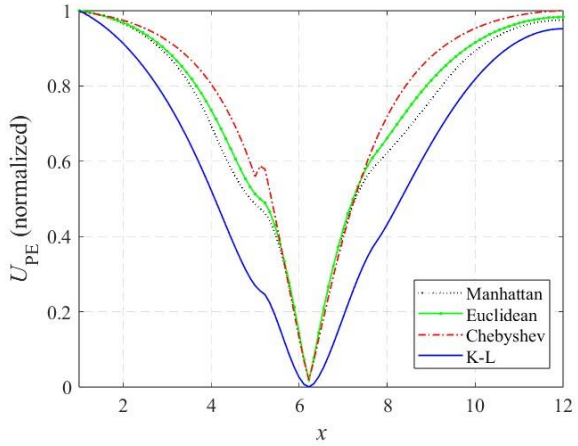

Fig. 3.21 Normalized PE objective functions U_{PE} versus x for $\boldsymbol{R}^t = \boldsymbol{R}_f(x_f^*)$, varying $x = L$ from 1 mm to 12 mm, using frequency sweeps from 4 GHz to 6 GHz with 201 frequency points.

We refer to this first case as Case 1.

3.6.4.2 Case 2: Using as Target the Fine Model Response at the Optimal Coarse Model Design

As a second case for PE, we use as target response the full-wave EM response obtained in ADS Momentum Microwave at the optimum design parameters of the coarse model, *i.e.*, $\boldsymbol{R}^t = \boldsymbol{R}_f(x_c^*)$. We refer to this second case as Case 2.

Case 2 is relevant because this is typically the first target used in parameter extraction for space mapping optimization.

3.6.5 A Graphical Comparison of the Objective Functions Used in PE

In this section we perform a graphical comparison of all the objective function formulations for PE described in Sections 2.3 and 2.4. Since the single-stub band-stop microstrip filter uses only one design parameter, $x = L$, it is possible to plot the relationship between the model parameter x against the parameter extraction objective function U_{PE} for the l-th norms and the Kullback-Leibler formulation. All the plots in this section were obtain by varying $x = L$ from 1 mm to 12 mm with 100 points for x, with frequency sweeps from 4 GHz to 6 GHz to calculate $|S_{21}|$ using 201 frequency points per sweep.

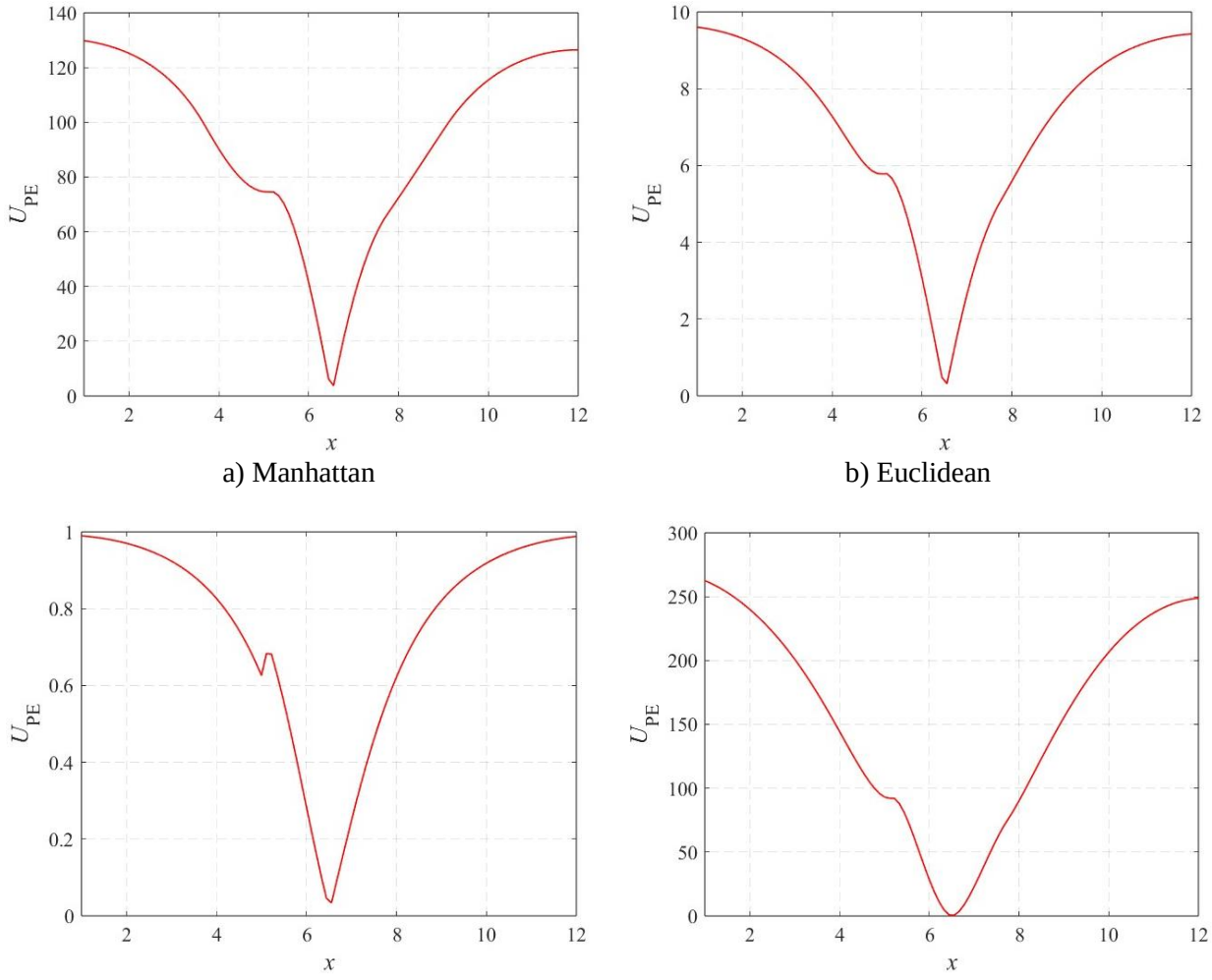

Fig. 3.22 PE objective functions U_{PE} versus x for $\boldsymbol{R}^t = \boldsymbol{R}_f(x_c^*)$, varying $x = L$ from 1 mm to 12 mm, using frequency sweeps from 4 GHz to 6 GHz with 201 frequency points.

To obtain the responses of the PE objective functions varying the design parameter x, a utility Matlab function is required to drive Keysight ADS [Leal-Romo-17] and [Rayas-Sánchez-20]. This Matlab function drives the ADS equivalent circuit model of the single-stub band-stop microstrip filter used as coarse model.

Fig. 3.20 shows the PE objective functions U_{PE} against the model parameter x for Case 1, where $\boldsymbol{R}^t = \boldsymbol{R}_f(x_f^*)$. As mentioned in Section 3.2, to make a better comparison, we use a normalized PE objective function, U_{PE}^n, calculated by (3-5) where the model parameters $\boldsymbol{x}^i \in \Re^n$ are evaluated in the whole domain of interest for plotting.

Fig. 3.21 shows the normalized PE objective functions, where it is seen that the K-L

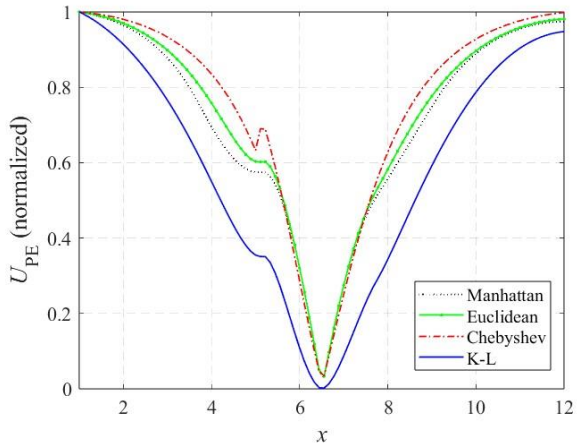

Fig. 3.23 Normalized PE objective functions U_{PE} versus x for $\boldsymbol{R}^t = \boldsymbol{R}_f(x_c^*)$, varying $x = L$ from 1 mm to 12 mm, using frequency sweeps from 4 GHz to 6 GHz with 201 frequency points.

formulation has a better dynamic range than the other formulations. Moreover, the K-L formulation does not have local minima.

The PE objective functions versus x for Case 2, where $\boldsymbol{R}^t = \boldsymbol{R}_f(x_c^*)$, are shown in Fig. 3.22. The normalized objective functions are shown in Fig. 3.23, where it is also seen that the K-L formulation has a better dynamic range than the other formulations and it does not have local minima.

3.6.6 Numerical Comparison Using all the Previous PE Formulations

In this section, the parameter extraction numerical optimization is applied to the microstrip band-stop filter using all the PE objective function formulations described in Sections 2.3 and 2.4.

To have a better comparison between all the formulations, a scaled PE objective function U_{PE}^s is considered to make fair numerical comparisons and to apply equivalent termination criteria to stop the numerical optimization, as follows

$$U_{PE}^s = \frac{U_{PE}(\boldsymbol{x})}{U_{PE}(\boldsymbol{x}^{(0)})} \tag{3-6}$$

where $\boldsymbol{x}^{(0)} \in \Re^n$ is the starting point for numerical PE.

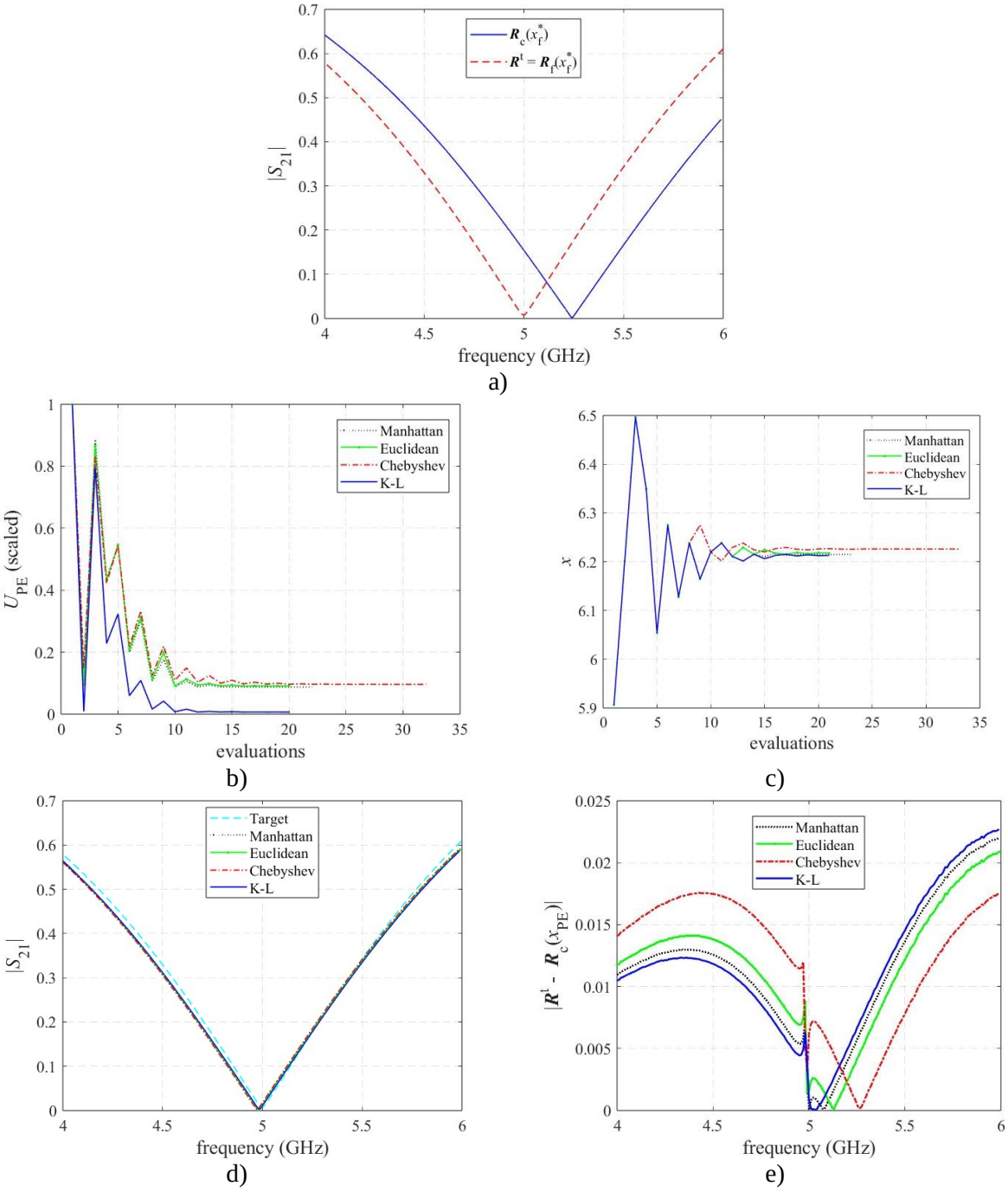

Fig. 3.24 Numerical PE for Case 1 with $x^{(0)} = x_f^* = 5.906$ mm: a) before PE; b) evolution of scaled U_{PE}, c) evolution of x, d) response matching, e) absolute matching error at each frequency.

All the examples shown in this section consider objective functions calculated with frequency sweeps from 4 GHz to 6 GHz with 201 frequency points. These numerical PE optimizations use the Nelder-Mead method [Nelder-65] available in Matlab. Here we also consider

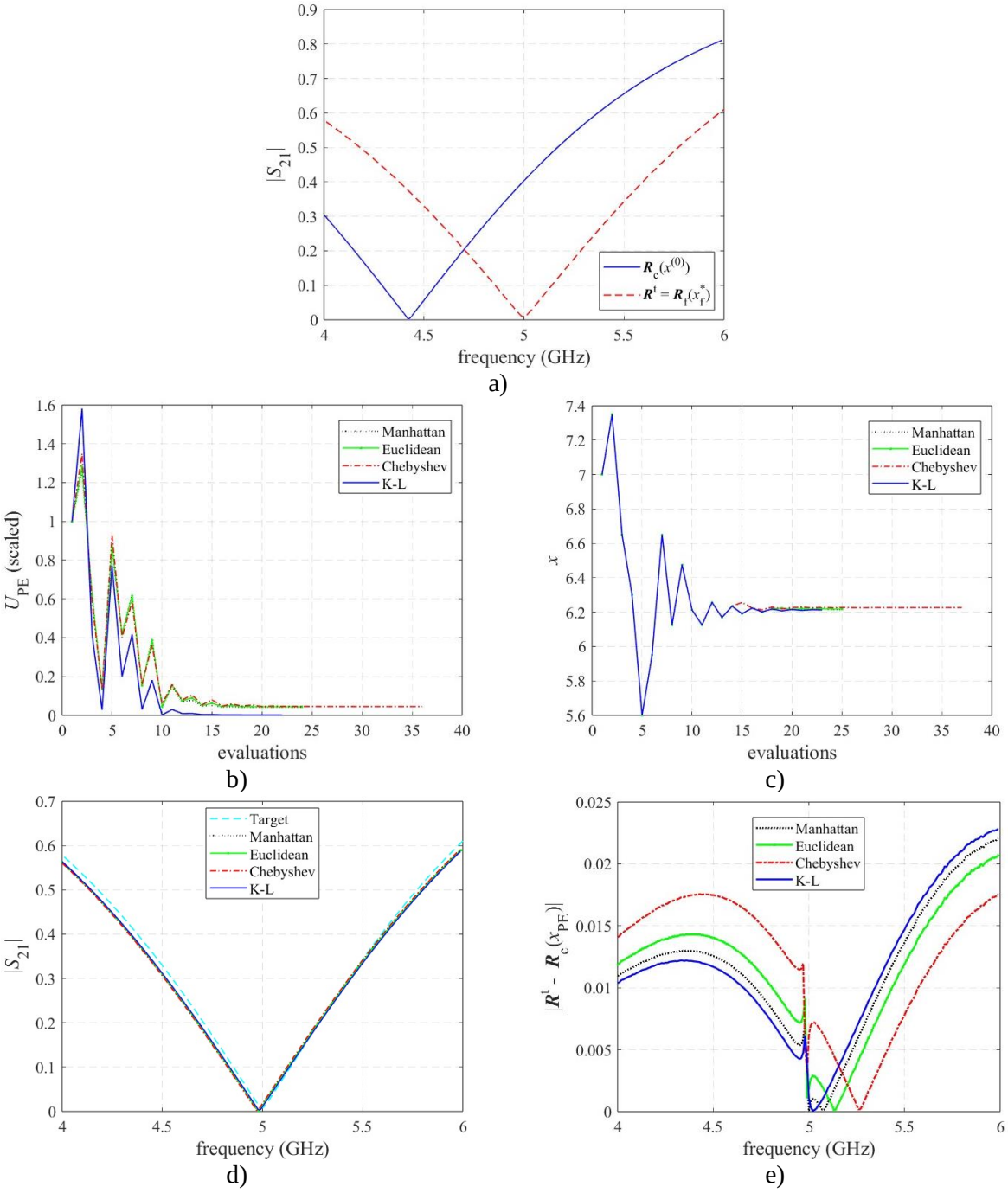

Fig. 3.25 Numerical PE for Case 1 with $x^{(0)}$ = 7.0 mm: a) before PE; b) evolution of scaled U_{PE}, c) evolution of x, d) response matching, e) absolute matching error at each frequency.

the same two PE cases mentioned in Sections 3.6.4.1 and 3.6.4.2: $\boldsymbol{R}^t = \boldsymbol{R}_f(x_f^*)$ and $\boldsymbol{R}^t = \boldsymbol{R}_f(x_c^*)$.

Two different values are considered as starting point $x^{(0)}$ for PE: the optimum fine model design (x_f^*) and an arbitrary value.

TABLE 3.2. TWO-DIMENTIONAL EXAMPLE SOLVED BY NUMERICAL PE USING THE NELDER-MEAD METHOD

$\boldsymbol{R}^t$	$\boldsymbol{x}^{(0)}$	Objective Function	U_s eval.	$\boldsymbol{x}^{PE}$	ε_{avg} (%)	ε_{max} (%)	ε_{nmse} (%)
Case 1 $\boldsymbol{R}^t = \boldsymbol{R}_f(\boldsymbol{x}_f^*)$	$\boldsymbol{x}^{(0)} = \boldsymbol{x}_f^* = L = 5.906$	Manhattan	22	6.214565	1.89	3.61	3.49
		Euclidean	20	6.217449	1.90	3.42	3.47
		Chebyshev	32	6.225956	0.34	2.88	3.62
		K-L	20	6.212835	1.90	3.72	3.53
	$\boldsymbol{x}^{(0)} = L = 7.0$	Manhattan	24	6.214551	1.89	3.61	3.49
		Euclidean	24	6.217969	1.90	3.39	3.47
		Chebyshev	36	6.225958	0.34	2.88	3.62
		K-L	22	6.212500	1.90	3.74	3.53
Case 2 $\boldsymbol{R}^t = \boldsymbol{R}_f(\boldsymbol{x}_c^*)$	$\boldsymbol{x}^{(0)} = \boldsymbol{x}_c^* = L = 6.1937$	Manhattan	18	6.511853	1.72	2.76	3.36
		Euclidean	20	6.514272	1.72	2.65	3.35
		Chebyshev	34	6.518053	0.28	2.48	3.38
		K-L	20	6.503385	1.77	3.17	3.56
	$\boldsymbol{x}^{(0)} = L = 7.0$	Manhattan	22	6.512598	1.72	2.73	3.36
		Euclidean	20	6.514648	1.73	2.64	3.35
		Chebyshev	34	6.518056	0.28	2.48	3.38
		K-L	18	6.502344	1.78	3.22	3.60

The numerical PE results for $\boldsymbol{R}^t = \boldsymbol{R}_f(x_f^*)$ with $x^{(0)} = x_f^*$ are shown in Fig. 3.24 for all the previous PE formulations. The coarse model response before PE, $\boldsymbol{R}_c(x^{(0)})$, and the target response $\boldsymbol{R}^t = \boldsymbol{R}_f(x_f^*)$ are shown in Fig. 3.24a. The evolution of the scaled objective function U_{PE}^s is shown in Fig. 3.24b. Fig. 3.24c shows the evolution of the design parameter x during optimization. Fig. 3.24d shows the target response matching of the coarse model response at the PE solution obtained by each formulation, $\boldsymbol{R}_c(x_{PE})$. Fig. 3.24e shows the absolute matching error at each frequency point for all the PE formulations. Similarly, Fig. 3.25 shows the numerical PE results for $\boldsymbol{R}^t = \boldsymbol{R}_f(x_f^*)$ with $\boldsymbol{x}^{(0)} = L = 7.0$ mm.

The numerical PE results for $\boldsymbol{R}^t = \boldsymbol{R}_f(x_c^*)$ with $x^{(0)} = \boldsymbol{x}_c^*$ ($L = 6.1937$ mm) and $\boldsymbol{x}^{(0)} = L = 7.0$ mm are shown in Fig. 3.26 and Fig. 3.27.

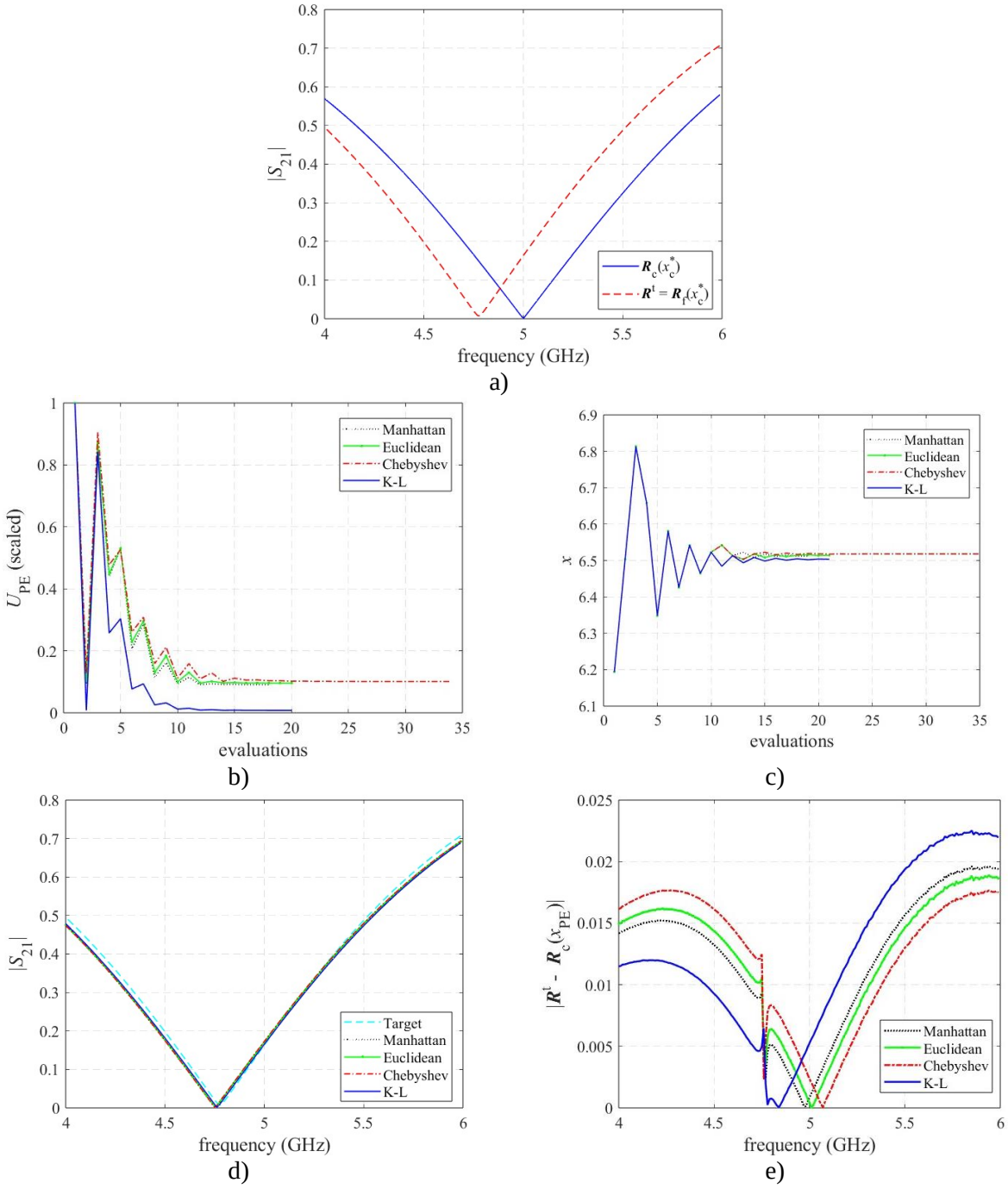

Fig. 3.26 Numerical PE for Case 2 with $x^{(0)} = x_c^* = 6.1937$ mm: a) before PE; b) evolution of scaled U_{PE}, c) evolution of x, d) response matching, e) absolute matching error at each frequency.

We can see from Fig. 3.24 - Fig. 3.27 that the matching quality for all the formulations is similar, and the number of coarse model evaluations to get the PE solution is similar or smaller with the K-L formulation. These results are summarized in Table 3.2.

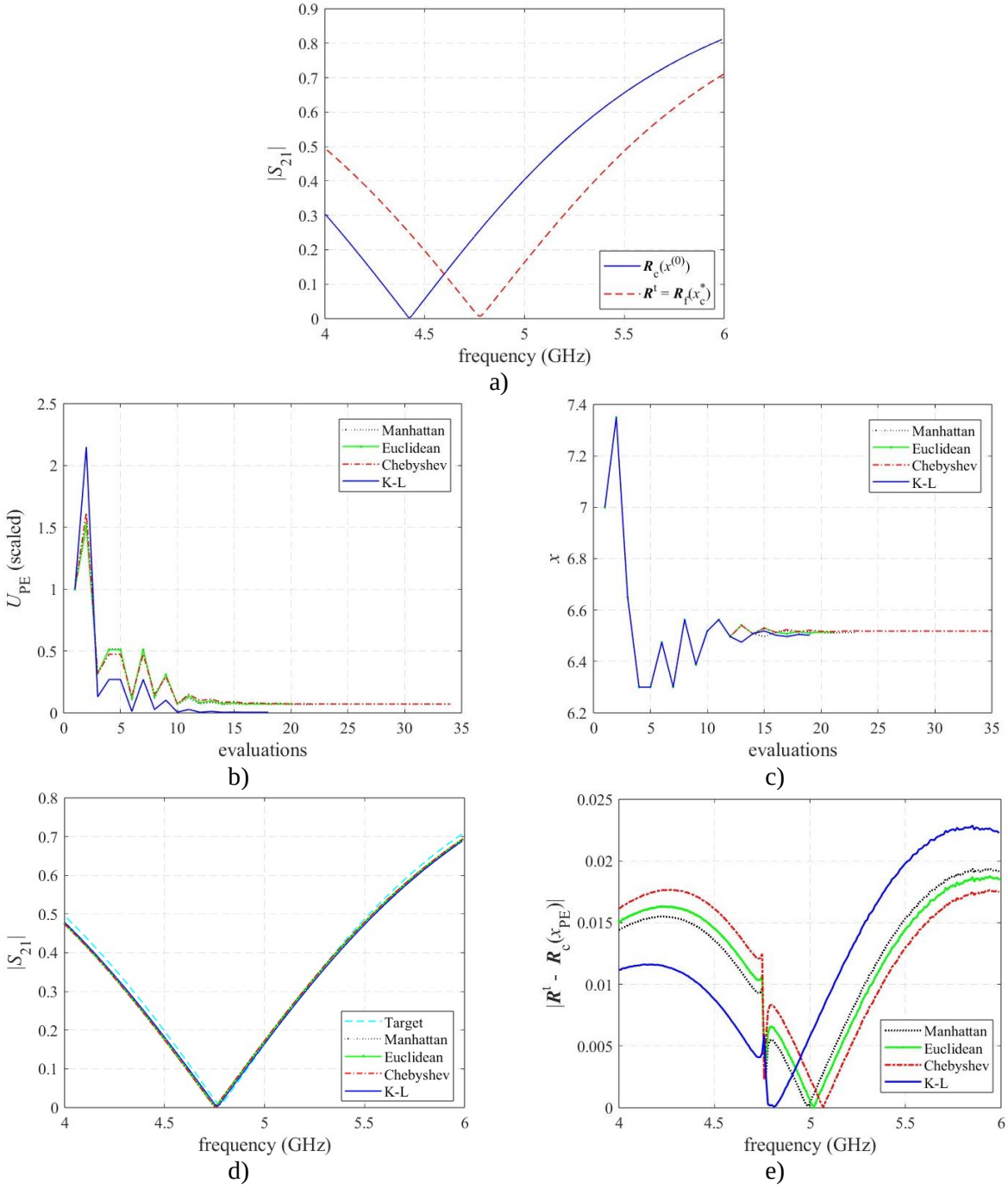

Fig. 3.27 Numerical PE for Case 2 with $x^{(0)} = L = 7.0$ mm: a) before PE; b) evolution of scaled U_{PE}, c) evolution of x, d) response matching, e) absolute matching error at each frequency.

The same figures of merit described in [Loera-Díaz-19b] are used in Table 3.2 to measure the corresponding matching errors between the l-th norms and the K-L formulation: average absolute relative error (ε_{avg}), normalized mean square error (*NMSE*), and maximum absolute

relative error ($\varepsilon_{\max}$), defined as

$$\varepsilon_{\text{avg}} = \frac{\frac{100}{r}\|\boldsymbol{e}_{\text{PE}}\|_1}{\|\boldsymbol{R}^{\text{t}}\|_\infty} \ (\%) \tag{3-7}$$

$$\varepsilon_{\max} = \frac{100\|\boldsymbol{e}_{\text{PE}}\|_\infty}{\|\boldsymbol{R}^{\text{t}}\|_\infty} \ (\%) \tag{3-8}$$

$$\varepsilon_{\text{nmse}} = \frac{100\|\boldsymbol{e}_{\text{PE}}\|_2}{\|\boldsymbol{R}^{\text{t}}\|_2} \ (\%) \tag{3-9}$$

where $\boldsymbol{e}_{\text{PE}}$ is the error vector after PE, $\boldsymbol{e}_{\text{PE}} = \boldsymbol{R}(x^{\text{PE}}) - \boldsymbol{R}^{\text{t}}$.

It is seen from Table 3.2 that errors produced for all the formulations are similar. However, the number of evaluations of the objective function (or the number of coarse model evaluations) to get the PE solution is smaller or similar for the K-L formulation.

3.7. Conclusion

In this chapter, a parameter extraction graphical study using Kullback-Leibler distance formulations as objective function was presented. It was confirmed in four different examples that the K-L distance PE formulation calculated with natural logarithm or 10-base logarithm yields equivalent results. It was also confirmed that the K-L formulation in "regular or direct order" can be severely affected (many local minima show up) when the responses are calculated using a relatively small number of points for the frequency sweep (or for the independent-variable). In the next chapter we will only use the K-L formulation with natural logarithm in "reverse order", since it yields softer objective functions with less local minima than the "direct order" K-L formulation.

This chapter also presented a graphical and numerical comparison of the Kullback-Leibler distance formulation as objective function for parameter extraction with the classical *l*-th norm formulations. This comparison was done using an EM validated single-stub band-stop filter in microstrip technology. Our results indicate that the promising behavior seen with previous synthetic examples of PE using the K-L formulation remains for this more realistic microwave example. PE using the K-L formulation exhibits similar or better PE performance than the traditional PE objective functions based on the *l*-th norms.

4. Space Mapping with Parameter Extraction Based on the K-L Distance Illustrated with Full-Wave EM and Equivalent Circuit Models

Space mapping (SM) techniques are commonly used for optimizing highly accurate models that require a large computational effort, known as fine models, by exploiting simplified physics-based models that are computationally fast but not accurate enough, known as coarse models. Most SM formulations require solving a parameter extraction (PE) sub-problem at each iteration. Typically, SM algorithms use classical *l*-th norms for the PE objective function. This chapter corresponds to a slightly modified version of our work in [Loera-Díaz-25c]. In this chapter, we first apply a PE formulation based on the Kullback-Leibler (K-L) distance to microstrip filters using their full-wave electromagnetic (EM) responses as targets, performing a rigorous numerical comparison against PE using classical norms. We subsequently propose, for the first time, a Broyden-based input space mapping algorithm using the K-L distance as objective function for the PE sub-problem. We apply SM design optimization to several examples, beginning with a classical synthetic test example and following with some microstrip filters using their full-wave EM representation as fine models, and their equivalent distributed circuit as coarse models. A rigorous numerical comparison is also performed between classical *l*-th norms and the K-L formulation for PE within the corresponding SM design optimizations. Our results indicate that SM with PE using the K-L formulation outperforms that one obtained by using the classical *l*-th norm PE formulations within SM.

4.1. Introduction

Space mapping (SM) techniques are used for the optimization of engineering models that are highly accurate but computationally expensive, named as fine models, with the support of physics-based auxiliary models that are fast but insufficiently accurate, named as coarse models [Koziel-08], [Cheng-08], [Rayas-Sánchez-21a]. Many space mapping algorithms [Bandler-04], [Rayas-Sánchez-25a] require solving a parameter extraction (PE) sub-problem at each SM

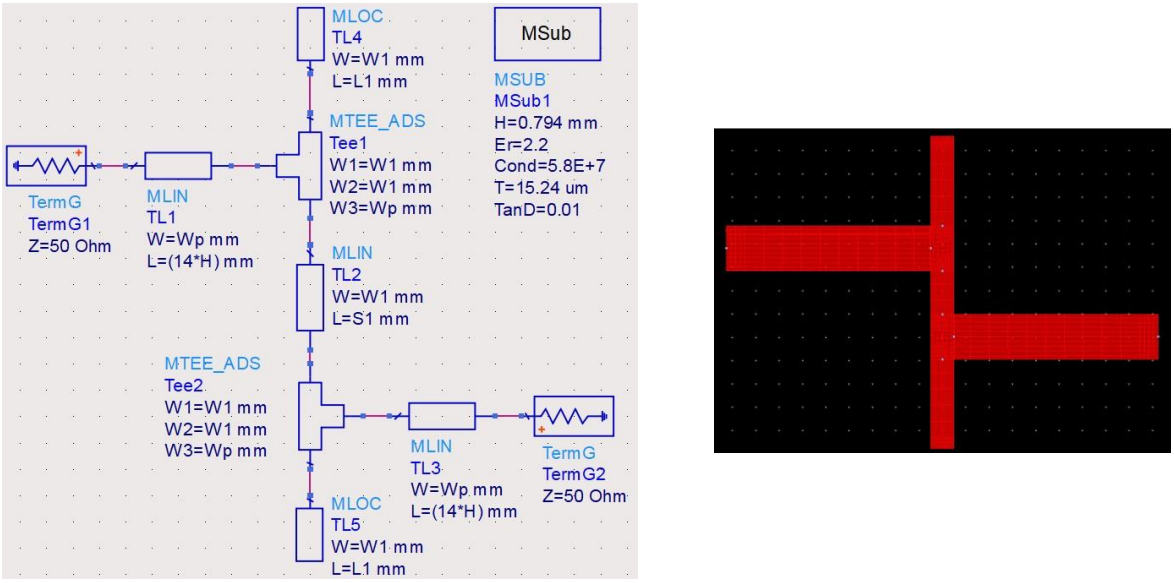

a) b)

Fig. 4.1 Low-pass filter in microstrip technology: a) coarse model in ADS, b) fine model in ADS Momentum. Images taken from [Loera-Díaz-25c].

iteration [Bandler-95], [Rayas-Sánchez-16], which consists of finding the coarse model parameters that make the coarse model response as close as possible to the fine model response at the current iterate. This PE sub-problem has a very important impact on the stability and convergence of space mapping algorithms [Bandler-04], [Rayas-Sánchez-25a], [Rayas-Sánchez-16], [Bandler-99]. Objective functions based on classical norms, also referred as *l*-th norms, have been traditionally employed to do PE [Bandler-23].

A very recent development for PE in the context of SM consists of translating conventional microwave responses (*e.g.*, |S21| evaluated over a broad frequency sweep) into a few problem-dependent key features based on engineering experience [Rayas-Sánchez-25b]. This approach has been recently adapted to formulate a cognitive SM technique [Rayas-Sánchez-25c]. However, in this chapter, we focus on the effects of applying different PE formulations on conventional microwave responses directly generated by commercially available high-frequency simulators.

On a totally different context, in the field of information theory, the Kullback-Leibler (K-L) distance formulation was developed [Kullback-51] as an approach inspired in Shannon entropy theory for measuring the "distance" or "divergence" in statistical populations. This formulation resulted in an efficient technique for measuring the difference between two probability distributions. It has been used in different fields and applications, *e.g.*, in speech synthesis to measure spectral distances [Veldhuis-03], in image processing for texture retrieval [Do-02], and

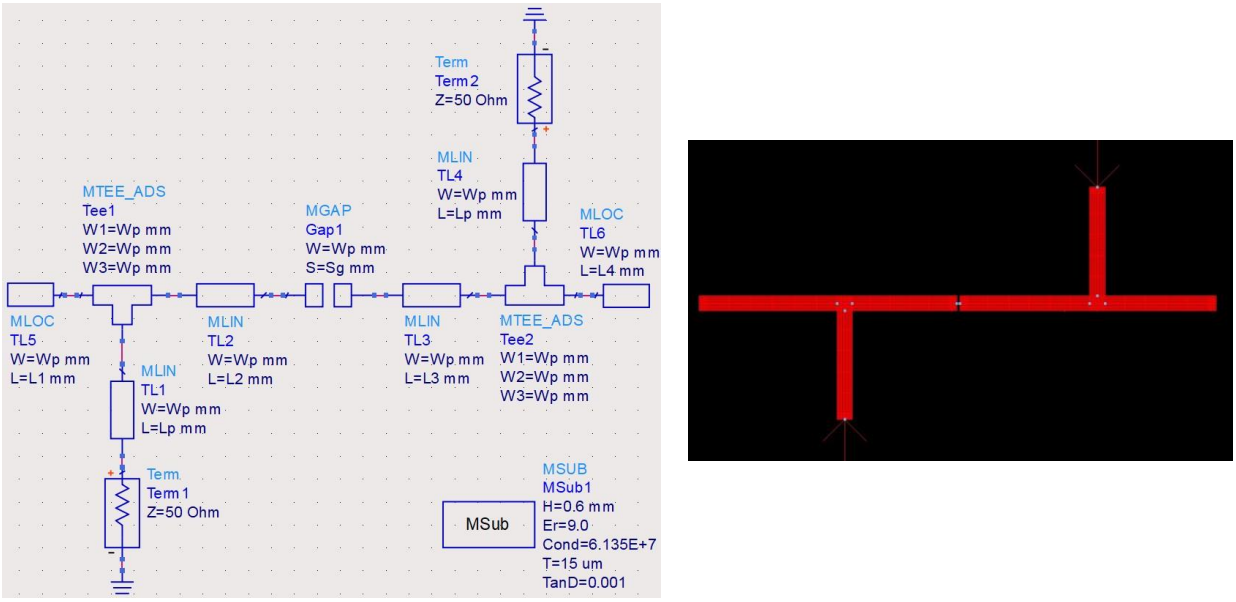

Fig. 4.2 Band-pass filter in microstrip technology: a) coarse model in ADS, b) fine model in ADS Momentum. Images taken from [Loera-Díaz-25c].

in gas sensors for odor discrimination [Vergara-09], among others. As confirmed in Section 4.3, the K-L formulation resulted in a very suitable objective function to extract the parameters of a circuit model to match a typical RF or microwave response used as a target, given its larger dynamic range and smoother contours, as demonstrated in [Loera-Díaz-20a].

An experimental formulation for PE in the context of SM was proposed in Chapter 2 [Loera-Díaz-20a] by exploiting the K-L distance to measure the local alignment between coarse and "fine" model responses, demonstrating a promising behavior of the resultant PE objective functions in some 1- and 2-dimensional synthetic examples [Loera-Díaz-20a]. It was observed that K-L formulations produce smoother PE objective functions with larger dynamic ranges as compared to those produced with classical *l*-th norms [Loera-Díaz-20a].

This chapter is based in our work in [Loera-Díaz-25c], where we first use the K-L distance formulation for PE, as defined in Chapter 2 [Loera-Díaz-20a], and apply it to microstrip filters whose target response is obtained from an accurate full-wave EM simulation, while the corresponding model responses are fast equivalent circuits in Keysight ADS [Loera-Díaz-25a], [Loera-Díaz-24b]. A rigorous numerical comparison of PE using the K-L formulation against PE using classical norms (Manhattan, Euclidean, and Chebyshev) is performed, confirming the advantages found in Chapter 2 [Loera-Díaz-20a]. In this expanded version of our work in [Loera-

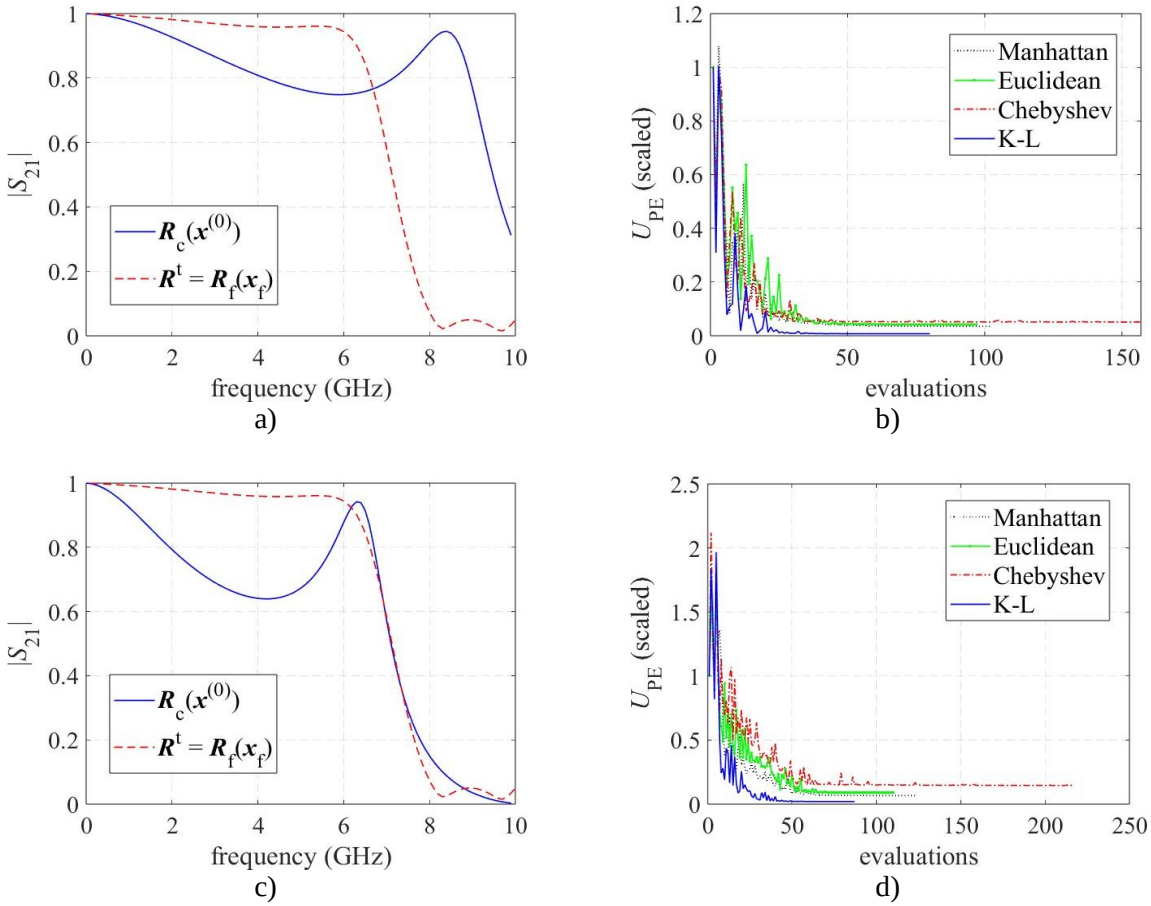

Fig. 4.3 PE results for the low-pass microstrip filter (see Fig. 1.12) using two different starting points $\boldsymbol{x}^{(0)}$ for the same target. a), c) EM response used as target $\boldsymbol{R}^t$ and initial coarse model response at the starting points, $\boldsymbol{R}_c(\boldsymbol{x}^{(0)})$; b), d) evolution of scaled U_{PE}. a) and b) use $\boldsymbol{x}^{(0)} = [4.0 \;\; 3.0 \;\; 2.0]^T$ mm (Case 1); c) and d) use $\boldsymbol{x}^{(0)} = [6.0 \;\; 4.0 \;\; 4.0]^T$ mm (Case 2). Images taken from [Loera-Díaz-25c].

Díaz-25a], we provide essential background on SM and make explicit the stopping criteria used in our SM examples for rigorous comparisons. We next propose, for the first time, a Broyden-based input SM algorithm [Rayas-Sánchez-16] that applies the K-L distance formulation in the PE sub-problem at each SM iteration. The proposed SM algorithm with K-L distance for PE is first applied to a classical synthetic example and then to several microstrip filters whose fine models use accurate full-wave EM models and the corresponding coarse models are equivalent circuits in Keysight ADS. We also perform a rigorous numerical comparison of this SM algorithm with PE using the K-L formulation against SM with classical norms for PE. We show that the proposed SM with K-L formulation for PE numerically outperforms the corresponding SM with classical *l*-th norms for the PE sub-problem.

The rest of the chapter is organized as follows. Section 4.2 revisits PE objective functions

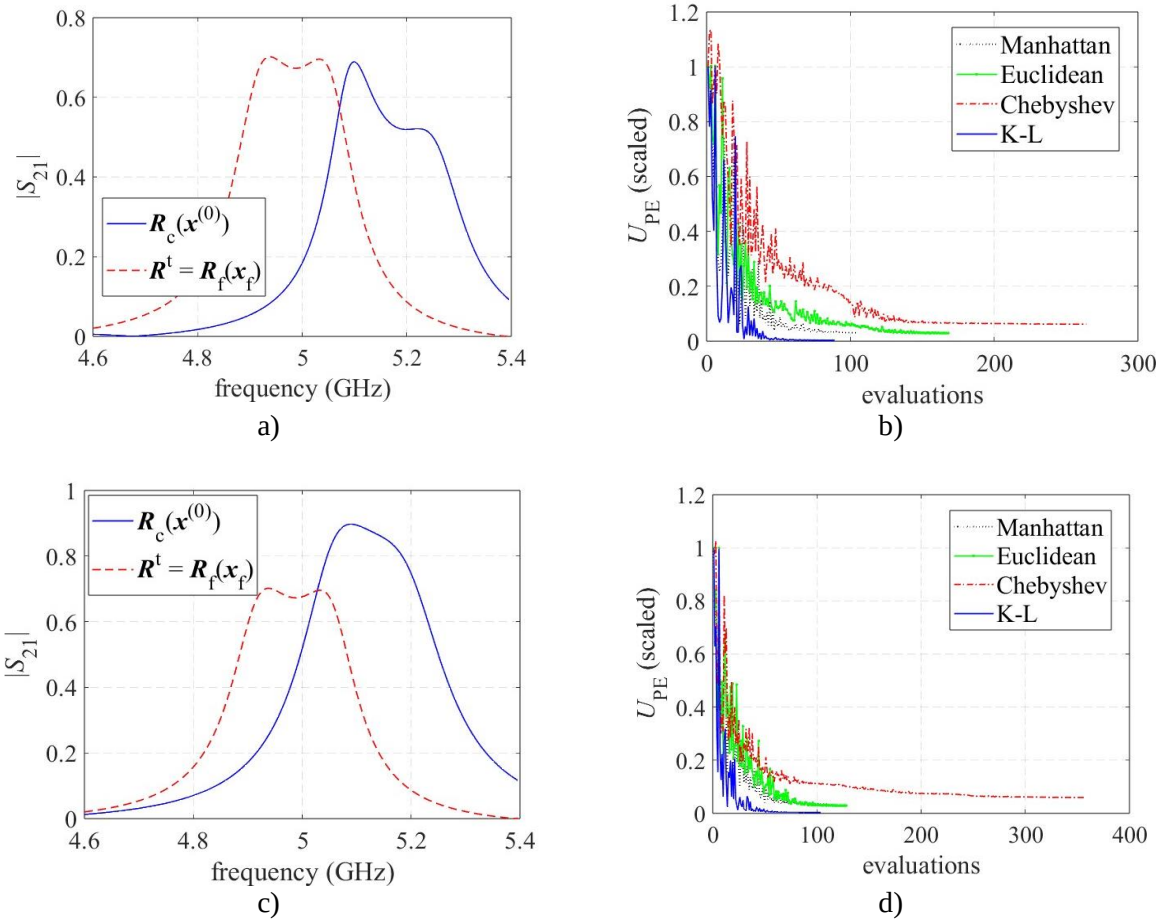

Fig. 4.4 PE results for the band-pass microstrip filter (see Fig. 1.35) using two different starting points $\boldsymbol{x}^{(0)}$ for the same target. a), c) EM filter response used as target $\boldsymbol{R}^{t}$ and initial coarse model response at the starting points, $\boldsymbol{R}_c(\boldsymbol{x}^{(0)})$; b), d) evolution of scaled U_{PE}. a) and b) use $\boldsymbol{x}^{(0)} = [6.2\ \ 4.6\ \ 5.9\ \ 5.1\ \ 0.15]^T$ mm (Case 1); c) and d) use $\boldsymbol{x}^{(0)} = [6.5\ \ 4.5\ \ 6.0\ \ 5.0\ \ 0.13]^T$ mm (Case 2). Images taken from [Loera-Díaz-25c].

and reintroduces the Kullback-Leibler distance for PE. Section 4.3 compares PE with classical *l*-th norms against PE with K-L formulation. Section 4.4 revisits Broyden-based input SM and defines the stopping criteria used for the numerical comparisons presented in Section 4.5. Finally, Section 4.6 concludes our work.

4.2. Parameter Extraction Objective Functions

Numerical parameter extraction can be formulated as the following optimization problem:

$$\boldsymbol{x}^{PE} = \arg\min_{\boldsymbol{x}} U_{PE}(\boldsymbol{R}(\boldsymbol{x}), \boldsymbol{R}^{t}) \tag{4-1}$$

TABLE 4.1. PE RESULTS FOR THE LOW-PASS FILTER USING THE NELDER-MEAD METHOD FOR EACH PE OBJECTIVE FUNCTION

$\boldsymbol{x}^{(0)}$	OF	i	$\boldsymbol{x}^{\mathrm{PE}}$	$\varepsilon_{\mathrm{avg}}^{\mathrm{PE}}$	$\varepsilon_{\mathrm{max}}^{\mathrm{PE}}$	$\varepsilon_{\mathrm{nms}}^{\mathrm{PE}}$
Case 1	Manhattan	102	$[1.3729 \quad 5.3993 \quad 2.8353]^{\mathrm{T}}$	0.93	5.40	2.10
	Euclidean	97	$[1.4973 \quad 5.3133 \quad 2.9794]^{\mathrm{T}}$	1.02	4.94	2.01
	Chebyshev	157	$[2.2123 \quad 4.9795 \quad 3.5190]^{\mathrm{T}}$	0.41	4.64	3.65
	K-L	80	$[1.5159 \quad 5.2744 \quad 3.1133]^{\mathrm{T}}$	1.06	4.95	2.06
Case 2	Manhattan	123	$[1.3722 \quad 5.3997 \quad 2.8358]^{\mathrm{T}}$	0.93	5.41	2.10
	Euclidean	110	$[1.4984 \quad 5.3126 \quad 2.9799]^{\mathrm{T}}$	1.03	4.94	2.01
	Chebyshev	216	$[2.2177 \quad 4.9768 \quad 3.5229]^{\mathrm{T}}$	0.41	4.64	3.67
	K-L	87	$[1.5157 \quad 5.2751 \quad 3.1106]^{\mathrm{T}}$	1.06	4.95	2.06

where the n model parameters are in vector $\boldsymbol{x} \in \Re^n$, the r model responses are represented by a multidimensional vector function $\boldsymbol{R}(\boldsymbol{x})$: $\Re^n \rightarrow \Re^r$, and vector $\boldsymbol{R}^{\mathrm{t}} \in \Re^r$ contains the target response for PE. The difference between $\boldsymbol{R}(\boldsymbol{x})$ and $\boldsymbol{R}^{\mathrm{t}}$ is measured by a multidimensional scalar PE objective function U_{PE}: $\Re^n \rightarrow \Re^1$. The purpose of PE, hopefully achieved by solving (4-1), is to find the optimal model parameters $\boldsymbol{x}^{\mathrm{PE}} \in \Re^n$ that make the model response $\boldsymbol{R}(\boldsymbol{x})$ as close as possible to the target response $\boldsymbol{R}^{\mathrm{t}}$. In the SM context, $\boldsymbol{R}^{\mathrm{t}}$ is obtained from the fine model, while $\boldsymbol{R}(\boldsymbol{x})$ is obtained from the coarse model.

The PE objective function using an l-th norm is

$$U_{\mathrm{PE}}(\boldsymbol{R}(\boldsymbol{x}), \boldsymbol{R}^{\mathrm{t}}) = \|\boldsymbol{e}(\boldsymbol{x})\|_l \tag{4-2}$$

where $\boldsymbol{e}(\boldsymbol{x}) \in \Re^n$ is the error of the model response with respect to the target response, $\boldsymbol{e}(\boldsymbol{x}) = \boldsymbol{R}(\boldsymbol{x}) - \boldsymbol{R}^{\mathrm{t}}$. The classical norms employed in (4-2) are Manhattan (l = 1), Euclidean (l = 2), and Chebyshev ($l \rightarrow \infty$) [Bandler-23], defined respectively as

$$U_{\mathrm{PE}}^{\mathrm{M}} = \sum_{j=1}^{r} \left| e_j(\boldsymbol{x}) \right| \tag{4-3}$$

$$U_{\mathrm{PE}}^{\mathrm{E}} = \left(\sum_{i=1}^{r} e_j^2(\boldsymbol{x}) \right)^{\frac{1}{2}} \tag{4-4}$$

$$U_{\mathrm{PE}}^{\mathrm{C}} = \max_j \left\{ \cdots \left| e_j(\boldsymbol{x}) \right| \cdots \right\} \tag{4-5}$$

Following [Loera-Díaz-20a], the difference between two general systems, A and B, can be represented by relative entropy [Zhao-05] according to Shannon information theory [McEliece-01]. This difference measured by the Kullback-Leibler (K-L) distance [Kullback-51] is given by

TABLE 4.2. PE RESULTS FOR THE BAND-PASS FILTER USING THE NELDER-MEAD METHOD FOR EACH PE OBJECTIVE FUNCTION

$\boldsymbol{x}^{(0)}$	OF	i	$\boldsymbol{x}^{\mathrm{PE}}$	$\varepsilon_{\mathrm{avg}}^{\mathrm{PE}}$	$\varepsilon_{\mathrm{max}}^{\mathrm{PE}}$	$\varepsilon_{\mathrm{nms}}^{\mathrm{PE}}$
Case 1	Manhattan	105	[6.6199 4.7714 5.8767 5.3965 0.1338]T	1.23	4.27	3.06
	Euclidean	168	[6.6440 4.7414 5.8708 5.4011 0.1300]T	1.24	2.58	2.77
	Chebyshev	264	[6.3725 4.9211 6.2208 5.2004 0.1386]T	0.16	5.49	6.82
	K-L	89	[6.6094 4.7837 5.8934 5.3795 0.1380]T	1.56	7.92	4.57
Case 2	Manhattan	110	[6.6489 4.7292 5.8664 5.4033 0.1237]T	1.32	2.8	2.86
	Euclidean	128	[6.6553 4.7236 5.8654 5.4040 0.1242]T	1.32	2.43	2.83
	Chebyshev	358	[6.3755 4.9193 6.2568 5.1737 0.1375]T	0.14	5.94	7.63
	K-L	104	[6.6215 4.7509 5.8855 5.3873 0.1246]T	1.53	6.11	4.31

(2-6) [Zhao-05], [Matsuoka-91], and reproduced here for convenience

$$C = \sum_{j=1}^{r} \left\{ A_j \ln \left| \frac{A_j}{B_j} \right| + (1 - A_j) \ln \left| \frac{1-A_j}{1-B_j} \right| \right\} \tag{4-6}$$

where C is the relative entropy between systems A and B, and A_j and B_j (j = 1, 2, … , r) are the j-th states of these systems. Adapting (4-6) to the PE objective function $U_{\mathrm{PE}}(\boldsymbol{R}(\boldsymbol{x}), \boldsymbol{R}^{\mathrm{t}})$,

$$U_{\mathrm{PE}}^{\mathrm{KL}} = \sum_{j=1}^{r} \left\{ R_j(\boldsymbol{x}) \ln \left| \frac{R_j(\boldsymbol{x})}{R_j^{\mathrm{t}}} \right| + (1 - R_j(\boldsymbol{x})) \ln \left| \frac{1-R_j(\boldsymbol{x})}{1-R_j^{\mathrm{t}}} \right| \right\} \tag{4-7}$$

where R_j is the j-th model response at model parameters $\boldsymbol{x}$, and Rj^{t} is the j-th target response [Loera-Díaz-20a] (see Section 2.4).

Since the PE objective function values using the above formulations significantly differ from each other, the following scaled PE objective function $U_{\mathrm{PE}}^{\mathrm{S}}$ is used to make fair numerical comparisons and to apply the same termination criteria to stop the numerical optimization during PE,

$$U_{\mathrm{PE}}^{\mathrm{S}} = \frac{U_{\mathrm{PE}}(\boldsymbol{x})}{U_{\mathrm{PE}}(\boldsymbol{x}^{(0)})} \tag{4-8}$$

where $\boldsymbol{x}^{(0)} \in \Re^n$ is the starting point for numerical PE.

Considering that (4-6) has been employed to measure the difference between probabilistic distributions, then (4-7) could be useful to do PE not only for deterministic responses but also for model responses with statistical fluctuations. That potential property of K-L-based PE can be studied in a future contribution considering statistical manufacturing tolerances in the model

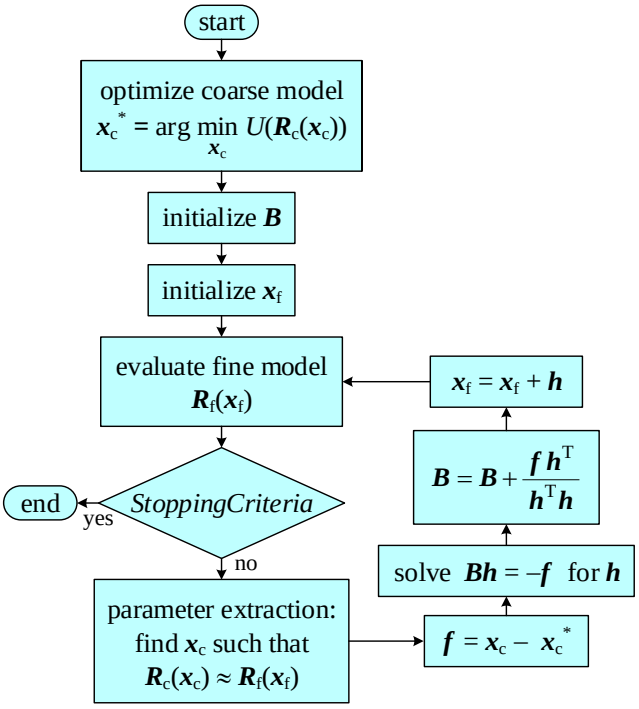

Fig. 4.5 Broyden-based input SM algorithm. Image taken from [Rayas-Sánchez-16].

parameters (beyond the scope of this work).

4.3. PE Using Classical Norms and K-L

A low-pass and a band-pass microstrip filters are used in this section to compare the behavior of the PE sub-problem with classical *l*-th norm versus the K-L formulation.

4.3.1 PE Example 1: Low-Pass Microstrip Filter

As a first PE example we use the microstrip low-pass filter shown in Fig. 1.12 [Sheen-90]. It has a substrate with a relative dielectric permittivity $\varepsilon_r = 2.2$, height $H = 0.794$ mm, and loss tangent $\tan(\delta) = 0.01$. Metal traces and ground plane use copper with thickness $t = 15.24$ μm and conductivity $\sigma = 5.8\times10^7$ S/m. The input-output 50-Ω microstrip lines have a width $W_p = 2.45$ mm and a length $L_p = 14H$. They are separated by a distance S_1 with a microstrip line width W_1 and open stubs with length L_1. This filter has three design parameters $\boldsymbol{x} = [W_1 \quad L_1 \quad S_1]^T$. The pre-assigned parameters are $\boldsymbol{z} = [H \;\; \varepsilon_r \;\; W_p \;\; L_p \;\; \tan(\delta) \;\; \sigma \;\; t]^T$.

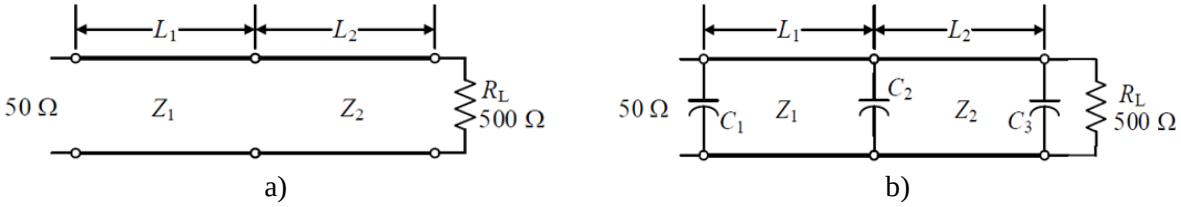

Fig. 4.6 Two-section impedance transformer [Pozar-98]: a) coarse model, b) fine model [Loera-Díaz-20a]. The design parameters are $\boldsymbol{x} = [L_1 \quad L_2]^T$ [Loera-Díaz-25c].

The coarse model is the Keysight ADS equivalent circuit shown in Fig. 4.1a. The full-wave EM fine model is in Keysight ADS Momentum Microwave, as shown in Fig. 4.1b, using a high-resolution discretization until EM resolution convergence is reached.

4.3.2 PE Example 2: Band-Pass Microstrip Filter

As a second PE example we use the microstrip band-pass filter shown in Fig. 1.35

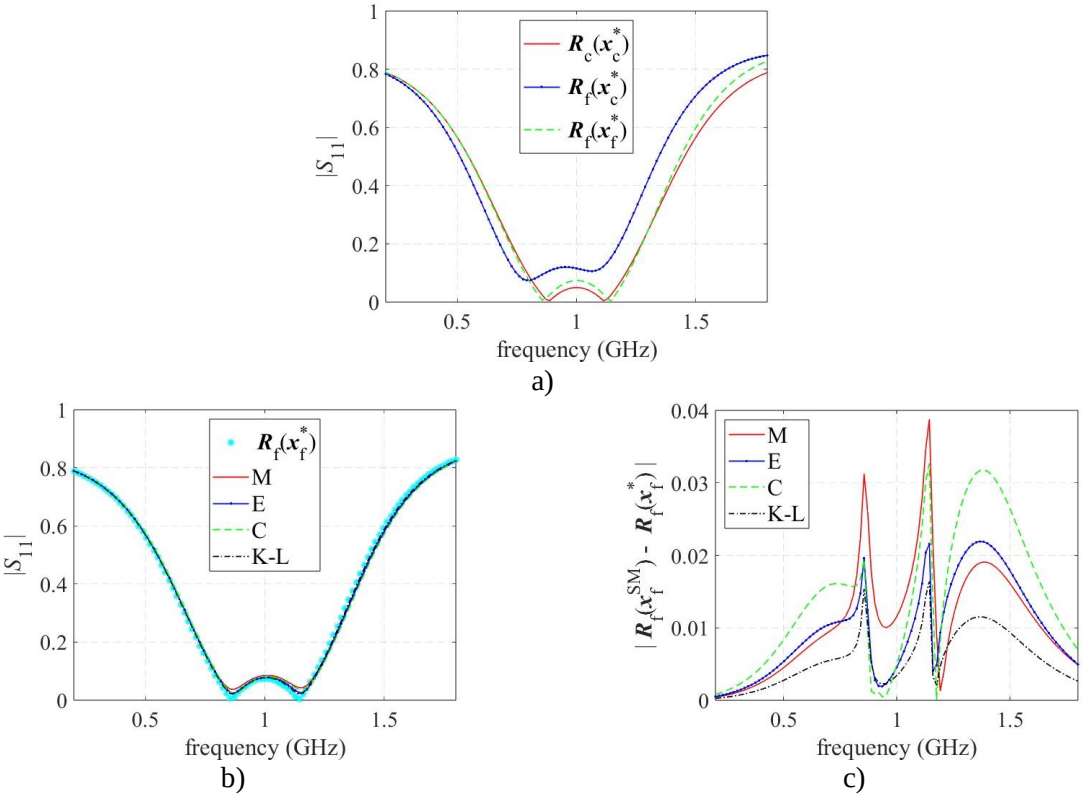

Fig. 4.7 SM results for the two-section impedance transformer. a) $\boldsymbol{R}_c(\boldsymbol{x}_c^*)$, $\boldsymbol{R}_f(\boldsymbol{x}_c^*)$, and $\boldsymbol{R}_f(\boldsymbol{x}_f^*)$; b) $\boldsymbol{R}_f(\boldsymbol{x}_f^{SM})$ using Manhattan (M), Euclidean (E), Chebyshev (C), and Kullback-Leibler (K-L) for PE, versus $\boldsymbol{R}_f(\boldsymbol{x}_f^*)$; c) corresponding matching error $|\boldsymbol{R}_f(\boldsymbol{x}_f^{SM}) - \boldsymbol{R}_f(\boldsymbol{x}_f^*)|$. Images taken from [Loera-Díaz-25c].

TABLE 4.3. SM RESULTS FOR THE TWO-SECTION IMPEDANCE TRANSFORMER USING DIFFERENT OBJECTIVE FUNCTIONS FOR PE

OF	$\boldsymbol{x}_c^{(i)T}$	$\boldsymbol{x}_f^{(i)T}$	$N_c^{(i)}$	N_c^t	ε_{avg}^{SM}	ε_{max}^{SM}	ε_{nms}^{SM}	SC
M	[101.93 92.06] [91.34 88.25]	[90.00 90.00] [78.07 87.94] [76.60 89.85]	69 83	152	1.33	4.68	2.67	2
E	[102.10 92.51] [90.64 88.55]	[90.00 90.00] [77.90 87.49] [77.24 88.98]	65 71	136	1.20	2.65	2.37	2
C	[102.00 94.24] [88.54 89.66]	[90.00 90.00] [78.00 85.76] [79.31 86.06]	97 88	185	1.69	3.95	3.37	2
K-L	[102.19 92.41] [90.04 88.39]	[90.00 90.00] [77.81 87.59] [77.77 89.17]	64 68	132	0.68	1.98	1.35	2

[Hennings-06]. The dielectric substrate uses alumina with $\varepsilon_r = 9$, $H = 0.6$ mm, and $\tan(\delta) = 0.001$. All microstrip lines used in this filter have the same width $W_p = 0.7$ mm. The feeding microstrip lines have a length $L_p = 5$ mm. Metallic strips and ground plane use $t = 15$ μm and $\sigma = 5.8\times10^7$ S/m. Main resonators have lengths L_1, L_2, L_3, and L_4, with a separating gap S_g. This band-pass filter has five design parameters $\boldsymbol{x} = [L_1 \;\; L_2 \;\; L_3 \;\; L_4 \;\; S_g]^T$ and seven pre-assigned parameters $\boldsymbol{z} = [H \;\; \varepsilon_r \;\; W_p \;\; \tan(\delta) \;\; \sigma \;\; t]^T$.

The coarse model is the Keysight ADS equivalent circuit shown in Fig. 4.2a. The corresponding full-wave EM fine model is in Keysight ADS Momentum Microwave, as shown in Fig. 4.2b, also using a fine resolution grid until resolution convergence is reached.

4.3.3 PE Results and Numerical Comparison

The following error metrics are used for numerical comparison between all the PE formulations: the average absolute relative error (ε_{avg}^{PE}), the maximum absolute relative error (ε_{max}^{PE}), and the normalized mean square error (ε_{nms}^{PE}), defined as

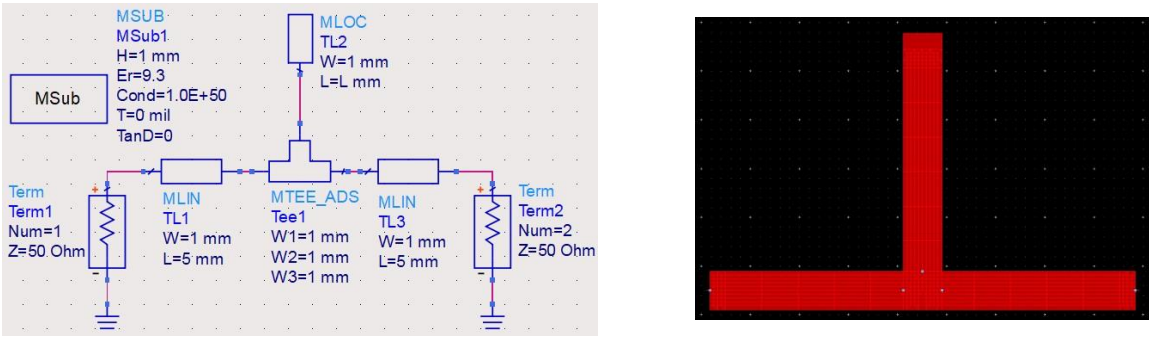

a) b)

Fig. 4.8 Single-stub band-stop filter in microstrip technology: a) coarse model in ADS, b) fine model in ADS Momentum. Images taken from [Loera-Díaz-25c].

$$\varepsilon_{\text{avg}}^{\text{PE}} = \frac{\frac{100}{r}\|\boldsymbol{e}_{\text{PE}}\|_1}{\|\boldsymbol{R}^{\text{t}}\|_\infty} \ (\%) \tag{4-9}$$

$$\varepsilon_{\text{max}}^{\text{PE}} = \frac{100\|\boldsymbol{e}_{\text{PE}}\|_\infty}{\|\boldsymbol{R}^{\text{t}}\|_\infty} \ (\%) \tag{4-10}$$

$$\varepsilon_{\text{nms}}^{\text{PE}} = \frac{100\|\boldsymbol{e}_{\text{PE}}\|_2}{\|\boldsymbol{R}^{\text{t}}\|_2} \ (\%) \tag{4-11}$$

where $\boldsymbol{e}^{\text{PE}}$ is the error vector after PE, $\boldsymbol{e}_{\text{PE}} = \boldsymbol{R}(\boldsymbol{x}^{\text{PE}}) - \boldsymbol{R}^{\text{t}}$.

The target fine model response $\boldsymbol{R}^{\text{t}}$ for PE is obtained from the EM simulation at reference design $\boldsymbol{x}_{\text{f}} = [1.270 \ \ 4.880 \ \ 2.365]^{\text{T}}$ (mm) for the low-pass filter, and $\boldsymbol{x}_{\text{f}} = [6.275 \ \ 4.75 \ \ 5.90 \ \ 5.05 \ \ 0.15]^{\text{T}}$ (mm) for the band-pass filter. We consider two arbitrary starting points $\boldsymbol{x}^{(0)}$ for PE for each filter. The results are shown in Fig. 4.3 and Table 4.1 for the low-pass filter, and in Fig. 4.4 and Table 4.2 for the band-pass filter. In both examples we use the same optimization method (Nelder-Mead) [Nelder-65] with the same termination criteria for PE: tolerances employed for optimization variables (Δx) and objective function ($\Delta U_{\text{PE}}^{\text{S}}$) are as in [Loera-Díaz-25c].

It is seen from Fig. 4.3 and Fig. 4.4 that, for both examples and both starting points, the K-L formulation requires less evaluations of the PE objective function than those needed by *l*-th norms, arriving to a smaller value of the scaled PE objective function. Table 4.1 and Table 4.2 reconfirm those results and additionally indicate that K-L yields similar response matching errors than those obtained with *l*-th norms.

4.4. SM Algorithm

The Broyden-based input SM algorithm, also known as aggressive space mapping (ASM),

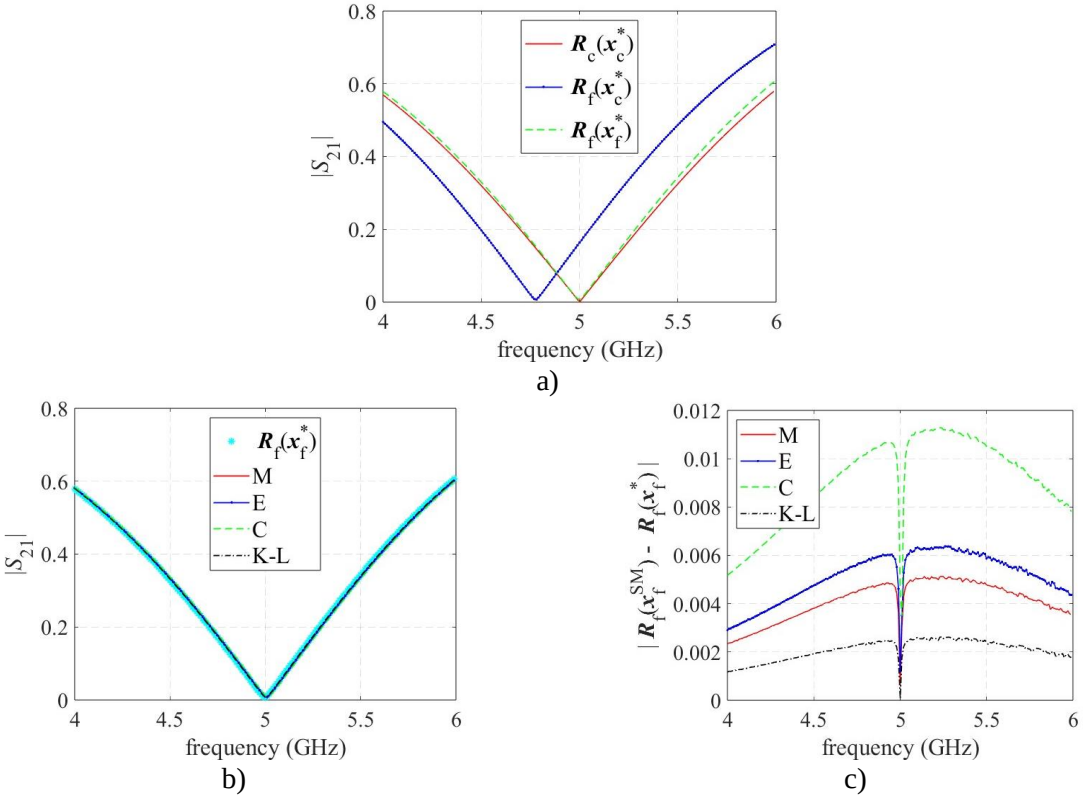

Fig. 4.9 SM results for the single-stub band-stop microstrip filter (see Fig. 1.2). a) $\boldsymbol{R}_c(\boldsymbol{x}_c^*)$, $\boldsymbol{R}_f(\boldsymbol{x}_c^*)$, and $\boldsymbol{R}_f(\boldsymbol{x}_f^*)$; b) $\boldsymbol{R}_f(\boldsymbol{x}_f^{SM})$ using Manhattan (M), Euclidean (E), Chebyshev (C), and Kullback-Leibler (K-L) for PE, versus $\boldsymbol{R}_f(\boldsymbol{x}_f^*)$; c) corresponding matching error $|\boldsymbol{R}_f(\boldsymbol{x}_f^{SM}) - \boldsymbol{R}_f(\boldsymbol{x}_f^*)$. Images taken from [Loera-Díaz-25c].

is shown in Fig. 4.5. First, the optimal coarse model design $\boldsymbol{x}_c^*$ is obtained [Bandler-95] by finding the ideal response that optimally satisfies the design specifications, $\boldsymbol{R}_c(\boldsymbol{x}_c^*)$. Next, the Broyden matrix $\boldsymbol{B}$ is initialized, normally with the identity matrix [Rayas-Sánchez-16]. Initially, the fine model response is evaluated at $\boldsymbol{x}_c^*$. If the stop criteria are not satisfied, then the PE sub-problem is solved to align the coarse model response $\boldsymbol{R}_c(\boldsymbol{x}_c)$ to the current fine model response $\boldsymbol{R}_f(\boldsymbol{x}_f)$. The difference $\boldsymbol{f}$ between the extracted parameters $\boldsymbol{x}_c$ and the optimal coarse model design $\boldsymbol{x}_c^*$ is calculated. Next, a quasi-Newton step $\boldsymbol{h}$ is calculated, $\boldsymbol{B}$ is updated using Broyden's formula, and the next iterate $\boldsymbol{x}_f$ is obtained where the new $\boldsymbol{R}_f(\boldsymbol{x}_f)$ is evaluated (see Fig. 4.5). This loop continues until the stopping criteria are satisfied, ending with a space-mapped solution $\boldsymbol{x}_f^{SM}$ [Rayas-Sánchez-16].

For the PE sub-problem in ASM, here we solve (4-1) by using as target the fine model response at the i-th iteration, $\boldsymbol{R}_f(\boldsymbol{x}_f^{(i)})$, to extract the coarse model parameters $\boldsymbol{x}_c^{PE}$, that achieve the local alignment $\boldsymbol{R}_c(\boldsymbol{x}_c^{PE}) \approx \boldsymbol{R}_f(\boldsymbol{x}_f^{(i)})$. This is done by using the four PE objective functions described

TABLE 4.4. SM RESULTS FOR THE BAND-STOP FILTER USING DIFFERENT OBJECTIVE FUNCTIONS FOR PE

OF	$\boldsymbol{x}_c^{(i)}$	$\boldsymbol{x}_f^{(i)}$	$N_c^{(i)}$	N_c^t	ε_{avg}^{SM}	ε_{max}^{SM}	ε_{nms}^{SM}	SC
	6.4985	6.1937	20					
M	6.1850	5.8889	20	40	6.89×10^{-11}	8.57×10^{-11}	8.37×10^{-11}	1&3
		5.8973						
	6.5010	6.1937	18					
E	6.1848	5.8864	20	38	8.57×10^{-11}	1.06×10^{-10}	1.04×10^{-10}	1&3
		5.8951						
	6.5045	6.1937	28					
C	6.1899	5.8829	34	62	1.52×10^{-10}	1.88×10^{-10}	1.85×10^{-10}	1&3
		5.8867						
	6.4889	6.1937	16					
K-L	6.1906	5.8985	20	36	3.48×10^{-11}	4.37×10^{-11}	4.23×10^{-11}	1&3
		5.9016						

in Section 4.2 Then, we compare the behavior of ASM obtained with classical norms (4-3)-(4-5) for PE versus that one obtained with the K-L formulation (4-7) used in the PE sub-problem.

The final goal of ASM is to find a space-mapped solution that makes the fine model response sufficiently close to the optimal coarse model response, $\boldsymbol{R}_f(\boldsymbol{x}_f^{SM}) \approx \boldsymbol{R}_c(\boldsymbol{x}_c^*)$.

Here, the stopping criteria (SC) used for ASM are [Rayas-Sánchez-16]:

$$\left\| \boldsymbol{f}(\boldsymbol{x}_f^{(i)}) \right\|_\infty < \varepsilon_1 \quad \vee \quad \ldots \tag{4-12a}$$

$$\left\| \boldsymbol{R}_f\left(\boldsymbol{x}_f^{(i)}\right) - \boldsymbol{R}_c(\boldsymbol{x}_c^*) \right\|_\infty \leq \varepsilon_2(\varepsilon_2 + \|\boldsymbol{R}_c(\boldsymbol{x}_c^*)\|_\infty) \quad \vee \quad \ldots \tag{4-12b}$$

$$\left\| \boldsymbol{x}_f^{(i+1)} - \boldsymbol{x}_f^{(i)} \right\|_2 \leq \varepsilon_3(\varepsilon_3 + \|\boldsymbol{x}_f^*\|_2) \quad \vee \quad \ldots \tag{4-12c}$$

$$i > i_{max} \tag{4-12d}$$

where ε_1, ε_2 and ε_3 are arbitrary small positive scalars. Typically i_{max} is $3n$ or $4n$ ($\boldsymbol{x}_f \in \Re^n$) [Rayas-Sánchez-16].

4.5. SM Using Classical Norms and K-L for PE

The Broyden-based input SM algorithm with classical *l*-th norms and with the K-L distance for PE [Loera-Díaz-20b], [Loera-Díaz-25b] is implemented in this section and applied to several

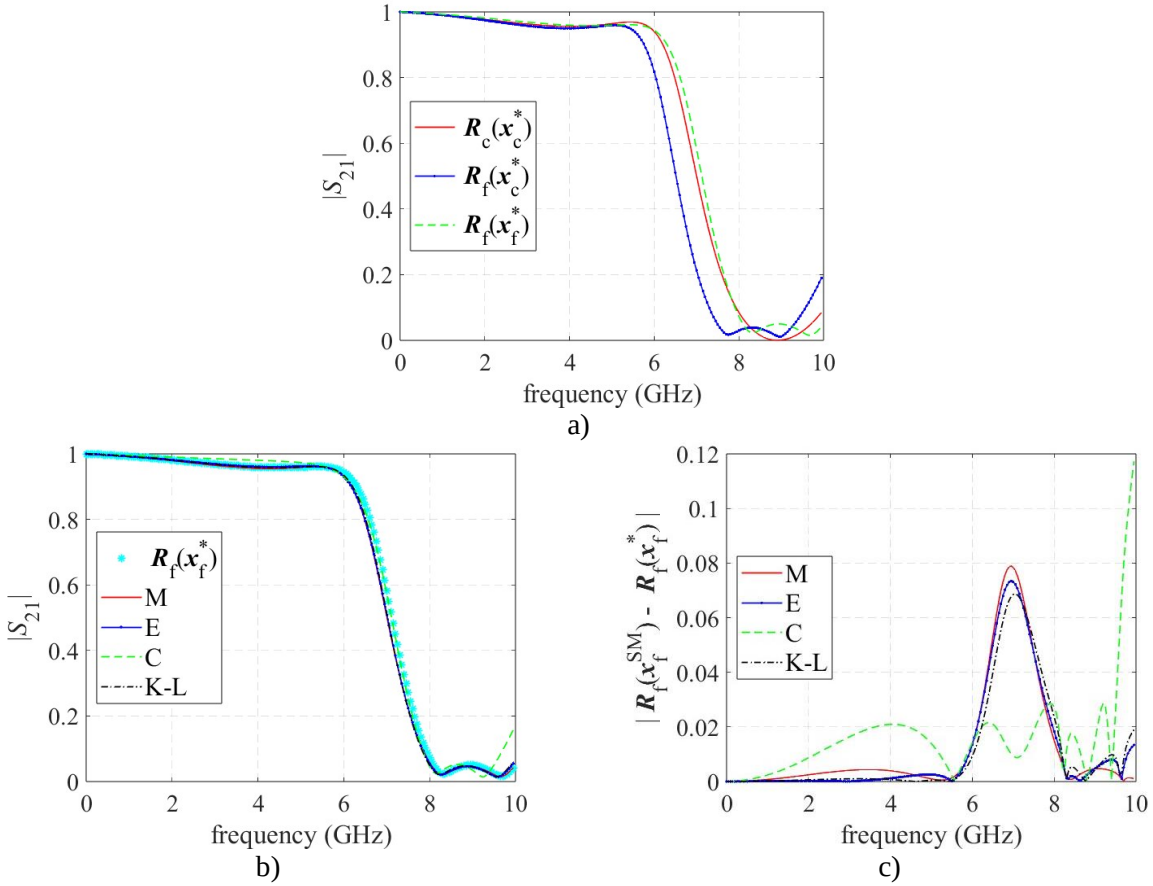

Fig. 4.10 SM results for the low-pass microstrip filter (see Fig. 1.12). a) $\boldsymbol{R}_c(\boldsymbol{x}_c^*)$, $\boldsymbol{R}_f(\boldsymbol{x}_c^*)$, and $\boldsymbol{R}_f(\boldsymbol{x}_f^*)$; b) $\boldsymbol{R}_f(\boldsymbol{x}_f^{SM})$ using Manhattan (M), Euclidean (E), Chebyshev (C), and Kullback-Leibler (K-L) for PE, versus $\boldsymbol{R}_f(\boldsymbol{x}_f^*)$; c) corresponding matching error $|\boldsymbol{R}_f(\boldsymbol{x}_f^{SM}) - \boldsymbol{R}_f(\boldsymbol{x}_f^*)$. Images taken from [Loera-Díaz-25c].

design optimization examples. The corresponding numerical results, including the $\boldsymbol{x}_f^{SM}$ found for each case, are rigorously compared. First, we apply SM to a classical synthetic test example (a two-section impedance transformer). Next, we apply it to three microstrip filters (band-stop, low-pass, and band-pass, respectively) whose fine models are accurate full-wave EM models, and their equivalent circuits are taken as coarse models.

4.5.1 SM Example 1: Classical Synthetic Test Example

As a first SM example, consider a classical synthetic test case: a capacitively-loaded 10:1 two-section impedance transformer. Ideal transmission lines are used in the coarse model, while capacitively-loaded transmission lines are used in the fine model, as shown in Fig. 4.6 [Pozar-98],

TABLE 4.5. SM RESULTS FOR THE LOW-PASS FILTER USING DIFFERENT OBJECTIVE FUNCTIONS FOR PE

OF	$\boldsymbol{x}_c^{(i)T}$	$\boldsymbol{x}_f^{(i)T}$	$N_c^{(i)}$	N_c^t	ε_{avg}^{SM}	ε_{max}^{SM}	ε_{nms}^{SM}	SC
M	[1.71 5.60 3.74] [1.39 5.41 2.83]	[1.52 5.27 3.11] [1.32 4.95 2.49] [1.41 4.85 2.70]	73 91	164	1.21×10^{-10}	7.93×10^{-10}	4.20×10^{-10}	3
E	[1.79 5.60 3.72] [1.45 5.32 3.01]	[1.52 5.27 3.11] [1.24 4.95 2.51] [1.30 4.92 2.60]	70 61	131	1.14×10^{-10}	7.38×10^{-10}	4.02×10^{-10}	3
C	[2.24 5.42 4.02] [1.62 5.09 3.33]	[1.52 5.27 3.11] [0.79 5.13 2.21] [0.66 5.35 1.94]	151 119	270	1.61×10^{-10}	1.18×10^{-09}	4.14×10^{-10}	3
K-L	[1.76 5.59 3.79] [1.49 5.29 3.06]	[1.52 5.27 3.11] [1.28 4.96 2.44] [1.30 4.94 2.49]	65 45	110	1.10×10^{-10}	6.90×10^{-10}	3.84×10^{-10}	1&3

[Loera-Díaz-20a].

The design parameters are $\boldsymbol{x} = [L_1 \ L_2]^T$ (degrees), with $C_1 = 0.4$ pF, $C_2 = 0.2$ pF and $C_3 = 0.1$ pF. The reference impedance for both models is $Z_0 = 50\ \Omega$ and the load impedance is $R_L = 500\ \Omega$. The transmission lines characteristic impedances are kept fixed at $Z_1 = 1.8233Z_0\ \Omega$, and $Z_2 = 5.4845Z_0\ \Omega$, using coefficients for a Chebyshev profile with a 10:1 transformation ratio and a 0.05 ripple [Pozar-98].

The optimal coarse model design (analytically obtained) is $\boldsymbol{x}_c^* = [90 \ \ 90]^T$ (degrees). The optimal fine model design (obtained from direct conventional optimization) is $\boldsymbol{x}_f^* = [79.0670 \ 88.6166]^T$. Responses are calculated from 0.2 to 1.8 GHz using $p = 101$ frequency points. The parameter extraction sub-problem considers the complete frequency range.

Fig. 4.7a shows the coarse model optimal response, $\boldsymbol{R}_c(\boldsymbol{x}_c^*)$, which is the target response for ASM, the fine model response at the optimal coarse model design, $\boldsymbol{R}_f(\boldsymbol{x}_c^*)$, which is the initial fine model response of the ASM algorithm, and the actual fine model optimal response, $\boldsymbol{R}_f(\boldsymbol{x}_f^*)$, which is normally unknown in a SM problem. Here we use $\boldsymbol{R}_f(\boldsymbol{x}_f^*)$ to assess the accuracy of the fine model response at the space-mapped solution $\boldsymbol{R}_f(\boldsymbol{x}_f^{SM})$ obtained when using the ASM algorithm with classical *l*-th norms and the K-L formulation. The same is done in the following examples.

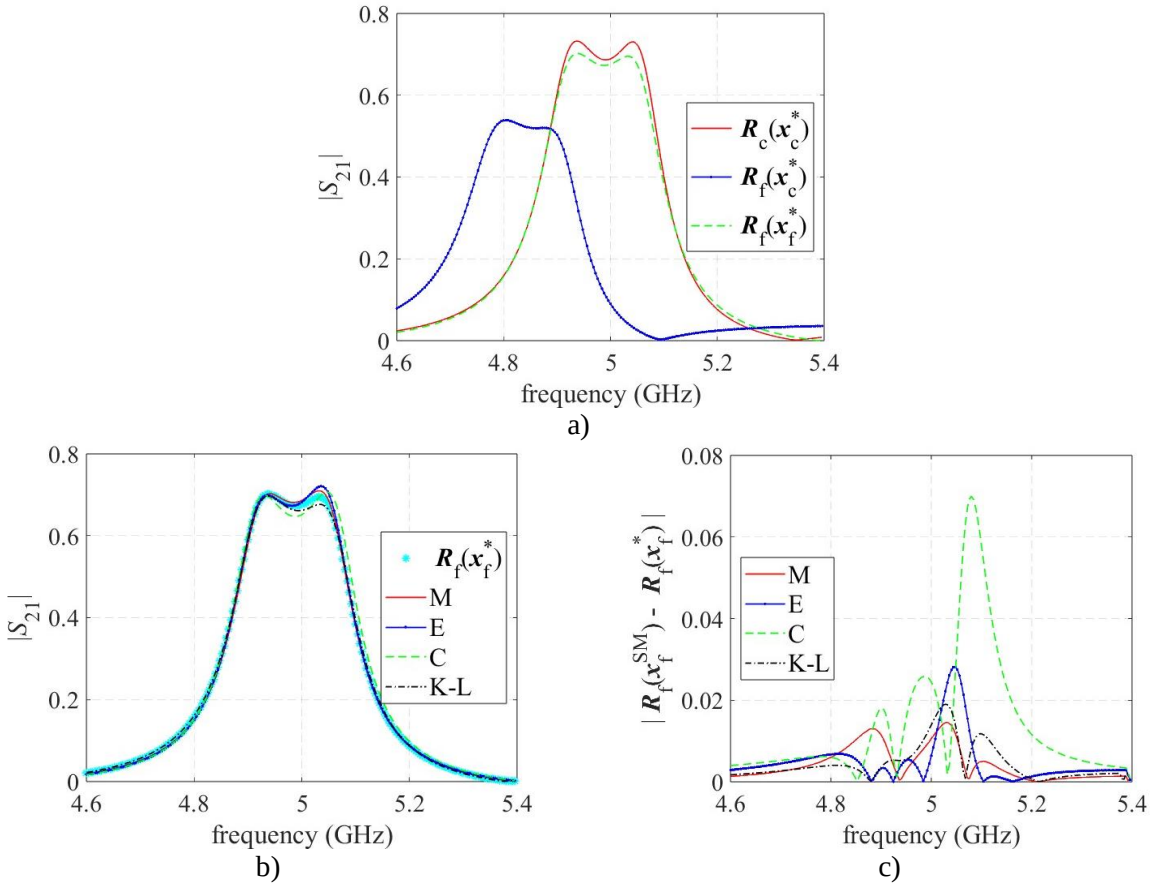

Fig. 4.11 SM results for the band-pass microstrip filter (see Fig. 1.35). a) $\boldsymbol{R}_c(\boldsymbol{x}_c^*)$, $\boldsymbol{R}_f(\boldsymbol{x}_c^*)$, and $\boldsymbol{R}_f(\boldsymbol{x}_f^*)$; b) $\boldsymbol{R}_f(\boldsymbol{x}_f^{SM})$ using Manhattan (M), Euclidean (E), Chebyshev (C), and Kullback-Leibler (K-L) for PE, versus $\boldsymbol{R}_f(\boldsymbol{x}_f^*)$; c) corresponding matching error $|\boldsymbol{R}_f(\boldsymbol{x}_f^{SM}) - \boldsymbol{R}_f(\boldsymbol{x}_f^*)$. Images taken from [Loera-Díaz-25c].

4.5.2 SM Example 2: Single-Stub Band-Stop Microstrip Filter

As a second SM example, consider the single-stub band-stop microstrip filter reported in [Koziel-08] and illustrated in Fig. 1.2. The coarse model uses a Keysight ADS equivalent circuit (see Fig. 4.8a). The fine model uses full-wave EM simulations in Keysight ADS Momentum Microwave with a high-resolution discretization until convergence is reached (see Fig. 4.8b).

This band-stop microstrip filter has only one design parameter $x = L$ (mm). The pre-assigned parameters are $\boldsymbol{z} = [H \ \varepsilon_r \ W \ L_1]^T$, with a substrate thickness $H = 1$ mm, relative dielectric permittivity $\varepsilon_r = 9.3$, microstrips width $W = 1$ mm, and input/output microstrips length $L_1 = 5$ mm. These values of H, ε_r, and W yield a characteristic impedance $Z_0 \approx 50$ Ω. In this example, losses

TABLE 4.6. SM RESULTS FOR THE BAND-PASS FILTER USING DIFFERENT OBJECTIVE FUNCTIONS FOR PE AND THE NELDER-MEAD OPTIMIZATION METHOD FOR PE

OF	$\boldsymbol{x}_c^{(i)T}$	$\boldsymbol{x}_f^{(i)T}$	$N_c^{(i)}$	N_c^t	ε_{avg}^{SM}	ε_{max}^{SM}	ε_{nms}^{SM}	SC
M	[6.92 4.86 5.94 5.68 0.13]^T	[6.61 4.78 5.89 5.38 0.14]^T	165	454	8.03×10^{-11}	2.70×10^{-10}	1.18×10^{-10}	1&3
	[6.64 4.73 5.84 5.42 0.12]^T	[6.30 4.71 5.85 5.08 0.14]^T	289					
		[6.26 4.77 5.91 5.04 0.16]^T						
E	[6.94 4.82 5.92 5.69 0.11]^T	[6.61 4.78 5.89 5.38 0.14]^T	293	582	9.09×10^{-11}	5.22×10^{-10}	1.50×10^{-10}	1&3
	[6.65 4.74 5.85 5.42 0.14]^T	[6.28 4.75 5.87 5.07 0.16]^T	289					
		[6.24 4.80 5.92 5.03 0.16]^T						
C	[6.48 5.14 6.37 5.47 0.12]^T	[6.61 4.78 5.89 5.38 0.14]^T	360	856	2.56×10^{-10}	1.30×10^{-09}	4.16×10^{-10}	3
	[6.96 4.53 5.47 5.57 0.15]^T	[6.74 4.43 5.41 5.29 0.15]^T	298					
	[6.83 4.62 5.68 5.49 0.14]^T	[6.55 4.56 5.64 5.18 0.15]^T	198					
		[6.22 4.81 5.90 5.03 0.14]^T						
K-L	[6.89 4.89 5.94 5.68 0.13]^T	[6.61 4.78 5.89 5.38 0.14]^T	101	261	8.32×10^{-11}	3.52×10^{-10}	1.25×10^{-10}	1&3
	[6.64 4.74 5.86 5.40 0.14]^T	[6.33 4.68 5.85 5.08 0.14]^T	160					
		[6.29 4.72 5.88 5.06 0.14]^T						

are neglected and metals are considered as infinitesimally thin conductors, *i.e.*, loss tangent tan(δ) = 0, metal thickness t = 0, and conductivity σ is infinite [Loera-Díaz-25c].

The optimal fine model design is $\boldsymbol{x}_f^* = 5.906$ and the optimal coarse model design is $\boldsymbol{x}_c^* = 6.1937$. Fig. 4.9a shows $\boldsymbol{R}_c(\boldsymbol{x}_c^*)$, $\boldsymbol{R}_f(\boldsymbol{x}_c^*)$ and $\boldsymbol{R}_f(\boldsymbol{x}_f^*)$.

4.5.3 SM Example 3: Low-Pass Microstrip Filter

As a third SM example, consider the low-pass microstrip filter described in Section 4.3.1. The optimal fine model design is $\boldsymbol{x}_f^* = [1.270 \quad 4.880 \quad 2.365]^T$ and the optimal coarse model design is $\boldsymbol{x}_c^* = [1.5159 \quad 5.2744 \quad 3.1133]^T$. $\boldsymbol{R}_c(\boldsymbol{x}_c^*)$, $\boldsymbol{R}_f(\boldsymbol{x}_c^*)$ and $\boldsymbol{R}_f(\boldsymbol{x}_f^*)$ are shown in Fig. 4.10a.

4.5.4 SM Example 4: Band-Pass Microstrip Filter

As the final SM example, consider the band-pass filter described in Section 4.3.2. The optimal fine model design is $\boldsymbol{x}_f^* = [6.275 \quad 4.75 \quad 5.9 \quad 5.05 \quad 0.15]^T$ and the optimal coarse model design is $\boldsymbol{x}_c^* = [6.6094 \quad 4.7837 \quad 5.8934 \quad 5.3795 \quad 0.1380]^T$. Fig. 4.11a shows $\boldsymbol{R}_c(\boldsymbol{x}_c^*)$, $\boldsymbol{R}_f(\boldsymbol{x}_c^*)$ and $\boldsymbol{R}_f(\boldsymbol{x}_f^*)$.

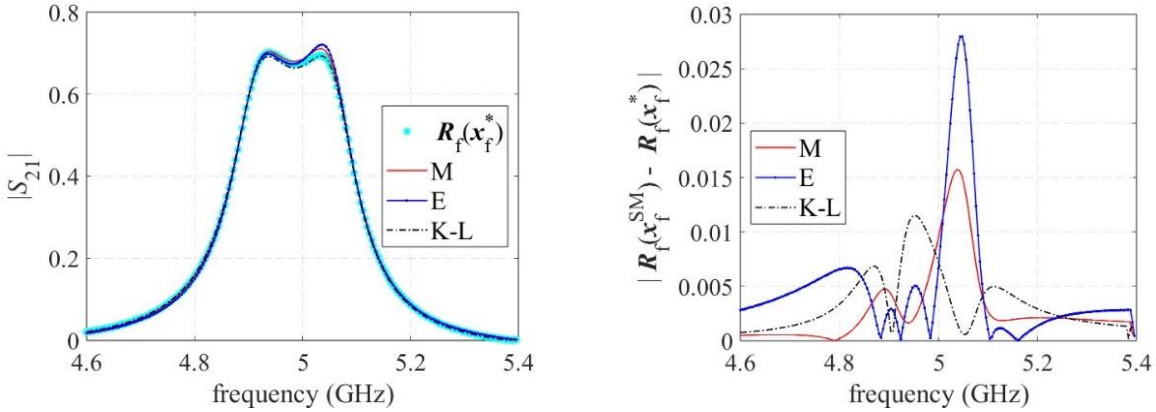

a) b)

Fig. 4.12 SM results results for the band-pass microstrip filter (see Fig. 1.35) when the gradient-based constrained interior-point optimization method is used for PE at each SM iteration (instead of Nelder-Mead). $\boldsymbol{R}_c(\boldsymbol{x}_c^*)$, $\boldsymbol{R}_f(\boldsymbol{x}_c^*)$, and $\boldsymbol{R}_f(\boldsymbol{x}_f^*)$ are the same as those in Fig. 4.11a. a) $\boldsymbol{R}_f(\boldsymbol{x}_f^{SM})$ using Manhattan (M), Euclidean (E), and Kullback-Leibler (K-L) for PE, versus $\boldsymbol{R}_f(\boldsymbol{x}_f^*)$; c) corresponding matching error $|\boldsymbol{R}_f(\boldsymbol{x}_f^{SM}) - \boldsymbol{R}_f(\boldsymbol{x}_f^*)|$. In this case, the Chebyshev norm for PE makes SM to diverge (see Table 4.7). Images taken from [Loera-Díaz-25c].

4.5.5 SM Results and Comparison

The following error metrics are used for numerical comparisons to assess the fine model response at the space-mapped solution $\boldsymbol{R}_f(\boldsymbol{x}_f^{SM})$ found by ASM using all the PE formulations: the average absolute relative error (ε_{avg}^{SM}), the maximum absolute relative error (ε_{max}^{SM}), and the normalized mean square error (ε_{nms}^{SM}), defined as

$$\varepsilon_{avg}^{SM} = \frac{100}{r}\frac{\|\boldsymbol{e}_{SM}\|_1}{\|\boldsymbol{R}_f(\boldsymbol{x}_f^*)\|_\infty} \ (\%) \tag{4-13}$$

$$\varepsilon_{max}^{SM} = \frac{100\|\boldsymbol{e}_{SM}\|_\infty}{\|\boldsymbol{R}_f(\boldsymbol{x}_f^*)\|_\infty} \ (\%) \tag{4-14}$$

$$\varepsilon_{nms}^{SM} = \frac{100\|\boldsymbol{e}_{SM}\|_2}{\|\boldsymbol{R}_f(\boldsymbol{x}_f^*)\|_2} \ (\%) \tag{4-15}$$

where $\boldsymbol{e}_{SM} = \boldsymbol{R}_f(\boldsymbol{x}_f^{SM}) - \boldsymbol{R}_f(\boldsymbol{x}_f^*)$.

The SM results are shown in Fig. 4.7 and Table 4.3 for the synthetic test example, in Fig. 4.9 and Table 4.4 for the single-stub band-stop microstrip filter, in Fig. 4.10 and Table 4.5 for the low-pass microstrip filter, and finally in Fig. 4.11 and Table 4.6 for the band-pass microstrip filter.

In all these examples we use the same optimization method (Nelder-Mead) for PE with the same termination criteria. Tolerances for the PE sub-problem and for SM are as indicated in

TABLE 4.7. SM RESULTS FOR THE BAND-PASS FILTER USING DIFFERENT OBJECTIVE FUNCTIONS FOR PE AND THE GRADIENT-BASED CONSTRAINED INTERIOR-POINT OPTIMIZATION METHOD FOR PE

OF	$\boldsymbol{x}_c^{(i)T}$	$\boldsymbol{x}_f^{(i)T}$	$N_c^{(i)}$	N_c^t	ε_{avg}^{SM}	ε_{max}^{SM}	ε_{nms}^{SM}	SC
M	[6.92 4.84 5.93 5.68 1.22] [6.64 4.75 5.85 5.41 0.14]	[6.61 4.78 5.89 5.38 0.14] [6.30 4.73 5.86 5.07 0.15] [6.27 4.77 5.91 5.04 0.15]	383 209	592	5.53×10^{-11}	9.34×10^{-11}	2.92×10^{-10}	3
E	[6.94 4.82 5.92 5.69 0.11] [6.65 4.74 5.85 5.42 1.41]	[6.61 4.78 5.89 5.38 0.14] [6.28 4.75 5.87 5.07 0.16] [6.24 4.80 5.92 5.03 0.16]	217 178	395	8.95×10^{-11}	1.48×10^{-10}	5.18×10^{-10}	1&3
C	[0.11 0.13 6.00 5.67 1.00] [6.24 5.85 5.92 5.33 0.10] [6.18 5.77 6.00 5.27 0.13] [NA NA NA NA NA]	[6.61 4.78 5.89 5.38 0.14] [13.11 9.43 5.79 5.09 0.18] [13.46 8.41 5.76 5.13 0.21] [27.63 **-24.16** 2.20 8.86 0.32]	338 139 66	NA	NA	NA	NA	NA
K-L	[6.91 4.85 5.93 5.68 0.12] [6.63 4.75 5.86 5.40 0.14]	[6.61 4.78 5.89 5.38 0.14] [6.31 4.72 5.85 5.08 0.15] [6.28 4.75 5.89 5.06 0.15]	145 132	277	6.36×10^{-11}	8.71×10^{-11}	2.14×10^{-10}	3

[Loera-Díaz-25c]. The exiting stop criteria (SC) are represented in Table 4.3 - Table 4.6 by numbers 1 to 4, which correspond to those in (4-12) [Loera-Díaz-25c], respectively.

We can see from Table 4.3 - Table 4.6 that the Broyden-based input SM algorithm with the K-L formulation used for the PE sub-problem outperforms that one with classical norms for PE given the following attributes: 1) it yields similar errors (4-13)-(4-15) in the final fine model response found; 2) it ends with similar or better stopping criteria (SC) satisfied; 3) it takes equal or less fine model evaluations to obtain the SM solution; and 4) it requires less or much less evaluations of the coarse model in the whole SM optimization cycle. These results are consistent with our findings in [Loera-Díaz-20a], where the K-L formulation produces smoother PE objective functions with larger dynamic ranges as compared to those produced with classical *l*-th norms.

By contrasting the overall results in Table 4.3 - Table 4.6, it is also observed that, as we increase the complexity and the dimensionality of the problem, the K-L formulation for PE makes SM exhibit a clearer enhanced performance as compared to that one using classical norms for PE.

It is well known that the overall CPU time employed by any SM technique essentially depends on the number of fine model evaluations. However, if the coarse model in a given SM problem is not that computationally inexpensive, performing less coarse model evaluations during PE at each SM iteration can also produce a non-negligible speed up. For instance, in the fourth SM example (see Table 4.6), the total execution time (minutes:seconds) of all the coarse model evaluations for PE is 05:38 by K-L formulation, 09:48 by Manhattan norm, 12:33 by Euclidean

norm, and 18:27 by Chebyshev norm, using a conventional laptop computer (AMD Ryzen® 7 5700U processor with AMD Radeon® Graphics 1.80 GHz and 16 GB RAM).

Regarding the numerical optimization method employed for PE, in [Loera-Díaz-20a] we use not only the Nelder-Mead method to compare PE with a K-L formulation versus classical norms, but also the trust region interior-reflective Newton method, which is a gradient-based method, as well as a comparison based on the graphical contours of the corresponding PE objective functions, making our conclusions on PE behavior independent of the optimization technique employed for PE [Loera-Díaz-20a]. To study the effects of changing the optimization method for PE in SM, we solved again the fourth example by using the gradient-based constrained interior-point optimization method available in Matlab to perform PE at each SM iteration. The corresponding results are shown in Table 4.7 and Fig. 4.12. It is seen that these results fully support our previous conclusions, confirming the benefits of using a K-L formulation against using classical norms for PE in classical Broyden-based input SM. It is also seen in Table 4.7 that SM fails (diverges) when using a Chebyshev norm for PE and the gradient-based constrained interior-point optimization method to do PE at each SM iteration.

Finally, the proposed new formulation for Broyden-based input SM using a K-L distance for PE can also be applied to design optimization problems in other microwave technologies, such as waveguide technology. Several problems in waveguide and other technologies might be considered in a future and more general contribution.

4.6. Conclusion

A Broyden-based input space mapping (SM) algorithm, using a Kullback-Leibler (K-L) formulation as objective function for the parameter extraction (PE) sub-problem, was proposed for the first time. First, we applied PE with the K-L formulation to microstrip filters using their full-wave electromagnetic (EM) responses as targets, and we performed a rigorous numerical comparison against PE with classical norms. Next, we applied SM design optimization, using PE with the K-L formulation, to several examples, beginning with a classical synthetic example and following with some microstrip filters whose full-wave EM simulations were used as fine models, and their equivalent distributed circuits were used as coarse models. Then, we performed a rigorous numerical comparison between classical *l*-th norms and the K-L formulation for PE within

the corresponding SM design optimizations. Our results indicate that Broyden-based input SM with the K-L formulation in the PE sub-problem outperforms that one with classical *l*-th norms. Other SM techniques that require performing PE could similarly benefit from the K-L formulation.

General Conclusions

High-frequency circuits are widely used in modern electronics for many different applications, such as telecommunications, automotive electronics, and computer equipment, among others. Distributed-element circuits and full-wave electromagnetic (EM) simulations are employed for modeling these circuits since lumped-element circuits are not adequate for these frequencies.

To adjust and optimize these high-frequency circuits, simulation software is employed. Full-wave EM simulations are more accurate than simulations based on distributed equivalent circuits. However, full-wave EM simulations must be properly configured to obtain reliable simulation responses.

Direct optimization of radio frequency and microwave circuits using full-wave EM simulations is computationally very expensive, and could be unfeasible in many situations. Microwave components optimization during the design process can be assisted by space mapping (SM) algorithms to accelerate the optimization process, using full-wave EM simulations as fine model, with the support of faster but more inaccurate equivalent circuit simulations as coarse model.

Parameter extraction (PE) is an important sub-process employed in many SM algorithms. The role of PE in SM is crucial on the convergence and robustness of SM. Therefore, any improved form of PE is highly valuable in the context of SM.

In Chapter 1 of this doctoral dissertation, a procedure to configure ADS Momentum to obtain reliable 2-D EM simulations for some filters in microstrip technology was presented. The validated circuits were a single-stub band-stop filter, a low-pass filter, a band-pass filter and another band-stop filter. Some of the validated EM models shown in this chapter were later used in Chapter 3 and Chapter 4.

In Chapter 2, a formulation for PE based in terms of the K-L distance was proposed. Then, a rigorous comparison against classical norm formulations, that is, Manhattan, Euclidean, and Chebyshev norms, was performed. To illustrate this comparison, two different synthetic examples were used: an ideal 10:1 two section impedance transformer as a one-dimensional PE example, and a sixth-order π band-pass lumped filter as a two-dimensional PE example. Our results indicated

that the proposed K-L formulation for PE yields similar or better performance than PE with classical norm formulations, since the K-L formulation required less or a similar number of iterations for a satisfactory matching response in the PE sub-process and it presented smother objective functions.

In Chapter 3, a graphical and numerical study of PE based on the proposed K-L formulation against classical norm formulations (Manhattan, Euclidean, and Chebyshev norms) was presented. For this study, three synthetic examples were used: a one-section impedance transformer, a two-section impedance transformer, and a third-order low pass asymmetrical lumped filter. In addition to these synthetic examples, a single-stub band-stop filter in microstrip technology validated in Chapter 1 was also employed. This chapter also showed that the K-L distance formulation for PE calculated with natural logarithm and 10-base logarithm yields equivalent results. It was also shown that the K-L formulation in "reverse order" yields softer objective functions with less local minima in comparison with that one using the "direct order". Our results, illustrated with a single-stub band-stop filter in microstrip technology, showed that the promising behavior of PE shown with synthetic examples, remains in more complex examples, such as, but not limited to, structures implemented in microstrip technology. These results confirmed that PE with the K-L formulation requires less evaluations of the objective function with similar or better error matching in comparison with PE based on classical norms.

In Chapter 4, the most important contribution of this doctoral dissertation was presented. This chapter proposed a Broyden-based input SM algorithm with PE based on the K-L formulation. First, it presented a couple of PE examples illustrated with a low-pass and a band-pass filter validated in Chapter 1. Then, SM was illustrated first with a synthetic example, a one-section impedance transformer used in Chapter 2, and next with a single-stub band-stop filter, a low-pass filter, and a band-pass filter in microstrip technology, all validated in Chapter 1. Our results showed that SM with PE based on the K-L formulation yields a similar or better response error matching in similar or less evaluations of the coarse model for each PE iteration, in comparison to PE based on classical norm formulations. Our results also showed that, as we increased the complexity and dimensionality of the problem, PE based on the K-L formulation exhibits an even better performance in comparison to PE based on classical norm formulations.

In summary, this doctoral dissertation proposed a new formulation of SM with PE based on the Kullback-Leibler distance for Broyden-based input SM, which yields similar or better

response matching with similar or less evaluations of the coarse model.

Some possible future research opportunities are related to this dissertation. One possible future research work consists of applying the proposed Broyden-based input space mapping with the K-L distance PE to higher-order microstrip filters, or other types of microstrip circuits such as impedance matching networks, power dividers, etc. This proposed SM formulation could also be applied to design optimization problems in other microwave technologies, such as waveguide technologies. Moreover, this formulation might also be applied to other fields, such as, antenna design, MEMS devices, among others.

As mentioned in Section 4.5.5, as we increased the complexity and the dimensionality of the problem, the K-L formulation exhibited a clearer enhanced performance in comparison to the one obtained with classical norms. Therefore, further studies regarding this aspect, by considering large-scale problems, would be very relevant. Another potential research line would be the integration of the K-L formulation for parameter extraction assisted by artificial intelligence techniques (possibly combined with cognition driven parameter extraction [Rayas-Sánchez-25b], [Rayas-Sánchez-25c]).

During this doctoral dissertation, the analyzed examples only considered deterministic responses. Therefore, another possible future work opportunity could be the study of the effects of using SM with PE based on the K-L formulation for fine model responses with statistical fluctuations. For example, microwave designs considering manufacturing variability could be considered. This is a promising future research line based on the fact that the K-L distance has been successfully employed to measure the difference between probabilistic distributions.

Further studies of SM with PE based on formulations different than the K-L distance could be realized, such as, but not limited to, formulations employed in artificial vision for pattern recognition, imaging processing, etc.

Conclusiones generales

Los circuitos de alta frecuencia son ampliamente usados en la electrónica moderna para muchas aplicaciones diferentes, tales como telecomunicaciones, electrónica automotriz, equipo de cómputo, entre otros. Los circuitos de elementos distribuidos y las simulaciones electromagnéticas de onda completa son empleados para el modelado de estos circuitos debido a que los circuitos de elementos concentrados no son adecuados para estas frecuencias.

Para ajustar y optimizar estos circuitos de altas frecuencias, programas de simulación son utilizados. Las simulaciones electromagnéticas de onda completa son más exactas que las simulaciones basadas en circuitos distribuidos equivalentes. Sin embargo, las simulaciones electromagnéticas de onda completa deben de ser apropiadamente configuradas para obtener respuestas de simulación confiables.

La optimación directa de circuitos de radio frecuencia y microondas, usando simulaciones electromagnéticas de onda completa, es computacionalmente muy costosa, al grado de que puede ser inviable en muchas situaciones. La optimización de componentes de microondas, durante el proceso de diseño, puede ser asistida por algoritmos de mapeo espacial para acelerar el proceso de optimización, usando simulaciones electromagnéticas de onda completa como modelo fino, con el soporte de simulaciones de circuitos equivalentes, que son mucho más rápidas, pero más inexactas, como modelo burdo.

La extracción de parámetros es un subproceso importante empleado en muchos algoritmos de mapeo espacial. El rol de la extracción de parámetros en mapeo espacial es crucial en la convergencia y robustez de mapeo espacial. Por lo tanto, cualquier forma mejorada de extracción de parámetros es altamente valiosa en el contexto de mapeo espacial.

En el Capítulo 1 de esta disertación doctoral, un procedimiento para configurar ADS Momentum, para obtener simulaciones electromagnéticas 2-D confiables para algunos filtros en tecnología microcinta, fue presentado. Los circuitos validados fueron un filtro supresor de banda de un solo resonador, un filtro pasa bajas, un filtro pasa banda y otro filtro supresor de banda. Algunos de los modelos electromagnéticos validados y mostrados en este capítulo fueron después utilizados en el Capítulo 3 y el Capítulo 4.

En el Capítulo 2, una formulación de extracción de parámetros basada en términos de la

distancia de Kullback-Leibler fue propuesta. Después, se realizó una comparación rigurosa contra formulaciones de normas clásicas, esto es, norma Manhattan, Euclidiana y Chebyshev. Para ilustrar esta comparación, dos ejemplos sintéticos diferentes fueron usados: un transformador de impedancia ideal 10:1 de dos secciones, como ejemplo de extracción de parámetros de una dimensión, y un filtro π pasa banda de parámetros concentrados de sexto orden, como ejemplo de extracción de parámetros de dos dimensiones. Nuestros resultados indicaron que la formulación propuesta de Kullback-Leibler para extracción de parámetros produce un desempeño similar o mejor que las formulaciones de extracción de parámetros con normas clásicas, debido a que la formulación de Kullback-Leibler requirió de un número inferior o similar de iteraciones para un empate de respuesta satisfactorio en el sub-proceso de extracción de parámetros, y presentó también funciones objetivo más suaves.

En el Capítulo 3, un estudio gráfico y numérico de la extracción de parámetros propuesta, basada en la formulación de Kullback-Leibler, contra formulaciones clásicas (normas Manhattan, Euclidiana y Chebyshev), fue presentado. Para este estudio, tres ejemplos sintéticos fueron usados: un transformador de impedancia de una sección, un transformador de impedancia de dos secciones, y un filtro simétrico concentrado pasa bajas de tercer orden. Además de estos ejemplos sintéticos, un filtro supresor de banda en tecnología microcinta de un solo resonador, validado en el Capítulo 1, fue empleado. Este capítulo también mostró que la formulación de la distancia de Kullback-Leibler para extracción de parámetros, calculada con logaritmo base 10 y logaritmo natural, produce resultados equivalentes. También se mostró que la formulación de Kullback-Leibler en "orden inverso" produce funciones objetivo más suaves y con menos mínimos locales en comparación con la formulación en "orden directo". Nuestros resultados, ilustrados con un filtro supresor de banda en tecnología microcinta de un solo resonador, mostraron que el prometedor comportamiento de extracción de parámetros, mostrado con ejemplos sintéticos, prevalece en ejemplos más complejos, tales como, pero sin limitarse a, estructuras implementadas en tecnología microcinta. Estos resultados confirmaron que la extracción de parámetros con la formulación de Kullback-Leibler requieren menos evaluaciones de la función objetivo, arrojando además un error de empate en las respuestas similar o mejor en comparación a la extracción de parámetros basada en normas clásicas.

En el Capítulo 4, la contribución más importante de esta disertación doctoral fue presentada. En este capítulo se propuso un algoritmo de mapeo espacial a la entrada basado en

Broyden con extracción de parámetros basada en la distancia de Kullback-Leibler. Primero, se presentó un par de ejemplos de extracción de parámetros ilustrados con un filtro pasa bajas y un filtro pasa banda, los cuales fueron validados en el Capítulo 1. Después, se ilustró el mapeo espacial, primero con un ejemplo sintético, un transformador de impedancia de una sección usado en el Capítulo 2, y luego con un filtro rechaza banda de un solo resonador, un filtro pasa bajas y un filtro pasa banda en tecnología microcinta, todos validados en el Capítulo 1. Nuestros resultados mostraron que el mapeo espacial con extracción de parámetros basada en la formulación de Kullback-Leibler produce un error de empate de respuesta similar o mejor en un número similar o menor de evaluaciones del modelo burdo para cada iteración de extracción de parámetros, en comparación con la extracción de parámetros basada en formulaciones de normas clásicas. Nuestros resultados también mostraron que, conforme se incrementa la complejidad y dimensionalidad del problema, la extracción de parámetros basada en la formulación de Kullback-Leibler presenta incluso un aún mejor desempeño en comparación a la extracción de parámetros basada en formulaciones de normas clásicas.

En resumen, esta disertación doctoral propuso una nueva formulación de mapeo espacial con extracción de parámetros basada en la distancia de Kullback-Leibler para mapeo espacial a la entrada basado en Broyden, el cual produce un empate de respuesta similar o mejor con un número similar o menor de evaluaciones del modelo burdo.

Varias posibles oportunidades de investigación futuras están relacionadas con esta disertación. Un posible trabajo futuro de investigación consiste en aplicar el mapeo espacial con extracción de parámetros basada en la distancia de Kullback-Leibler en filtros microcinta de mayor orden, o en otros tipos de circuitos microcinta, tales como redes de acoplamiento de impedancia, divisores de potencia, etc. Esta formulación propuesta de mapeo espacial también podría ser aplicada a problemas de optimización de diseño en otras tecnologías de microondas, tales como tecnologías de guía de onda. Además, esta formulación podría ser implementada en otros campos, tales como en el diseño de antenas, dispositivos MEMS, entre otros.

Como se mencionó en la Sección 4.5.5, conforme incrementamos la complejidad y dimensión del problema, la formulación de K-L presenta una más clara mejoría en el desempeño con respecto al que se obtiene con normas clásicas. Por lo tanto, estudios adicionales de este aspecto, considerando problemas de dimensiones grandes (o a gran escala), serían muy relevantes. Otra línea potencial de investigación sería la integración de la formulación de K-L para extracción

de parámetros asistida por técnicas de inteligencia artificial (posiblemente combinada con extracción de parámetros conducida por cognición [Rayas-Sánchez-25b], [Rayas-Sánchez-25c]).

Durante esta disertación doctoral, los ejemplos analizados solo consideraron respuestas determinísticas. Por lo tanto, otra posible oportunidad de trabajo futuro podría ser el estudio de los efectos de utilizar mapeo espacial con extracción de parámetros basada en la formulación de Kullback-Leibler para respuestas del modelo fino con fluctuaciones estadísticas. Esta es una prometedora línea de investigación a futuro, considerando el hecho de que la distancia de Kullback-Leibler ha sido exitosamente empleada para medir la diferencia entre distribuciones de probabilidad.

Estudios adicionales de mapeo espacial con extracción de parámetros basada en formulaciones diferentes a la distancia de Kullback-Leibler también podrían ser realizados, tales como, pero no limitadas a, formulaciones típicamente empleadas en visión artificial para el reconocimiento de patrones, procesamiento de imágenes, etc.

Appendix

A. LIST OF INTERNAL RESEARCH REPORTS

1) R. Loera-Díaz, J. E. Rayas-Sánchez, and Zabdiel Brito-Brito, "Monte-Carlo analysis, yield estimation, and worst-case prediction of a microstrip filter," Internal Report *PhDEngScITESO-18-23-R (CAECAS-18-09-R)*, ITESO, Tlaquepaque, Mexico, Aug. 2018.

2) R. Loera-Díaz, J. E. Rayas-Sánchez, and Zabdiel Brito-Brito, "A formulation for circuit parameter extraction based on the Kullback-Leibler distance," Internal Report *PhDEngScITESO-19-10-R (CAECAS-19-12-R)*, ITESO, Tlaquepaque, Mexico, Jul. 2019.

3) R. Loera-Díaz and J. E. Rayas-Sánchez, "An enhanced objective function for circuit parameter extraction based on the Kullback-Leibler distance," Internal Report *PhDEngScITESO-19-37-R (CAECAS-19-15-R)*, ITESO, Tlaquepaque, Mexico, Dec. 2019.

4) R. Loera-Díaz and J. E. Rayas-Sánchez, "Aggressive space mapping with parameter extraction based on the Kullback-Leibler distance: synthetic examples," Internal Report *PhDEngScITESO-20-11-R (CAECAS-20-07-R)*, ITESO, Tlaquepaque, Mexico, Aug. 2020.

5) R. Loera-Díaz, J. E. Rayas-Sánchez, and Zabdiel Brito-Brito, "A comparative study of several topologies for band-pass and band-stop filters in microstrip technology," Internal Report *PhDEngScITESO-20-21-R (CAECAS-20-09-R)*, ITESO, Tlaquepaque, Mexico, Dec. 2020.

6) R. Loera-Díaz and J. E. Rayas-Sánchez, "Validating electromagnetic models implemented in ADS Momentum for several filters in microstrip technology," Internal Report *PhDEngScITESO-22-19-R (CAECAS-22-07-R)*, ITESO, Tlaquepaque, Mexico, Nov. 2022.

7) R. Loera-Díaz and J. E. Rayas-Sánchez, “Comparison of ADS circuital models for a microstrip low-pass filter,” Internal Report *PhDEngScITESO-23-05-R (CAECAS-23-02-R),* ITESO, Tlaquepaque, Mexico, Aug. 2023.

8) R. Loera-Díaz and J. E. Rayas-Sánchez, “Parameter extraction graphical study using Kullback-Leibler formulations,” Internal Report *PhDEngScITESO-23-13-R (CAECAS-23-04-R),* ITESO, Tlaquepaque, Mexico, Dec. 2023.

9) R. Loera-Díaz and J. E. Rayas-Sánchez, “Parameter extraction using l-norms and the Kullback-Leibler formulation in a validated EM model of a single-stub microstrip band-stop filter,” Internal Report *PhDEngScITESO-24-12-R (CAECAS-24-04-R),* ITESO, Tlaquepaque, Mexico, Jul. 2024.

10) R. Loera-Díaz and J. E. Rayas-Sánchez, “A rigorous numerical comparison for parameter extraction using classical and Kullback-Leibler formulations for microstrip filters,” Internal Report *PhDEngScITESO-24-17-R (CAECAS-24-06-R),* ITESO, Tlaquepaque, Mexico, Nov. 2024.

11) R. Loera-Díaz and J. E. Rayas-Sánchez, “Aggressive space mapping with parameter extraction based on the Kullback-Leibler distance applied to a synthetic example and some validated EM models of microstrip filters,” Internal Report *PhDEngScITESO-25-04-R (CAECAS-25-01-R),* ITESO, Tlaquepaque, Mexico, Apr. 2025.

B. LIST OF PUBLICATIONS

B.1. CONFERENCE PAPERS

1) **R. Loera-Díaz** and J. E. Rayas-Sánchez, "An objective function formulation for circuit parameter extraction based on the Kullback-Leibler distance," in *IEEE MTT-S Int. Microwave Symp. Dig.*, Los Angeles, CA, Aug. 2020, pp. 80-82. (ISSN: 0149-645X; ISSN-e: 2576-7216; ISBN: 978-1-7281-6816-6; e-ISBN: 978-1-7281-6815-9; INSPEC: 20054460; DOI: 10.1109/IMS30576.2020.9224002).
https://ieeexplore-ieee-org/document/9224002/

2) **R. Loera-Díaz**, J. E. Rayas-Sánchez and E. R. Villa-Loustaunau, "A rigorous numerical comparison for parameter extraction using classical and Kullback-Leibler formulations illustrated with full-wave EM and equivalent circuit models for microstrip filters," in *IEEE MTT-S Latin America Microwave Conf. (LAMC-2025)*, San Juan, Puerto Rico, Jan. 2025, pp. 93-96. (ISBN: 979-8-3315-4041-8; e-ISBN: 979-8-3315-4040-1; DOI: 10.1109/LAMC63321.2025.10880557).
https://ieeexplore.ieee.org/document/10880557

3) E. R. Villa-Loustaunau, J. E. Rayas-Sánchez, **R. Loera-Díaz**, and F. Rangel-Patiño, "Optimizing the full mixed-mode performance of a differential microstrip interconnect with a right-angle bend by using two symmetrical bumps," in *IEEE MTT-S Latin America Microwave Conf. (LAMC-2025)*, San Juan, Puerto Rico, Jan. 2025, pp. 97-100. (ISBN: 979-8-3315-4041-8; e-ISBN: 979-8-3315-4040-1; DOI: 10.1109/LAMC63321.2025.10880547).
https://ieeexplore.ieee.org/document/10880547

B.2. JOURNAL PAPER

1) **R. Loera-Díaz** and J. E. Rayas-Sánchez, “Space mapping with parameter extraction based on the Kullback–Leibler distance illustrated with full-wave EM and equivalent circuit models for microstrip filters,” *IEEE Trans. Microwave Theory Techn.*, vol. 73, no. 11, pp. 8383-8392, Nov. 2025. (p-ISSN: 0018-9480; e-ISSN: 1557-9670; published online: 21 July 2025; DOI: 10.1109/TMTT.2025.3588177).
https://ieeexplore.ieee.org/document/11086482
https://doi.org/10.1109/TMTT.2025.3588177

Bibliography

[Aksun-05] I. Aksun and N. Kinayman, *Modern Microwave Circuits*. Norwood, MA: Artech House, 2005.

[Bakr-00] M. H. Bakr, J. W. Bandler, K. Madsen, J. E. Rayas-Sanchez, and J. Søndergaard, "Space-mapping optimization of microwave circuits exploiting surrogate models," *IEEE Trans. Microwave Theory Techn.*, vol. 48, no. 12, pp. 2297-2306, Dec. 2000.

[Bandler-95] J. W. Bandler, R. M. Biernacki, S. H. Chen, R. H. Hemmers, and K. Madsen, "Electromagnetic optimization exploiting aggressive space mapping," *IEEE Trans. Microw. Theory Tech.*, vol. 41, no. 12, pp. 2874-2882, Dec. 1995.

[Bandler-99] J. W. Bandler, R. M. Biernacki, S. H. Chen, and D. Omeragic, "Space mapping optimization of waveguide filters using finite element and mode-matching electromagnetic simulators," *Int. J. RF Microwave Computer-Aided Eng.*, vol. 9, no. 1, pp. 54-70, Jan. 1999.

[Bandler-04] J. W. Bandler, Q. Cheng, A. S. Mohamed, M. H. Bakr, K. Madsen, and J. Søndergaard, "Space mapping: the state of the art," *IEEE Trans. Microwave Theory Techn.*, vol. 52, no. 1, pp. 337-361, Jan. 2004.

[Bandler-23] J. W. Bandler and J. E. Rayas-Sánchez, "An early history of optimization technology for automated design of microwave circuits," *IEEE J. Microwaves*, vol. 3, no. 1, pp. 319-337, Jan. 2023.

[Bouhlel-19] N. Bouhlel and A. Dziri, "Kullback–Leibler divergence between multivariate generalized Gaussian distributions," *IEEE Signal Processing Letters*, vol. 26, no. 7, pp. 1021-1025, July 2019.

[Brito-Brito-12] Z. Brito-Brito and J. E. Rayas-Sánchez, "EM simulation of a lossless microstrip bandpass filter using COMSOL with lumped ports," Internal Report *CAECAS-12-07-R*, ITESO, Tlaquepaque, Mexico, May. 2012.

[Brito-Brito-13] Z. Brito-Brito, J. E. Rayas-Sánchez, J. C. Cervantes-González, and C. A. López, "Impact of 3D EM model configuration on the direct optimization of microstrip structures," in *COMSOL Conf.*, Boston, MA, Oct. 2013, pp. 1-5.

[Brito-Brito-15] Z. Brito-Brito, J. E. Rayas-Sánchez, and J. L. Chávez-Hurtado, "Enhanced procedure to setup the simulation bounding box and the meshing scheme of a 3D finite element EM simulator for planar microwave structures," in *IEEE MTT-S Int. Microwave Symp. Dig.*, Phoenix, AZ, May 2015, pp. 1-3.

[Cervantes-Gónzalez-12] J. C. Cervantes-Gónzalez, Z. Brito-Brito, C. A. López, and J. E. Rayas-Sánchez, "EM-thermo-mechanical simulation of a microstrip bandpass filter using COMSOL Multiphysics," Internal Report *CAECAS-12-12-R*, ITESO, Tlaquepaque, México, Jun. 2012.

[Chávez-Hurtado-13] J. L. Chávez-Hurtado, Z. Brito-Brito, and J. E. Rayas-Sánchez, "Coarse and fine models for a fifth order Chebyshev bandstop microstrip filter with L-shaped resonators using COMSOL and Sonnet," Internal Report *PhDEngScITESO-13-01-R (CAECAS-13-08-R)*, ITESO, Tlaquepaque, México, Dec. 2013.

[Chávez-Hurtado-14a] J. L. Chávez-Hurtado and J. E. Rayas-Sánchez, "Four benchmark microstrip line models," Internal Report *PhDEngScITESO-14-03-R (CAECAS-14-04-R)*, ITESO, Tlaquepaque, Mexico, Jul. 2014.

[Chávez-Hurtado-14b] J. L. Chávez-Hurtado, J. E. Rayas-Sánchez, and Z. Brito-Brito, "COMSOL configuration for the EM simulation of a single-layer SIW interconnect with transitions to microstrip lines," Internal Report *PhDEngScITESO-14-07-R (CAECAS-14-07-R)*, ITESO, Tlaquepaque, Mexico, Oct. 2014.

[Chávez-Hurtado-14c] J. L. Chávez-Hurtado, J. E. Rayas-Sánchez, and Z. Brito-Brito, "Reliable full-wave EM simulation of a single-layer SIW interconnect with transitions to microstrip lines," in *COMSOL Conf.*, Boston, MA, Oct. 2014, pp. 1-5.

[Chávez-Hurtado-16] J. L. Chávez-Hurtado and J. E. Rayas-Sánchez, "An initial temperature-dependent polynomial surrogate model of a microstrip bandpass filter using COMSOL Multiphysics," Internal Report *PhDEngScITESO-16-03-R (CAECAS-16-04-R)*, ITESO, Tlaquepaque, México, Feb. 2016.

[Chen-08] J. Chen, J. R. Hershey, P. A. Olsen, and E. Yashchin, "Accelerated Monte Carlo for Kullback-Leibler divergence between Gaussian mixture models," in *2008 IEEE Int. Conf. Acoustics, Speech and Signal Processing*, Las Vegas, NV, USA, 2008, pp. 4553-4556.

[Cheng-08] Q. S. Cheng, J. W. Bandler, and S. Koziel, "Combining coarse and fine models for optimal design," in *IEEE Microwave Mag.*, vol. 9, no. 1, pp. 79-88, Feb. 2008.

[Cui-02] X. Cui and A. Alwan, "Efficient adaptation text design based on the Kullback-Leibler measure," in *2002 IEEE Int. Conf. on Acoustics, Speech, and Signal Processing*, Orlando, FL, USA, 2002, pp. I-613-I-616.

[D'Inzeo-79] G. D'Inzeo, F. Giannini, and R. Sorrentino, "Novel microwave integrated low-pass filters," *Electron. Lett.*, vol. 15, no. 9, pp. 258-260, Apr. 26, 1979.

[Do-02] N. Do, M. Vetterli, "Wavelet-based texture retrieval using generalized Gaussian density and Kullback-Leibler," in *IEEE Transactions on Image Processing*, vol. 11, no. 2, pp. 146-158, Feb. 2002.

[Dunn-14] W. J. M. Dunn, "Where did EM simulation tools go?: a comparison of how EM tools were used in circuit simulators 25 years ago to today," *IEEE Microwave Magazine*, vol. 15, no. 1, pp. 65-69, Jan.-Feb. 2014.

[Erven-14] T. van Erven and P. Harremos, "Rényi divergence and Kullback-Leibler divergence," *IEEE Trans. Information Theory*, vol. 60, no. 7, pp. 3797-3820, July 2014.

[Gutiérrez-Ayala-10] V. Gutiérrez-Ayala and J. E. Rayas-Sánchez, "Neural input space mapping optimization based on nonlinear two-layer perceptrons with optimized nonlinearity," *Int. J. RF and Microwave CAE*, vol. 20, pp. 512-526, Sep. 2010.

[Han-22] B. Han and B. -K. Bao, "River channel extraction in SAR images using level sets driven by symmetric Kullback–Leibler distance," *IEEE Trans. Geoscience Remote Sensing*, vol. 60, pp. 1-16, 2022.

[Harrington-67] R. F. Harrington, "Matrix methods for field problems," *Proc. IEEE*, vol. 55, no. 2, pp. 136-149, Feb. 1967.

[Hennings-06] A. Hennings, E. Semouchkina, A. Baker, and G. Semouchkin, "Design optimization of bandpass filters with normally fed microstrip resonators loaded by high-permittivity dielectric," *IEEE Trans. Microwave Theory Tech.*, vol. 54, no. 3, pp. 1253-1261, Mar. 2006.

[Hershey-07] J. R. Hershey and P. A. Olsen, "Approximating the Kullback Leibler divergence between Gaussian mixture models," in *2007 IEEE Int. Conf. Acoustics, Speech Signal Processing - ICASSP '07*, Honolulu, HI, USA, 2007, pp. IV-317-IV-320.

[Hong-01] J. S. Hong and M. J. Lancaster, *Microstrip Filters for RF/Microwave Applications*. New York, NY: John Wiley & Sons, Inc, 2001.

[Keysight-22] Keysight Technologies (1985-2022), *Electronic Design Automation (EDA) Software, Advanced Design System 2022*, Jul. 2022.

[Kogure-11] H. Kogure, Y. Kogure, and J. C. Rautio, *Introduction to RF Design Using EM Simulators.* Norwood, MA: Artech House, 2011.

[Koziel-06] S. Koziel, J. W. Bandler, and K. Madsen, "A space-mapping framework for engineering optimization - theory and implementation," *IEEE Trans. Microwave Theory Tech.*, vol. 54, pp. 3721-3730, Oct. 2006.

[Koziel-08] S. Koziel, Q. S. Cheng, and J. W. Bandler, "Space mapping," *IEEE Microwave Magazine*, vol. 9, no. 6, pp. 105-122, Dec. 2008.

[Koziel-13] S. Koziel, X-S Yang, and Q. J. Zhang, *Simulation-Driven Design Optimization and Modeling for Microwave Engineering*. London, England: Imperial College Press, 2013.

[Kullback-51] S. Kullback and R. Leibler, "On the information and sufficiency," *Ann. Math. Statist.*, vol. 22, pp. 79-86, 1951.

[Kullback-87] S. Kullback, "Letter to the Editor: The Kullback-Leibler distance," *The American Statistician*, vol. 41, no. 4, pp. 340, 1987.

[Leal-Romo-17] F. J. Leal-Romo and J. E. Rayas-Sánchez, "ADS-Matlab automation driver," Internal Report *PhDEngScITESO-17-31-R (CAECAS-17-14-R)*, ITESO, Tlaquepaque, Mexico, Nov. 2017.

[Lee-11] C. -H. Lee, F. Gutierrez, and D. Dou, "Calculating feature weights in Naive Bayes with Kullback-Leibler measure," in *2011 IEEE Int. Conf. Data Mining*, Vancouver, BC, Canada, 2011, pp. 1146-1151.

[Loera-Díaz-18] R. Loera-Díaz, J. E. Rayas-Sánchez, and Z. Brito-Brito, "Monte-Carlo analysis, yield estimation, and worst-case prediction of a microstrip filter," Internal Report *PhDEngScITESO-18-23-R (CAECAS-18-09-R)*, ITESO, Tlaquepaque, Mexico, Aug. 2018.

[Loera-Díaz-19a] R. Loera-Díaz, J. E. Rayas-Sánchez, and Z. Brito-Brito, "A formulation for circuit parameter extraction based on the Kullback-Leibler distance," Internal Report *PhDEngScITESO-19-10-R (CAECAS-19-12-R)*, ITESO, Tlaquepaque, Mexico, Jul. 2019.

[Loera-Díaz-19b] R. Loera-Díaz and J. E. Rayas-Sánchez, "An enhanced objective function for circuit parameter extraction based on the Kullback-Leibler distance," Internal Report *PhDEngScITESO-19-37-R (CAECAS-19-15-R)*, ITESO, Tlaquepaque, Mexico, Dec. 2019.

[Loera-Díaz-20a] R. Loera-Díaz and J. E. Rayas-Sánchez, "An objective function formulation for circuit parameter extraction based on the Kullback-Leibler distance," in *IEEE MTT-S Int. Microwave Symp. Dig.*, Los Angeles, CA, Aug. 2020, pp. 80-82.

[Loera-Díaz-20b] R. Loera-Díaz and J. E. Rayas-Sánchez, "Aggressive space mapping with parameter extraction based on the Kullback-Leibler distance: synthetic examples," Internal Report *PhDEngScITESO-20-11-R (CAECAS-20-07-R)*, ITESO, Tlaquepaque, Mexico, Aug. 2020.

[Loera-Díaz-20c] R. Loera-Díaz, J. E. Rayas-Sánchez, and Z. Brito-Brito, "A comparative study of several topologies for band-pass and band-stop filters in microstrip technology," Internal Report *PhDEngScITESO-20-21-R (CAECAS-20-09-R)*, ITESO, Tlaquepaque, Mexico, Dec. 2020.

[Loera-Díaz-22] R. Loera-Díaz and J. E. Rayas-Sánchez, "Validating electromagnetic models implemented in ADS Momentum for several filters in microstrip technology," Internal Report *PhDEngScITESO-22-19-R (CAECAS-22-07-R)*, ITESO, Tlaquepaque, Mexico, Nov. 2022.

[Loera-Díaz-23a] R. Loera-Díaz and J. E. Rayas-Sánchez, "Comparison of ADS circuital models for a microstrip low-pass filter," Internal Report *PhDEngScITESO-23-05-R (CAECAS-23-02-R)*, ITESO, Tlaquepaque, Mexico, Aug. 2023.

[Loera-Díaz-23b] R. Loera-Díaz and J. E. Rayas-Sánchez, "Parameter extraction graphical study using Kullback-Leibler formulations," Internal Report *PhDEngScITESO-23-13-R (CAECAS-23-04-R)*, ITESO, Tlaquepaque, Mexico, Dec. 2023.

[Loera-Díaz-24a] R. Loera-Díaz and J. E. Rayas-Sánchez, "Parameter extraction using l-norms and the Kullback-Leibler formulation in a validated EM model of a single-stub microstrip band-stop filter," Internal Report *PhDEngScITESO-24-12-R (CAECAS-24-04-R)*, ITESO, Tlaquepaque, Mexico, Jul. 2024.

[Loera-Díaz-24b] R. Loera-Díaz and J. E. Rayas-Sánchez, "A rigorous numerical comparison for parameter extraction using classical and Kullback-Leibler formulations for microstrip filters," Internal Report *PhDEngScITESO-24-17-R (CAECAS-24-06-R)*, ITESO, Tlaquepaque, Mexico, Nov. 2024.

[Loera-Díaz-25a] R. Loera-Díaz, J. E. Rayas-Sánchez, and Villa-Loustaunau, "A rigorous numerical comparison for parameter extraction using classical and Kullback-Leibler formulations illustrated with full-wave EM and equivalent circuit models for microstrip filters," in *IEEE MTT-S Latin America Microwave Conf. (LAMC-2025)*, San Juan, Puerto Rico, Jan. 2025, pp. 93-96.

[Loera-Díaz-25b] R. Loera-Díaz and J. E. Rayas-Sánchez, "Aggressive space mapping with parameter extraction based on the Kullback-Leibler distance applied to a synthetic example and some validated EM models of microstrip filters," Internal Report *PhDEngScITESO-25-04-R (CAECAS-25-01-R)*, ITESO, Tlaquepaque, Mexico, Apr. 2025.

[Loera-Díaz-25c] R. Loera-Díaz and J. E. Rayas-Sánchez, "Space mapping with parameter extraction based on the Kullback–Leibler distance illustrated with full-wave EM and equivalent circuit models for microstrip filters," *IEEE Transactions on Microwave Theory and Techniques*, early access version, 2025.

[Maas-14] S. A. Maas, *Practical Microwave Circuits*. Norwood, MA: Artech House, 2014.

[Matsuoka-91] K. Matsuoka and J. Yi, "Backpropagation based on the logarithmic error function and elimination of local minima," *1991 IEEE International Joint Conference on Neural Networks*, Singapore, 1991, pp. 1117-1122 vol.2.

[McEliece-01] R. J. McEliece, *The Theory of Information and Coding*. New York, NY: Cambridge Univ. Press, 2001.

[Mirotznik-97] M. S. Mirotznik and D. Prather, "How to choose EM software," *IEEE Spectrum*, vol. 34, pp. 53-58, 1997.

[Nafornita-12] C. Nafornita, Y. Berthoumieu, I. Nafornita, and A Isar, "Kullback-Leibler distance between complex generalized Gaussian distributions," in *2012 Proc. 20th European Signal Processing Conf. (EUSIPCO)*, Bucharest, Romania, Oct. 2012, pp. 1850-1854.

[Nelder-65] J. A. Nelder and R. Mead, "A simplex method for function minimization," *The Computer J.*, vol. 7, no. 4, pp. 308-313, Jan. 1965.

[Pozar-98] D. M. Pozar, *Microwave Engineering*. Amherst, MA: Wiley, 1998.

[Rautio-03] "Planar electromagnetic analysis," *IEEE Microwave Magazine*, vol. 4, no. 1, pp. 35-41, March 2003.

[Ravindran-06] A. Ravindran, K. M. Ragsdell, and G. V. Reklaitis, *Engineering Optimization: Methods and Applications.* Hoboken, NJ: Wiley, 2006.

[Rayas-Sánchez-01] J. E. Rayas-Sánchez, *Neural Space Mapping Methods for Modeling and Design of Microwave Circuits*, Ph.D. Thesis, Dept. of Electrical and Comp. Eng., McMaster University, Hamilton, Canada, 2001.

[Rayas-Sánchez-09] J. E. Rayas-Sánchez and J. A. Jasso-Urzúa, "EM-based optimization of a single layer SIW with microstrip transitions using linear output space mapping," *IEEE MTT-S Int. Microwave Symp. Dig.*, Boston, MA, Jun. 2009, pp. 525-528.

[Rayas-Sánchez-12a] J. E. Rayas-Sánchez, J. C. Cervantes-González, C. A. López, Z. Brito-Brito, and J. Aguilera-Torrenta, "Developing coarse and fine EM COMSOL models of a microstrip low-pass filter for space mapping optimization," Internal Report *CAECAS-12-19-R*, ITESO, Tlaquepaque, Mexico, Sep. 2012.

[Rayas-Sánchez-12b] J. E. Rayas-Sánchez and Z. Brito-Brito, "Broyden-based input space mapping optimization of a microstrip low-pass filter implemented in COMSOL," Internal Report *CAECAS-12-21-R*, ITESO, Tlaquepaque, Mexico, Oct. 2012.

[Rayas-Sánchez-16] J. E. Rayas-Sánchez, "Power in simplicity with ASM: tracing the aggressive space mapping algorithm over two decades of development and engineering applications," *IEEE Microwave Magazine*, vol. 17, no. 4, pp. 64-76, Apr. 2016.

[Rayas-Sánchez-20] J. E. Rayas-Sánchez, "An updated configuration to drive Keysight ADS from Matlab," Internal Report *CAECAS-20-05-R*, ITESO, Tlaquepaque, Mexico, Jul. 2020.

[Rayas-Sánchez-21a] J. E. Rayas-Sánchez, S. Koziel, and J. W. Bandler, "Advanced RF and microwave design optimization: a journey and a vision of future trends," *IEEE J. of Microwaves*, vol. 1, no. 1, pp. 481-493, Jan. 2021.

[Rayas-Sánchez-21b] J. E. Rayas-Sánchez, "Configuring Keysight Momentum for reliable full-wave EM simulation of microstrip lines," Internal Report *CAECAS-21-04-R*, ITESO, Tlaquepaque, Mexico, Jul. 2021.

[Rayas-Sánchez-25a] J. E. Rayas-Sánchez, Q. J. Zhang, J. W. Rautio, N. K. Nikolova, V. E. Boria, Q. S. Cheng, M. Yu, and W. J. R. Hoefer, "Microwave modeling and design optimization: The legacy of John Bandler," *IEEE Trans. Microwave Theory Techn.*, vol. 73, no. 01, pp. 87-101, Jan. 2025.

[Rayas-Sánchez-25b] J. E. Rayas-Sánchez, "Cognitive parameter extraction for space mapping design optimization," in *IEEE MTT-S Latin America Microwave Conf. (LAMC-2025)*, San Juan, Puerto Rico, Jan. 2025, pp. 9-12.

[Rayas-Sánchez-25c] J. E. Rayas-Sánchez, "Cognitive Broyden-based input space mapping for design optimization," *IEEE Microwave Wireless Tech. Lett.*, vol. 35, no. 6, pp. 760-763, Jun. 2025.

[Sheen-90] D. M. Sheen, S. M. Ali, M. D. Abouzahara, and J. A. Kong, "Application of the three-dimensional finite-difference time-domain method to the analysis of planar microstrip circuits," *IEEE Trans. Microwave Theory Tech.*, vol. 38, pp. 849-857, July 1990.

[Swanson-91] D. G. Swanson, "Simulating EM fields," *IEEE Spectrum*, vol. 28, pp. 34-37, 1991.

[Swanson-03] D. G. Swanson and W. J. R. Hoefer, *Microwave Circuit Modeling Using Electromagnetic Field Simulation*. Norwood, MA: Artech House, 2003.

[Søndergaard-03] J. Søndergaard, *Optimization using Surrogate Models by the Space Mapping Technique*, Ph.D. Thesis, Dept. of Informatics and Mathematical Modeling, Technical University of Denmark, Lyngby, Denmark, 2003.

[Veldhuis-03] R. Veldhuis and E. Klabbers, "On the computation of the Kullback-Leibler measure for spectral distances," *IEEE Transactions on Speech and Audio Processing*, vol. 11, no. 1, pp. 100-103, Jan. 2003.

[Vergara-09] A. Vergara, M. Muezzinoglu, N. Rulkov, and E. Huerta, "Kullback-Leibler distance optimization for artificial chemo-sensors," *IEEE Sensors Conference*, La Jolla, CA, Nov. 2009, pp. 1146-1150.

[Villa-Loustaunau-23] E. R. Villa-Loustaunau and J. E. Rayas-Sánchez, "Minimizing differential to common mode conversion caused by a right-angle behind in a differential microstrip interconnect by using a length match bump," Internal Report *PhDEngScITESO-23-01-R (CAECAS-23-01-R)*, ITESO, Tlaquepaque, México, Feb. 2023.

[Villa-Loustaunau-25] E. R. Villa-Loustaunau, J. E. Rayas-Sánchez, R. Loera-Díaz, and F. Rangel-Patiño, "Optimizing the full mixed-mode performance of a differential microstrip interconnect with a right-angle bend by using two symmetrical bumps," in *IEEE MTT-S Latin America Microwave Conf. (LAMC-2025)*, San Juan, Puerto Rico, Jan. 2025, pp. 97-100.

[Zhao-05] Y. Zhao, G. Xi, and J. Yi, "BP algorithm based on cross entropy function criterion," *Jisuanji Gongcheng/Computer Engineering*, vol. 31, no. 19, pp. 12-14, Oct. 2005.

[Zhou-20] X. Zhou, Z. Zhang, Q. Chen, and X. Liu, "A practical plateau lake extraction algorithm combining novel statistical features and Kullback–Leibler distance using synthetic aperture radar imagery," *IEEE J. Selected Topics in Applied Earth Observations and Remote Sensing*, vol. 13, pp. 4702-4713, 2020.

[Zhu -02] X. Zhu, *Fundamentals of Applied Information Theory*. Beijing: Tsinghua University Press, 2002.

Author Index

Subject Index

L

M

N

O

P

R

S

T

V

W

Y